1-1-2022

Biopolymer Unfolding as a Process of Biased Activated Barrier Crossing

Sudeep Adhikari

BIOPOLYMER UNFOLDING AS A PROCESS OF BIASED ACTIVATED BARRIER CROSSING

A Dissertation
presented in partial fulfillment of requirements
for the degree of Doctor of Philosophy
in the Department of Physics and Astronomy,
The University of Mississippi

by

SUDEEP ADHIKARI

MAY 2022

ABSTRACT

The biopolymer unfolding process can be conceptualized as the thermally activated crossing of a barrier in some energy landscape; the real-world unfolding dynamics are in correspondence with the rate of transit over the barrier. In this dissertation, we report on four projects that exploit this analogy to advance our understanding of so-called pulling experiments, in which a biopolymer chain is encouraged to unfold by direct application of forces to its two ends. Regardless of the specific experimental realization, standard pulling techniques give rise to a *biased* barrier crossing problem. The applied force has the effect of tilting the energy landscape. The height and shape of the barrier are altered by the tilt, and the rate of transit over the barrier is highly sensitive to such changes.

In the first project, we improve on existing analyses that treat the problem of barrier crossing in one dimension (1D). In the context of pulling experiments, biopolymers are often characterized by an effective 1D energy profile that depends on a single reaction coordinate, the extension or end-to-end distance. Features of this profile can be extracted from the probability distribution of the critical applied force at which the polymer unfolds. This analysis is typically based on the historical rate equations due to Bell and Evans or on the improved rate equations proposed by Dudko *et al*. We argue, however, that the former is inadequate, leading to unreliable landscape parameters in many common situations, and that the latter, while providing a better model at low pulling forces, displays unphysical behavior at high pulling and is afflicted with a point of mathematical breakdown. We propose a new form of the rate equation, one that is well-behaved everywhere (no pathologies or unphysical regimes), that produces a closed-form expression for the critical force distribution (which Dudko's form lacks), that leads to more reliable and faithful parameter extraction, and that is valid even up to fast pulling rates, as revealed by our numerical simulations.

In the second project, we argue that biased barrier crossing is governed by three intrinsic force scales, corresponding to the barrier-vaulting thermal kick that the bath provides, the applied pulling force required to fully deplete the barrier, and the instantaneous applied force. We further suggest that two independent ratios of these forces constitute arguments to an underlying scaling function. We identify universal behavior and demonstrate that data collapse onto a universal curve can be achieved for simulated data over a wide variety of energy landscapes having barriers of different height and shape and for loading rates spanning many orders of magnitude.

In the third project, we address some of the limitations of tracking only one reaction coordinate. For instance, a 1D analysis is insensitive to configurations that are degenerate in the end-to-end length; nor can it distinguish rate contributions from multiple transition pathways. As a first step, we extend our rate modeling to account for energy landscapes in two dimensions (2D). We derive a 2D form of our rate equation and numerically test its reliability with regard to prediction and landscape parameter extraction. We also test the degree of consistency between the 1D and 2D approaches.

In the fourth project, we simulate a semi-realistic toy model of a biopolymer using Monte Carlo sampling and parallel tempering with the goal of exploring how to choose a secondary reaction coordinate, complementary to the primary end-to-end extension. We assume that monomers in the chain backbone move in the continuum with a constraint of fixed neighbor distance (chemical bond length), subject to the energetic costs of bond-bending and of long-range interactions that account for excluded volume effects, hydrophobic attraction, and electrostatics. We implement local and global updates that produce an ergodic and efficient exploration of the conformational phase space. These computational tools are put to work on real protein sequences in order to highlight the limitations of the conventional analysis of pulling experiments that assumes projection onto a single reaction coordinate.

DEDICATION

To my parents

Mr. Raghu Nath Adhikari

Ms. Durga Devi Adhikari

&

my wife

Swapnil Pokhrel

LIST OF ABBREVIATIONS AND SYMBOLS

TS	Transition State
1D	One dimensional
2D	Two dimensional
MC	Monte Carlo
MD	Molecular Dynamics
SAW	Self Avoiding Walk

ACKNOWLEDGEMENTS

The accomplishments of graduate school set the stage for a future career. But a young student, eager to achieve something, quickly realizes how much he needs to learn, how limited his own knowledge is, and how much his success depends on the collective efforts of everyone around him. With that in mind, I would like to thank all of those who played a part in whatever I achieved as a grad student.

First and foremost, I would like to thank my Ph.D. supervisor, Kevin Beach, who is one of the nicest human beings I have ever met and who almost always had an answer to any question I had. The way he helped me navigate through these research projects and various frustrating dead ends was admirable. I would always return from a visit to his office with happiness, confidence, and with a sense of satisfaction, as it would solve a week's worth of confusion and indecision. Constantly pushing myself to independently learn new techniques demanded by the research projects we worked on has made me confident that I can learn whatever will be required of me in the future.

I would like to express my appreciation to my thesis committee members Luca Bombelli, Joel Mobley, and Sasan Nouranian, who have been so supportive throughout. It was pleasure to have them onboard, and I am grateful to them for reading through my whole dissertation and providing feedback to improve it. Apart from being a member of my committee, the constant help and support I got from Luca Bombelli will always hold a special place in my heart. I would also like to mention Alakabha Datta, who was ever present for help and support whenever I needed. My sincere gratitude goes to Ana Pavel, who provided me a chance to get involved in a collaborative project and help me add a new dimension to my research profile.

I would like to thank my peers and the staff in the physics department for playing their part in this journey and for being like a family to me. My group members, especially Khagendra

Adhikari, deserve an honorable mention for their constant help and support.

Most important, I would like to thank my parents for paving the way for my higher education and always encouraging me. My sibling Suyog, brother Sudeep, and sisters Reema & Minu deserve a mention for their constant encouragement. Finally, above all, I would like to thank my wife, Swapnil Pokhrel, my friend, my happiness, and love, for providing unconditional support and being with me joyfully through almost the entire journey.

TABLE OF CONTENTS

LIST OF FIGURES

CHAPTER 1

BACKGROUND MATERIAL

1.1 Introduction

A biopolymer consists of repeating units, or monomers, that are strung together to produce a long, flexible chain. In the case of a protein (a many-unit polypeptide chain), the monomers are amino acids; the repeating path of N–C–C–O atoms can be seen as the chain backbone, supporting the various residues. The chain's flexibility, along with the existence of monomer-monomer interactions of varying strength, character, and range, allows for the emergence of compact, folded configurations that are thermodynamically stable or at least long-lived. Biopolymers are typically described in terms of conformational energy landscapes [1–3]. Their folding, unfolding, and fluctuation processes can be represented by diffusive motion through these landscapes [4], which are complex, multidimensional hypersurfaces in the atomic or monomer coordinates.

The contribution of explicitly quantum processes notwithstanding [5], classical energy landscape theory [6–8] provides a useful framework for describing the evolution of biopolymers. Through this lens, structural transformation is viewed as a thermally driven escape from a local confining potential [9]. That is to say, the transition between a folded and an unfolded conformation—or between two differently folded ones—corresponds to a (stochastic) trajectory through the landscape, passing out of one well, over a barrier, and into another well.

Developing tools of analysis within this framework has become ever more pressing, given the profound developments in single-molecule biophysics [10–23]. One of the key practical problems is how to infer the energy landscape, or at least a projection of it onto an appropriate reaction coordinate, from experimentally measured quantities [24–33]. As is typical of inverse problems, recovery of the landscape from measured data is ill-conditioned: it is highly sensitive to

experimental uncertainties and to any assumptions that go into the forward model.

Thermally activated barrier crossing [34–37] is a ubiquitous and highly consequential process in physics, chemistry, and biology. An understanding of the factors that influence the rate of barrier crossing [38–41] is necessary for the interpretation of experiments that attempt to infer barrier height and shape from measurements of the escape rate. An important specialization—falling under the rubric of *pulling experiments*—is the case in which the barrier is diminished by an applied force, with the escape rate enhanced accordingly.

Experimental access to escape rate information in biochemistry has been revolutionized by the development of single-molecule force spectroscopy [42–46], in which a mechanical load is applied across a single molecule using an atomic force microscope or optical tweezers. The landscapes for biologically relevant sequences contain distinct, barrier-separated wells corresponding to various folded and unfolded conformations. (It is postulated that evolution has produced highly structured energy landscapes, rather than randomly corrugated ones, that typically possess a guiding funnel toward each biological useful conformation.) The rate of transition [47–49] from one well to another depends primarily on the height of the intervening barrier but also on its shape.

To simplify the task of analysis, landscapes are often converted into lower-dimensional manifolds [50–55] via projection or other dimensional reduction techniques. The most extreme example is the projection of the landscape onto an effective 1D free energy profile that has as its single functional argument the polymer chain's end-to-end distance. Despite the huge loss of information, this is still meaningful in the context of pulling experiments, because the molecular extension serves as a natural reaction coordinate, and the 1D energy profile often correctly encodes the folding dynamics. Numerous studies have been carried out to explore the unfolding process under the application of constant and time-varying pulling forces [56–62]. A key experimental goal is to be able to reliably reconstruct the 1D energy profile from measurements of an ensemble of escape events [63–66].

The motion of biopolymers can be simulated in real time using heat-bath-coupled Langevin dynamics, an approach that is well-justified within thermodynamics and statistical mechanics. The

heat bath (or *thermal bath* or *thermal reservoir*) in thermodynamics refers to a large body held at a constant temperature with which the system of interest is in contact; the system and bath must be able to exchange heat so that the two can come into equilibrium. In this work, the system of interest is the biopolymer, and the aqueous solution in which it is immersed serves as the bath. The bath is assumed to possess a large enough heat capacity to be an essentially infinite source of thermal energy, so that it can exchange energy with the system (as a thermal source or as a heat sink) without altering its temperature. For a system that has reached equilibrium, we can also consider motion in fictitious Monte Carlo time, so long as the conformational update rules produce correctly weighted coverage of the phase space.

In this dissertation, we are primarily interested in the mechanical unfolding of biopolymers by application of a bias force. The simulations we perform, analyze, and discuss run the gamut from point-particle dynamics over a 1D barrier up to Monte Carlo treatment of semi-realistic, coarse-grained, bead-and-rod models that include explicit molecular interactions.

Non-spontaneous unfolding of a biopolymer chain can be induced by an external pulling force. Such work is crucial to understanding the mechanical properties of the biopolymer and the details of the underlying energy landscape. How a protein molecule responds to external stimulus, particularly its extension in response to pulling, can provide valuable insight into its mechanical stability. The mechanical pulling process can be viewed as an activated barrier crossing process with bias. To explain the rate of barrier crossing, much excellent work has been done [67, 68]. In this dissertation, we build on those foundational insights.

A protein can be mechanically unfolded using a number of experimental techniques [69], including optical tweezers [70–72], magnetic tweezers [73, 74], and atomic force microscopy (AFM) [75–78]. In each of these approaches, the protein chain is typically tethered at one end to a surface and another end is left free for applying mechanical force. In the case of optical tweezers, both ends may be free and attached to polystyrene beads, which are manipulated with the potential gradients created by focused lasers (as illustrated in Fig. 1.1). The force response of the protein is monitored, typically under conditions of a time-dependent force with a constant loading rate

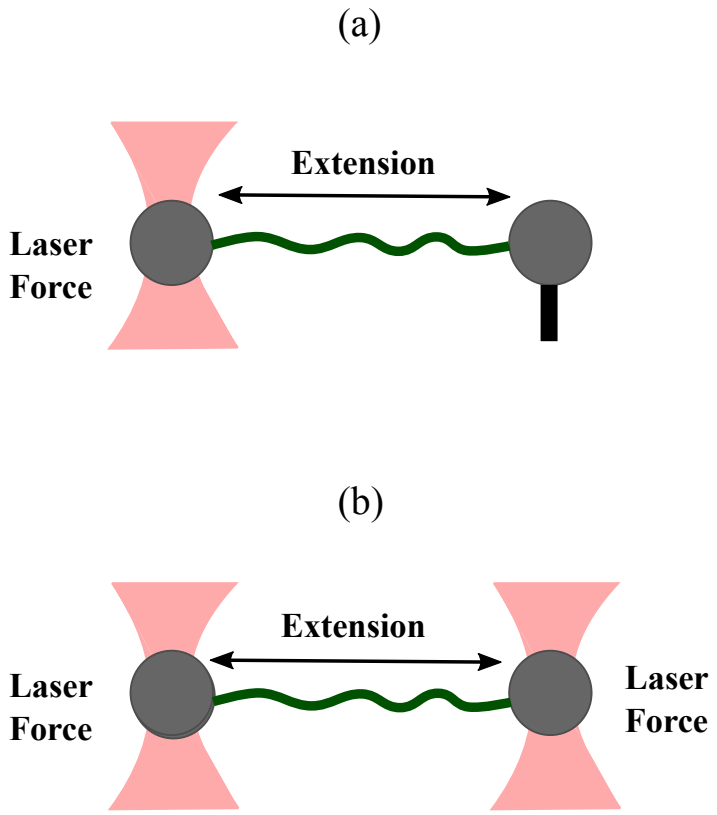

Figure 1.1. Schematic representation optical trap arrangement. (a) Single optical trap where the molecule is tethered at one end and pulled at the other end by using the laser potential (b) Double optical trap where the molecule is pulled on either end by using the laser potential

(force-extension mode) [79] or a constant force (force-clamp mode) [80]. In this dissertation, we try to simulate the mechanical pulling of protein chains with an eye to interpreting those numerical experiments in terms of a biased activated barrier crossing process [34–37]. We employ the kind of rate analysis commonly applied to chemical reactions.

1.2 Thermodynamic and kinetic stability of proteins

A protein chain is said to be in its native conformation when it has achieved the minimum value of its thermodynamic Gibbs free energy, G. For a system at constant temperature T and

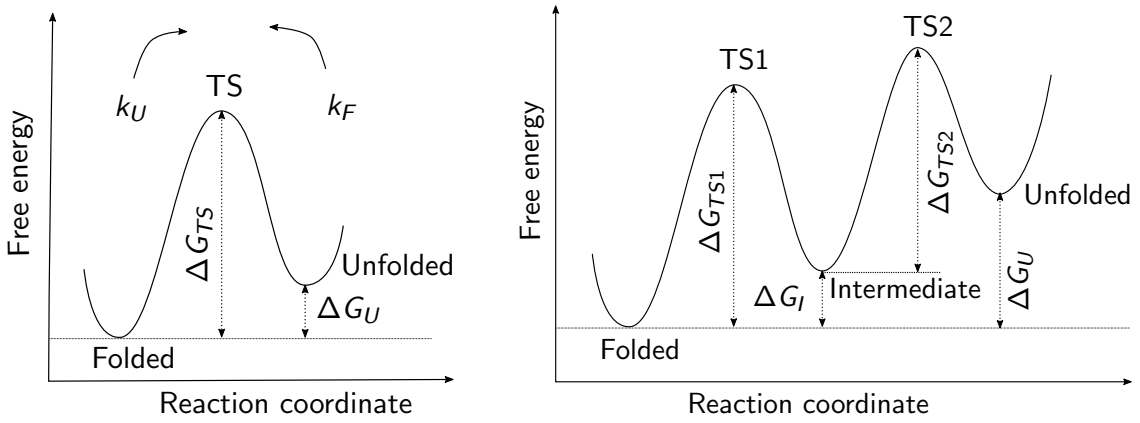

Figure 1.2. Left: schematic of two-state energy landscape of a protein, where the Folded state is separated by a single barrier TS. For an unfolding process, energy ΔG_{TS} is required to overcome the barrier. Right: a three-state energy landscape is shown containing a Folded, Intermediate, and Unfolded state. The unfolding process in this landscape is a two-step process. First, energy of ΔG_{TS1} is required to overcome the barrier at TS1 and then energy of ΔG_{TS2} is required to overcome the barrier at TS2. ΔG_{TS2} is the barrier height to unfolded state with respect to the intermediate state. Energies ΔG_I and ΔG_U are the energies of intermediate and unfolded state respectively with respect to the folded state.

pressure P, the change in the Gibbs free energy, ΔG, is used to determine whether a reaction is favorable or unfavorable. In the context of protein unfolding, the difference in Gibbs energy between unfolded and folded conformations determines the protein's thermodynamic stability. The difference in Gibbs energy simply refers to the amount of work done to transfer a body from one state to another as the body exchanges heat with its environment. The mathematical expression for that difference is $\Delta G = \Delta H - T\Delta S$, where ΔH refers to the change in enthalpy and ΔS refers to the change in entropy. The left panel of Fig. 1.2 illustrates the simplest situation, which corresponds to two wells separated by a single barrier. Many proteins exhibit more complex landscapes, where they can fold or unfold via intermediate states (see the right panel of Fig. 1.2).

Figure 1.3 shows a polypeptide chain moving down its folding funnel [3, 81]. If the energy landscape is rough, the chain passes through several short-lived, intermediate states before reaching the native state at the global minimum.

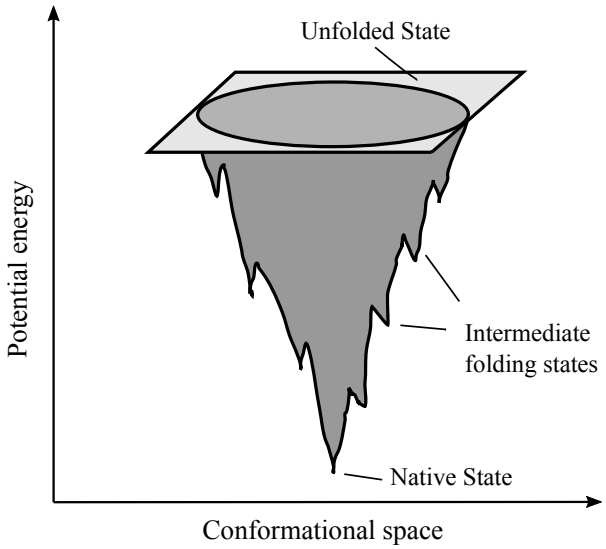

Figure 1.3. Folding funnel showing multiple folding intermediates before reaching a global minimum native state.

1.3 Relevant forces for proteins

The magnitude of the biologically relevant forces that affect proteins is crucial to the study of their mechanical properties. Proteins experience thermal agitation due to fluctuations consistent with the bath energy scale $k_BT = 4 \times 10^{-21}\,\mathrm{J} = 4.1\,\mathrm{pN\,nm}$ at room temperature. This roughly translates to 0.6 kcal/mol. The force magnitudes and associated length scales of various molecular processes are depicted in Fig. 1.4. As the chain is extended, the entropy tends to decrease (because of a reduction in the number of available microstates) and in the fully extended state the chain has only the unique straight-backbone configuration. As revealed by single molecular force spectroscopy, the typical length scale of interaction is on the order of nanometers, energies are on the order of k_BT, and entropic forces are on the order of piconewtons.

1.4 Reaction rate theory

The process of escape from a confining potential is understood from the theory of chemical reactions. Reaction rate theory is widely used, across areas such as chemical kinetics, diffusion in

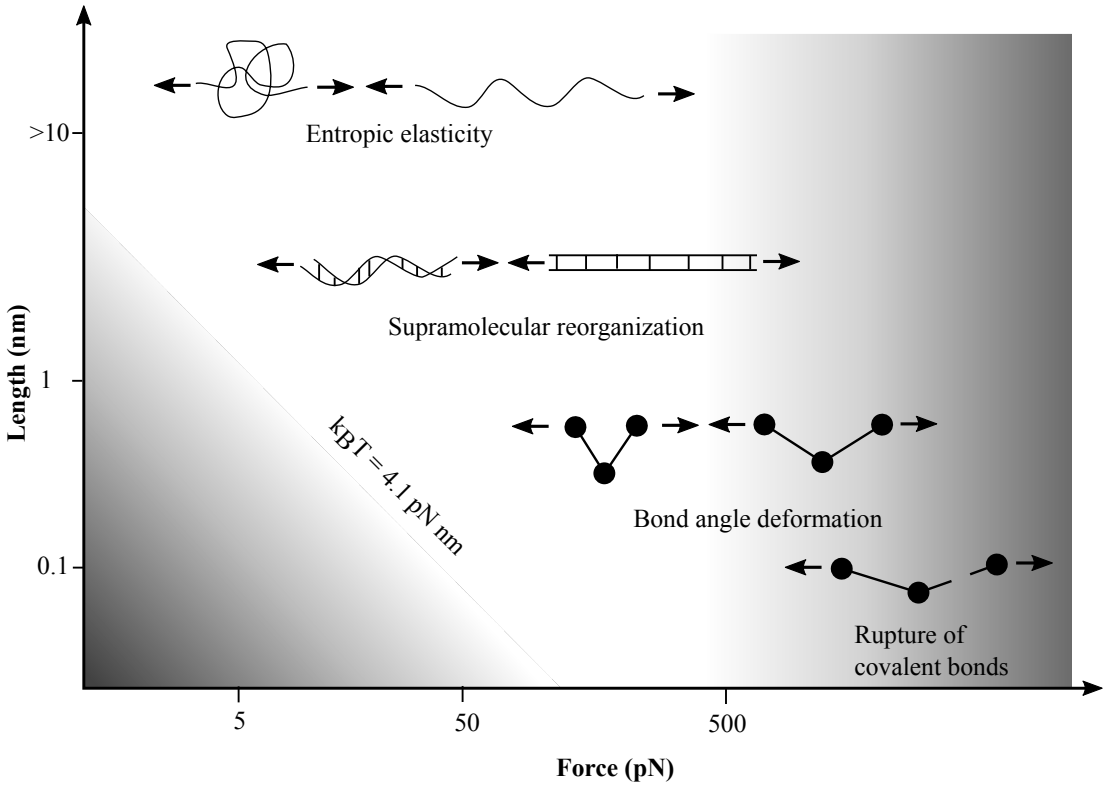

Figure 1.4. Figure illustrating the lengthscales and corresponding force scales associated with the bond breakage for different molecular interactions. The figure is a reworking of information from Ref. 77.

solids, homogenous nucleation, and electrical transfer theory. Chemists like to depict the progress of a chemical reaction as the motion along an effective one-dimensional coordinate, the so-called *reaction coordinate*, along which a free energy with a barrier is traced out. Fortunately, any activated barrier crossing problem can be treated with the same formalism. The concept of a rate theory was pioneered by Arrhenius. He was the first to explain the rate of chemical reaction as the product of a base rate and a suppression term that is exponentially sensitive to the ratio of the barrier height and temperature.

Variations of rate theory, such as transition state theory and Kramer's theory of diffusive barrier crossing [34], have been proposed. These theories are considered different from each other on the basis of assumptions they make about the motion leading to the transition and the definition of the transition state (TS). Here, TS refers to the surface that separates the reactant and the product state. In our work, the reactant state is considered to be the folded state and the product state to be the unfolded state. These states are separated by the free energy bottleneck. Rate theories are very important as they can be used to analyze, explain, and predict outcomes of the activated barrier crossing process.

1.4.1 Arrhenius law

The Arrhenius law states that the rate of chemical reaction k can be expressed in terms of two parameters, the activation free energy ΔG and a prefactor A:

$$k = Ae^{-\beta \Delta G}. \tag{1.1}$$

Here $\beta = 1/k_B T$, with k_B being Boltzmann's constant and T the temperature. Although the Arrhenius law was originally motivated by the rate of chemical reactions, the basic concept is applicable to almost any noise-activated barrier crossing mechanism. Generally, theories of chemical dynamics that invoke Eq. (1.1) in interpreting the experimental data view the transition as motion along a one dimensional reaction coordinate over a free energy barrier.

1.4.2 Transition state theory

The assumption in transition state theory is that a system moving toward its product state along the reaction coordinate is certain to achieve the product state once it crosses the TS. In other words, transition state theory views the orbit crossing TS as the "point of no return." It also contains a strong-coupling assumption, which presupposes thermal equilibrium throughout the entire system and neglects any effects due to a deviation from thermal equilibrium.

1.4.3 Kramer's theory

Kramer's theory connects more directly to the underlying Brownian motion. For a reaction coordinate x, this theory treats the dynamics along x as thermally randomized, damped motion in the presence of an effective potential $U(x)$. In this interpretation, the TS is no longer just the "point of no return" but instead is viewed as the point of "maximum indecision" at which the thermal fluctuations can take the system to either product or reactant state with equal probability.

The Langevin equation,

$$m\ddot{x} = m\dot{v} = -\frac{\partial U}{\partial x} - \gamma v + \xi(t), \tag{1.2}$$

is the basis of Kramers' theory. The noise $\xi(t)$ is only instantaneously correlated (no memory) and $\langle \xi(t)\xi(t') \rangle = 2k_B T\gamma\delta(t - t')$. Here, γ represents the damping parameter and is a uniform, temperature-independent, velocity relaxation rate. An overdamped limit with very high γ is sometimes assumed for the reaction dynamics in solution, and in this limit the left-hand-side of Eq. (1.2) is assumed to be negligible (since $|\gamma v| \gg m|\dot{v}|$). That is to say, the particle executes pure Brownian motion. For low γ, there will also be a significant inertial contribution.

1.5 Projection of biopolymer energy landscape onto lower dimension

Biopolymers such as DNA or proteins are ubiquitous in nature. There has lately been great interest in the study of these polymers, since they can be captured and manipulated individually. The other important aspect is that the behavior inside these polymers is best described using

statistical mechanics. The internal dynamics of these polymers are very complicated and expressed in terms of diffusion through a complicated multidimensional landscape. However, projecting this cumbersome multidimensional landscape onto a simpler, effective landscape in lower dimension simplifies the analysis.

1.5.1 One-dimensional analysis

It is common to suppose that the multidimensional hypersurface has been projected onto a lower-dimensional object. The projection can be effected using a straightforward mathematical trick: for a general reduction to dimension $d < 3N$, there is an effective energy potential $V_{\text{eff}}(q_1, q_2, \ldots, q_d)$ defined according to

$$\begin{aligned} P(q_1, q_2, \ldots, q_d) &= \frac{1}{Z} \int d\vec{r}_1 \cdots d\vec{r}_N \, d\vec{p}_1 \cdots d\vec{p}_N \, e^{-\beta H(\vec{r}_1,\ldots,\vec{r}_N,\vec{p}_1,\ldots,\vec{p}_N)} \\ &\qquad \times \mathcal{K}(q_1, q_2, \ldots, q_d; \vec{r}_1, \vec{r}_2, \ldots, \vec{r}_N) \\ &\equiv e^{-\beta V_{\text{eff}}(q_1, q_2, \ldots, q_d)}. \end{aligned} \tag{1.3}$$

Hence, for $d = 1$, with the end-to-end distance $q_1 = \ell$ selected via the choice of kernel, $\mathcal{K}(\ell; \vec{r}_1, \vec{r}_N) = \delta(\ell - |\vec{r}_N - \vec{r}_1|)$, we get

$$V_{\text{eff}}(\ell) = -\frac{1}{\beta} \ln \frac{1}{Z} \int d\vec{r}_1 \ldots d\vec{r}_N \, d\vec{p}_1 \ldots d\vec{p}_N \, e^{-\beta H(\vec{r}_1 \ldots \vec{r}_N, \vec{p}_1 \ldots \vec{p}_N)} \delta(\ell - |\vec{r}_N - \vec{r}_1|). \tag{1.4}$$

In most applications, we assume this landscape to be a double-well potential separated by a barrier, where one well represents the folded state and the other represents the unfolded state. The experimental art of pulling using an applied force is mimicked by tilting the landscape. As a matter of pulling protocol, the bias force can be either constant or variously time dependent.

Landscape parameters

There are several parameters that are useful in characterizing the features of an energy landscape. In the 1D picture (see Fig. 1.5), the most useful are the following:

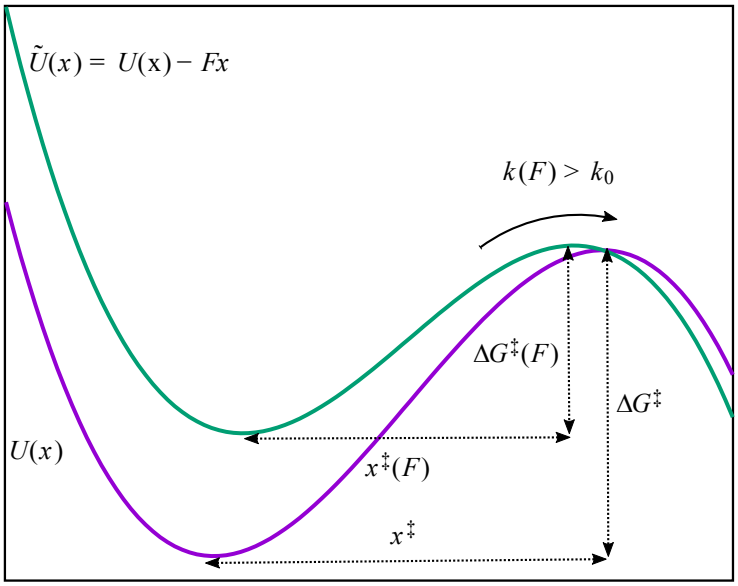

Figure 1.5. An unbiased double-well potential (solid purple line) and its biased counterpart (solid green line) are held up to comparison. In the unbiased potential, a particle escaping (left to right) from the well must traverse a barrier of height of $\Delta G^{\ddagger} = U(x_b) - U(x_l)$, over a distance $x^{\ddagger} = x_b - x_l$, where x_l and x_b are the positions of the left well and barrier. With application of an assistive pulling force ($F > 0$), the potential tilts to favor the destination well to the right of the barrier. The pulling force causes the well positions to shift; the barrier height and barrier distance decrease.

- intrinsic rate (k_0) : rate of transition from unfolded to folded state in the unbiased situation (i.e, the untilted landscape)
- barrier distance ($x^\ddagger$) : distance between the barrier and the minima of the folded well;
- barrier Height ($\Delta G^\ddagger$) : height of the barrier as viewed from the folded (originating) well;
- effective curvature ($\kappa^\ddagger$) : an inverse of the sum of the inverses (in the spirit of the reduced mass of the two-body central force problem),

$$\frac{1}{\kappa^\ddagger} = \frac{1}{U_0''(x_l)} - \frac{1}{U_0''(x_b)} = \frac{1}{\kappa_l} + \frac{1}{\kappa_b}, \tag{1.5}$$

  where κ_l and κ_b are the curvatures of folded well and barrier, respectively;
- shape parameter (ν): characterizes the shape of the barrier and is defined as $\nu = 2\Delta G^\ddagger/\kappa^\ddagger x^{\ddagger 2}$.

Escape rate modeling

To address the response of proteins to a mechanical pulling force, and the attendant changes in the corresponding landscape (see Fig. 1.6), several rate models have been developed. These predict the unfolding rate in the presence of bias with respect to the rate established in the unbiased case.

Bell-Evans or Bell-Evans-Richie model—this model explains protein unfolding via a two-state process by an energy barrier between folded and unfolded states. The energy barrier is defined by a single reaction coordinate, typically the end-to-end length. In pulling experiments using optical tweezers [82], the determination of landscape features has historically been carried out using this phenomenological theory [58–60, 67, 83], which predicts a rate

$$k_{\mathrm{BE}}(F) = k_0 e^{\beta F x^\ddagger}. \tag{1.6}$$

Here, $\beta^{-1} = k_B T$ is the thermal energy scale set by the aqueous environment; $x^\ddagger$ is the minimum-to-barrier distance of the effective 1D potential $U(x)$, a continuous (but not necessarily smooth)

function of the end-to-end extension. The model is expected to valid in the limit of weak applied force or extremely low pulling rate and very high barrier.

Dudko-Hummer-Szabo Model—Dudko and coworkers have tried to make the analysis more rigorous [68]. They calculated $k(F)$ and the corresponding probability density of the rupture force $p(F_c)$ within the framework of Kramer's theory for two specific free energy surfaces—the cusp surface and the linear cubic surface—and showed that these two examples can be subsumed into a single result [appearing as Eq. (3) in Ref. 68],

$$k_{\mathrm{D}}(F) = k_0\left(1 - \frac{\nu F x^{\ddagger}}{\Delta G^{\ddagger}}\right)^{1/\nu - 1} e^{\beta \Delta G^{\ddagger}\left[1 - (1 - \nu F x^{\ddagger}/\Delta G^{\ddagger})^{1/\nu}\right]}, \tag{1.7}$$

with interpolation provided by a shape parameter ν. This encompasses the Bell-Evans result, since $k_{\mathrm{D}}(F) \to k_{\mathrm{BE}}(F)$ as $\nu \to 1$. It is clear, however, that for all $\nu \neq 1$ Eq. (1.7) has a dangerous point of nonanalyticity. The vanishing of the rate $k_{\mathrm{D}}(F) \to 0$ as $F \to \Delta G^{\ddagger}/x^{\ddagger}\nu$ (for shape parameters in the range $0 < \nu < 1$) is manifestly unphysical; hence the Dudko expression is only appropriate for the pulling regime in which $F \ll \Delta G^{\ddagger}/x^{\ddagger}\nu$. In fact, the region of validity is more constrained still, since we should further require that the escape rate grow with pulling force. As it turns out, the function $k_{\mathrm{D}}(F)$ is monotonically increasing only for

$$F < \frac{\Delta G^{\ddagger}}{x^{\ddagger}\nu}\left[1 - \left(\frac{1-\nu}{\beta \Delta G^{\ddagger}}\right)^{\nu}\right]. \tag{1.8}$$

We propose more robust analysis to address these limitations in Ch. 3.

1.5.2 Two-dimensional analysis

In 2D analysis, the multidimensional landscape is projected onto a two dimensional landscape given by Eq. (1.9) which comes from Eq. (1.3) with $d = 2$.

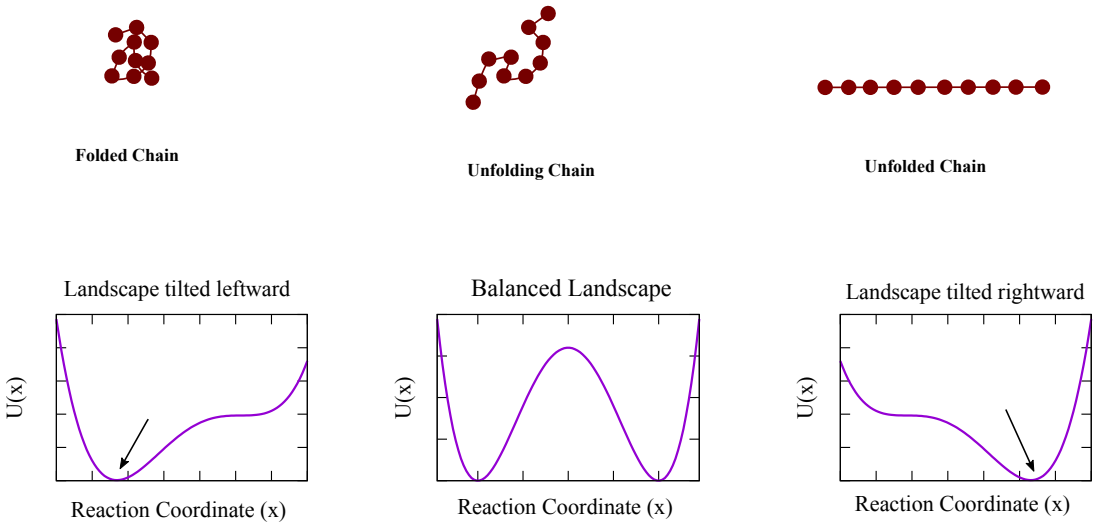

Figure 1.6. Top row: transformation from the folded (left) to unfolded (right) state proceeds by way of intermediate conformations that are positioned along the intervening energy barrier. Bottom row: in a balanced energy landscape, the chain in equilibrium will appear folded and unfolded with equal frequency, and the rate from left to right will match the rate from right to left; the application of a bias force tilts the landscape—favoring one state or another—and can eventually deplete barrier, so that the folded or unfolded state alone is stable.

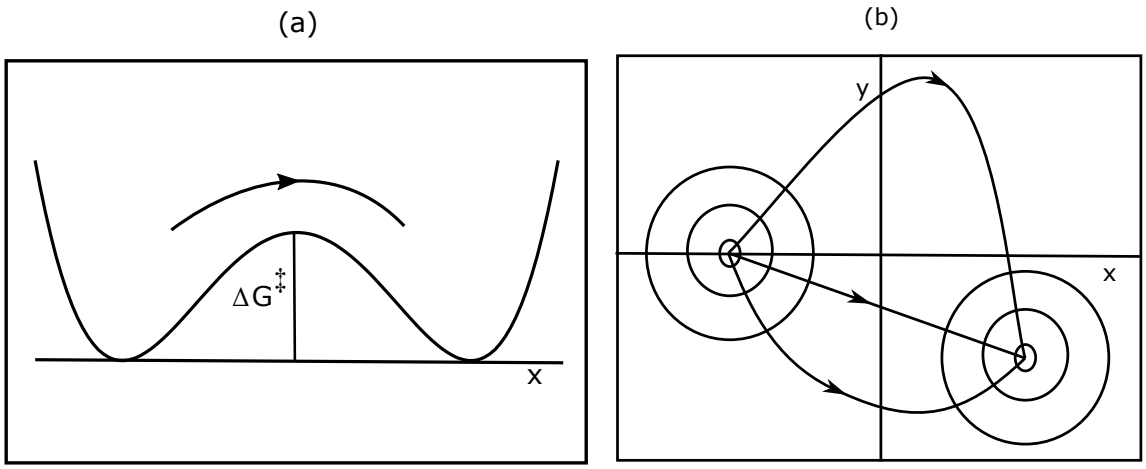

Figure 1.7. Figure to depict the transition paths from left well to right well: (a) One-dimensional landscape where there is only one possible path for the transition and (b) Two-dimensional landscape where there are multiple possible paths for the transition.

$$P(x,y) = \frac{1}{Z}\int d\vec{r}_1 ... d\vec{r}_N \, d\vec{p}_1 ... d\vec{p}_N \, e^{-\beta H(\vec{r}_1 ... \vec{r}_N, \vec{p}_1 ... \vec{p}_N)} \delta(x - |\vec{r}_N - \vec{r}_1|) \delta(y - R_g(c)) \\ \equiv e^{-\beta V_{\text{eff}}(x,y)}. \tag{1.9}$$

The projected 2D landscape consists of primary and secondary reaction coordinates end-to-end length l and cylindrical radius of gyration R_g respectively. The expression of R_g in our analysis is given by Eq. (1.14).

Motivation

The motivation behind 2D generalization was the inability of 1D model to recognize the protein chain with same end-to-end length but different conformational structure. In other words, in 1D model, the chain with same end-to-end length would have degenerate states as in Fig. 1.8 even if they have different folding conformations. This method works well in case of small proteins but it is suboptimal in case of protein with knots and multiple transition pathways of unfolding as shown in Fig. 1.7 (b). This sub-optimality in 1D model led to 2D generalization. To address this issue, we thought the most intuitive way would be to consider secondary reaction coordinate perpendicular

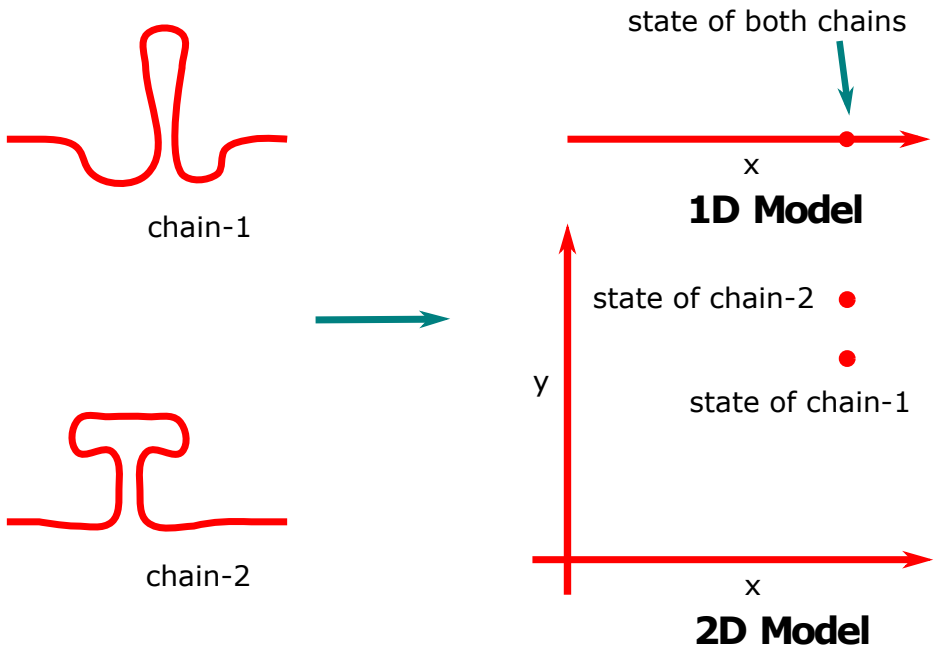

Figure 1.8. Chain configuration in one-dimensional analysis showing degenerate states for the chain with same end-to-end length (top right) and configuration states of biopolymer chain it two-dimensional analysis (bottom right). Two dimensional model lifted the degeneracy and 2D configuration can be projected into one dimensional configuration.

to primary reaction coordinate (as it lifts the degeneracy) and observe how analysis works. The analysis in fact worked so well and its robustness was validated by the numerical simulation in Ch. 5.

Landscape parameters

- intrinsic rate (k_0): rate of going from unfolded to folded state in unbiased situation;
- barrier distance ($r^{\ddagger}$): distance between the barrier and the minima of the folded well

$$\begin{aligned} x^{\ddagger} &= x_b - x_l \\ y^{\ddagger} &= y_b - y_l \\ r^{\ddagger} &= x^{\ddagger}\cos\theta + y^{\ddagger}\sin\theta; \end{aligned} \tag{1.10}$$

- barrier height ($\Delta G^{\ddagger}$): height of the barrier in relation to the folded well

$$\Delta G^{\ddagger} = U(x_b, y_b) - U(x_l, y_l); \tag{1.11}$$

- effective curvature ($\kappa^{\ddagger}$): see Sec. 5.2 for the full expression of $\kappa^{\ddagger}$.

1.6 Role of temperature in the mechanical properties of proteins

Mechanical flexibility is very important for the function of many proteins. How temperature affects in pulling experiments is very important to figure out. The study suggested that with increase in temperature, the unfolding force distributions narrowed and the value of minimum to barrier distance from folded well increased. This claim is corroborated by the results obtained from our simulation seen in table 1.1.

Table 1.1. Effect of temperature in critical force distribution. The value of k_BT is in pN nm and force is in pN. As the temperature of the simulation increases, the critical force distribution narrows down as seen in table below. The barrier height $\Delta G^{\ddagger}$of the potential considered here is 54 pN nm and the loading rate KV is 10^{-3} pN µs^{-1}.

k_BT	Critical force ($\overline{F}_C$)	Uncertainty in critical force (δF_C)
10.8	0.21	0.20
18.9	0.025	0.024
24.3	0.013	0.012
32.4	0.0072	0.0067

1.7 Semi-realistic modeling

1.7.1 Polymer chain architecture

A polymer molecule consists of similar repeating units called monomers. We considered a polymer chain with N monomers, each of which is separated by bonds of length b as shown in Fig. 1.9. The positions of the monomers are denoted by $\vec{r}_i$ ($i = 0, 1, 2, ..., N-1$). The two ends of the ith bond are at $\vec{r}_{i-1}$ and $\vec{r}_i$. In this case the end-to-end vectors between two bonds can be defined by

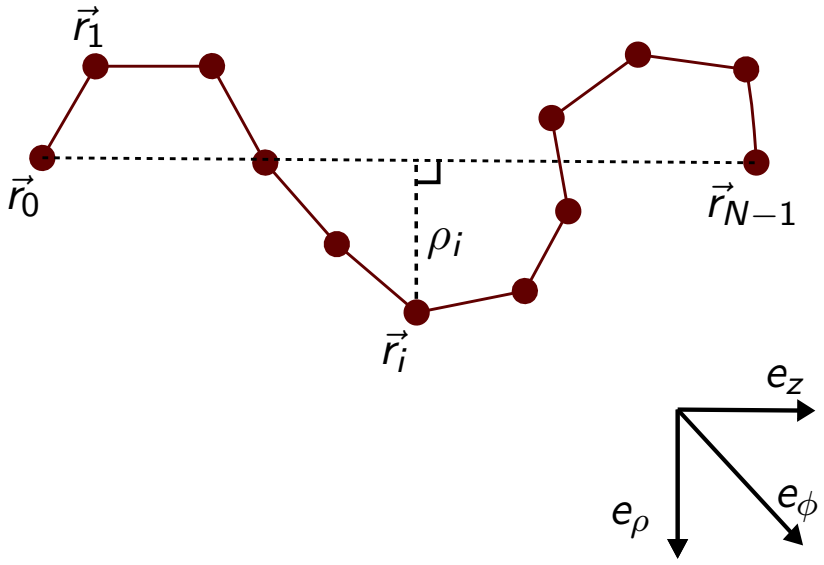

Figure 1.9. Polymer chain showing end-to-end vector $\vec{l} = \vec{r}_{N-1} - \vec{r}_0$ and and cylindrical radius of gyration $R_g = \sqrt{\langle \sum_{i=0}^{N-1} \rho_i^2 \rangle / N}$.

$$\vec{l} \equiv \vec{r}_{N-1} - \vec{r}_0. \tag{1.12}$$

The value of $\vec{l}$ differs from configuration to configuration. Although $\vec{l}$ represents only a portion of the conformational information, its average is always a good estimation of the chain's overall extent. The mean-square end-to-end distance of the chain is the thermally averaged value of $\vec{l} \cdot \vec{l}$:

$$\langle l^2 \rangle = \langle (\vec{r}_{N-1} - \vec{r}_0)^2 \rangle. \tag{1.13}$$

In some cases, the end-to-end distance is not sufficient to distinguish the various folded states. Hence, we have incorporated another quantity we call the cylindrical radius of gyration R_g with

$$R_g = \sqrt{\frac{\langle \sum_{i=0}^{N-1} \rho_i^2 \rangle}{N}}. \tag{1.14}$$

We can assume the whole chain to be contained in the cylinder of radius equal to the largest ρ_i and length l with its axis along end-to-end length vector as shown in Fig. 1.9.

1.7.2 Coarse-grained bead and rod model

The chain was assumed to be a combination of beads and rods. The beads represented monomers and the rods represented the covalent bond in between. Hydrophobic, charged and neutral monomers were taken into consideration and different update schemes like pivot rotation and site rotation were incorporated to map the chain onto the energy landscape with interaction potential:

$$V_{int} = J \sum_{i=1}^{N-2} \cos\theta_i + \sum_{i=0}^{N-3} \sum_{j=i+2}^{N-1} \left(V_{ij}^{EV} + V_{ij}^{H} + V_{ij}^{C} \right). \tag{1.15}$$

The first term in Eq. (1.15) represents the nearest neighbor bending cost summed over the whole chain. J is a constant representing the bending energy scale. The higher its value, the more difficult the chain is to bend (more rigid, less flexible). The θ_i values represent the bending angle between two adjacent bonds (the angle in the triangle formed by the three positions $\vec{r}_{i-1}$, $\vec{r}_i$, and $\vec{r}_{i+1}$) and it takes the values from 0 to 2π. At $\theta_i = 0$, the chain has fully extended configuration and this was assumed to be the initial state of our simulation.

Second term in Eq. (1.15) represents the pairwise long range interaction. Here, $V_{ij}^{EV} = V_0\Theta(a - r_{ij})$ represents excluded volume interaction term which prevents the overlapping of monomers. The value of V_0 is very high and almost tends to ∞. $\Theta(a - r_{ij})$ is a Heaviside step function which is equal to 1 for positive argument and zero for negative argument.

Similarly, $V_{ij}^{H} = f(A_i, A_j) \exp\left[(a - r_{ij})/b\right]$ represents the hydrophobic attraction term where $f(A_i, A_j)$ represents the strength of hydrophobic attraction between monomers A_i and A_j. These monomers basically try to shield them from water by coming closer to each other. The attraction is larger if both A_i and A_j are hydrophobic and smaller if one of them is neutral and other is hydrophobic. However, zero attraction is assumed if both of them are neutral. We will precisely talk about their magnitudes in numerical simulation.

Finally, $V_{ij}^{C} = g(A_i, A_j) \exp\left(-r_{ij}/\lambda\right) / \sqrt{b^2 + r_{ij}^2}$ represents the coulomb interaction term where $g(A_i, A_j)$ represents the strength of coulomb interaction. It is assumed to be positive if both A_i and A_j have like charges and assumed to be negative if they have unlike charges. The magnitudes

however are equal in both the cases. This term does not contribute if either or both the monomers in pair are neutral. The term λ represents the screening length.

1.8 Motivation

Mechanical unfolding of protein and its response to mechanical pulling force provides a valuable insight regarding the mechanical stability of protein. It would also help to provide the knowledge about the underlying protein landscape. Henceforth, we are really interested in simulating these experiments numerically and address the analytical limitations of these analyses. The limitations in preexisting rate equations defining rate of going from unfolded to folded state motivated us to come up more robust form of rate equation given by Eqs. (3.1) and (3.11). We believe, this piece of work in Ch. 3 improved 1D rate analysis in much better way. We continued this piece of work as we were motivated to get the global picture in 1D rate analysis and displayed the universality in 1D barrier escaping analysis via our work described in Ch. 4. Now, since we reinforced the 1D analysis as a whole, we thought it is better to address the limitation of 1D analysis and come up with some modifications to it. Since, the projection of multidimensional landscape to one dimension was not always optimal, especially for protein with larger sizes i.e, with knots and multiple unfolding pathways, we were motivated to propose a 2D model and generalize our 1D analysis in Ch. 3 to the work described in Ch. 5. The result we obtained were really encouraging and it further motivated us to explore the real physical form of the secondary reaction coordinate which motivated us to pursue different method of analysis using Monte Carlo simulation with efficient sampling techniques for semi-realistic polymer chains. This piece of work is described in Ch. 6. This is overall motivation behind pursuing the work explained in this dissertation.

1.9 Organization of dissertation

The dissertation will be organized in the following way. The relevant numerical methods used in this dissertation will be discussed in Ch. 2. In Ch. 3, the first project, biased activated barrier crossing in one dimension is discussed in detail. This piece of work has already been published

in Physical Review Research [84]. Second project depicting the universality in biased activated barrier crossing is described in Ch. 4. In Ch. 5, the sub optimality of one dimensional rate analysis is addressed by proposing a two dimensional analysis. This analysis works well in case of an abstract two dimensional landscape and we were even able to obtain a nice degree of convergence between one dimensional analysis and two dimensional analysis under suitable rescaling. In Ch. 6, we tried to reveal the limitation of single reaction coordinate picture using the Monte Carlo technique. This was our fourth project. Finally in Ch. 7, we summarize the whole dissertation work.

CHAPTER 2

METHODS

To accomplish this dissertation work, we have used three different methods. Heat bath coupled one-dimensional Langevin Dynamics, two-dimensional Langevin Dynamics with optimization and Monte Carlo technique with efficient sampling techniques such as parallel tempering and adaptive biasing force. We used 1D Langevin Dynamics for Chs. 3 and 4, 2D Langevin dynamics for Ch. 5 and Monte-Carlo technique for Ch. 6.

2.1 One-dimensional Langevin Dynamics

This particular work is one dimensional analysis of activated barrier crossing in relation to biopolymers like protein. For this work we assumed the protein chain to be in one dimensional conformational landscape with single reaction coordinate x. This reaction coordinate was made to execute the Langevin's dynamics according to 1D Langevin equation

$$m\ddot{x} = m\dot{v} = -\frac{\partial U}{\partial x} - \gamma v + \xi(t). \tag{2.1}$$

The process was implemented using a modern reformulation [85] of the Verlet algorithm [86]. The relevant experimental situation for this was a molecule of mass m executing stochastic motion in a biquadratic potential $U(x)$. The molecule was assumed to be pulled from two ends by a laser potential of force constant K and pulling velocity V; i.e, with an instantaneous force $F = KVt$ that increases linearly with time. The stochastic force $\xi(t)$ was drawn randomly from the Gaussian distribution of width $\sqrt{(2m\gamma k_B T \delta t)}$ with γ being the damping parameter. Low value of γ meant the inertial limit and high γ meant diffusion limit with the system executing Brownian motion.

The value of pulling force at which the molecule was fully extended was recorded. In the context of simulation, that's when the molecule either crossed the barrier or the barrier vanished. This value of force is known as the rupture or critical force. After getting the value of critical force for a protein molecule in a particular landscape, further analysis related to the probability and cumulative probability distribution was done to test the reliability of analytic expression of our rate equation in both prediction and parameter extraction. For prediction, the probability distribution and cumulative probability distribution of critical force were compared with the expressions obtained from Bell-Evans rate equation and our rate equation. For parameter extraction, bootstrapping technique was used. The simplified algorithm is written below.

2.1.1 Algorithm

Forward Problem - Prediction

1. Initialize the simulation in the left well, i.e, folded well.
2. Draw the starting velocity v_0 and position x_0 from distributions $e^{-\beta m v^2/2}$ and $e^{-\beta U(x)}\Theta(x_b - x)$, respectively, so that each simulation began fully thermalized.
3. Apply the biasing force F to the potential landscape and update the position and velocity of the particle using modified form [85] of Verlet algorithm [86].
4. Flag the value of the pulling force and time at which the particle convincingly crossed the barrier or barrier vanished.
5. Repeat steps 1 to 4 for 2500 times to get 2500 values of critical or rupture forces .

Inverse Problem - Landscape parameter extraction

1. Sort critical force distribution obtained from step 5 of forward problem
2. Bootstrap and generate multiple copies of the force distribution
3. Fit each of these copies of distribution using analytic expression of cumulative probability distribution and extract well parameters.

4. Compare these obtained parameters with actual values of well parameters to investigate the reliability of theoretical equations.

2.2 Two-dimensional Langevin Dynamics

For this particular work, 2D landscape with minima on either side of the saddle barrier was chosen to be the protein landscape. Unlike one dimensional analysis; we assumed the chain here to execute Langevin dynamics simultaneously in two mutually perpendicular directions though the motion along each reaction coordinate was assumed to be independent with each other.

$$m\ddot{\vec{q}} = m\dot{\vec{v}} = \frac{\partial U}{\partial \vec{q}} - \gamma\dot{\vec{q}} + \vec{\xi}(t). \tag{2.2}$$

Here, $\vec{q}$ is the generalized coordinate. Equation (2.2) can be broken into two independent equations as in Eq. (2.3) and can be used to address the motion of molecule along two independent directions x and y.

$$\begin{aligned} m_x\ddot{x} = m_x\dot{v}_x &= \frac{\partial U}{\partial x} - \gamma_x\dot{x} + \xi_x(t) \\ m_y\ddot{y} = m_y\dot{v}_y &= \frac{\partial U}{\partial y} - \gamma_y\dot{y} + \xi_y(t). \end{aligned} \tag{2.3}$$

The pulling force used here was similar to the one used in 1D analysis. However, the landscape potential in 2D analysis was rotated at discrete angles to explore the change in the impact of pulling force with respect to the pulling angle. The direction of pulling was always maintained along x-axis, primary reaction coordinate. Other similar analysis would be to apply the pulling force at an angle to x-axis until it becomes ineffectual. Theoretically it should happen when the pulling force is applied at right angle to x-axis or after the potential has been rotated by ninety degree still applying the force along the direction of unrotated x-axis.

The value of rupture force obtained from this analysis was recorded and the action was repeated numerous time to obtain the distribution of the rupture force. After this the 2D landscape

was projected to get the 1D landscape and simulation was carried out to see the degree of convergence between simulation in 2D landscape and reconstructed 1D landscape. On suitable scale of values of damping parameter 2D landscape simulation converged to the simulation in reconstructed 1D landscape. This process happened only till 2D landscape was rotated by reasonably small angle. At larger angle, these two simulations did not match. This is understandable as 1D projection won't account the rotation of 2D landscape and at some point it will be converted into single well instead of double well seemingly bi-quadratic potential. While executing 2D simulation gradient descent algorithm was used to flag the extrema in each step of the simulation. Also, we were not always able to reconstruct closed form expression of 1D landscape from 2D landscape and hence we used mathematical spline, an interpolation technique, to reconstruct the 1D landscape.

2.2.1 Transition analysis

Figuring out the transition state was one of the most challenging tasks we faced during two dimensional analysis. It was not that straightforward and obvious as one dimensional analysis. To resolve this issue we had to come up with some sort of mini-algorithm.

Consider a two dimensional potential well $U(x, y)$ separated by a saddle barrier with left / folded well at coordinate (x_l, y_l) and right / unfolded well at coordinate (x_r, y_r). If $\vec{r_l}$, $\vec{r_r}$ and $\vec{r_t}$ are the position vectors of bottom of the left well, bottom of the right well and the position of the particle at any instant of time t in simulation respectively, then

$$\begin{aligned} \vec{r_l} &= \langle x_l, y_l \rangle \\ \vec{r_r} &= \langle x_r, y_r \rangle \\ \vec{r_t} &= \langle x(t), y(t) \rangle \end{aligned} \tag{2.4}$$

Let

$$\begin{aligned} \vec{\Delta r_l} &= \vec{r_l} - \vec{r_t} \\ \vec{\Delta r_r} &= \vec{r_r} - \vec{r_t} \end{aligned} \tag{2.5}$$

If $\hat{g}$ is the unit gradient vector then,

$$\begin{aligned} \vec{\nabla}U &= \hat{i}\frac{\partial U}{\partial x} + \hat{j}\frac{\partial U}{\partial y} \\ |\vec{\nabla}U| &= \sqrt{\left(\frac{\partial U}{\partial x}\right)^2 + \left(\frac{\partial U}{\partial y}\right)^2} \\ \hat{g} &= -\frac{\vec{\nabla}U}{|\vec{\nabla}U|} \end{aligned} \tag{2.6}$$

At transition, $\hat{g} \cdot \Delta\vec{r}_l$ and $\hat{g} \cdot \Delta\vec{r}_r$ flip their sign, i.e, at transition $\hat{g} \cdot \Delta\vec{r}_l$ turns negative and $\hat{g} \cdot \Delta\vec{r}_r$ turns positive simultaneously.

2.2.2 Algorithm

Two dimensional Langevin dynamics

1. consider a two dimensional potential $U = U(x, y)$ with two wells separated by a saddle barrier.

2. Initialize the simulation in the bottom of left well, i.e, folded well.

3. Draw the stochastic forces on the molecule along x and y direction given by $\xi_x(t)$ and $\xi_y(t)$ respectively, randomly from the Gaussian Distribution of width $(2m_x\gamma_x k_B T\delta t)^{1/2}$ and $(2m_y\gamma_y k_B T\delta t)^{1/2}$ respectively with $k_B T = 4.1\,\mathrm{pN\cdot nm}$, $\gamma_x = 20\,\mu\mathrm{s}^{-1}$, $\gamma_y = 20\,\mu\mathrm{s}^{-1}$ and δt ranging from 10^{-1} µs to 10^{-5} µs from low to high pulling rates.

4. Apply the biasing force F to the potential landscape along the primary reaction coordinate and update the position and velocity of the particle using modified Verlet algorithm.

5. Flagged the value of the pulling force and time at which the particle convincingly crossed the barrier or barrier vanished that is when $\hat{g} \cdot \Delta\vec{r}_l$ and $\hat{g} \cdot \Delta\vec{r}_r$ flip their sign.

6. Repeat steps 1 to 5 for 2500 times.

7. Repeat steps 1 to 6 for different discrete angles of rotation of the potential landscapes.

Projection of 2D landscape to 1D landscape and spline interpolation

1. Obtained discrete values of 1D potential corresponding to our 2D potential using mathematical technique as seen in Eq. (5.14).

2. Used cubic spline technique of interpolation to obtain smooth form of 1D potential corresponding to 2D potential used.

3. Repeated 1D analysis for this reconstructed 1D landscape.

4. Cumulative probability distribution of the rupture force corresponding to 1D and 2D landscapes were compared to see the degree of convergence.

2.3 Monte Carlo

In this work, we allowed the protein chain with N monomers A_i ($i = 0, 1, \ldots, N-1$) of diameter a separated by bond length b, explore the energy space given by the energy hamiltonian (Eq. (1.15)) with given interation potential using various methods of updates. Two different update methods, pivot rotation and site rotation, were used. The move was accepted if either $dE < 0$ or ratio of probabilities of two successive states, $\exp(-\Delta E/k_B T)$ was greater than a small randomly generated number from uniform distribution between 0 and 1. Metropolis Monte Carlo method [87] was used for this. To make sure simulation did not get stuck in local minima, efficient sampling techniques like parallel tempering [88] or adaptive biasing force were used.

2.3.1 Pivot rotation

A random site was chosen and the portion of chain after that site was allowed to rotate freely about that site given by following rotation transformation.

1. Choose random site $j = 1, \ldots, N-2$ to be the origin for the rotation i.e, exclude the end sites.

2. Identify $j+1, j+2, \ldots N-1$ as a rigid body to rotate, origin at $\vec{r}_j$.

   Update rule:

Choose $\phi \in (0, 2\pi)$, $\theta \in (-\pi, \pi)$ and update $\vec{r}_{j+1}, \vec{r}_{j+2}, \ldots \vec{r}_{N-1}$ to $\vec{r'}_{j+1}, \vec{r'}_{j+2}, \ldots \vec{r'}_{N-1}$ respectively given by the update relation:

$$\begin{aligned} \vec{r}_{j+1} \rightarrow \vec{r'}_{j+1} &= R_{\theta,\phi}(\vec{r}_{j+1} - \vec{r}_j) + \vec{r}_j \\ \vec{r}_{N-1} \rightarrow \vec{r'}_{N-1} &= R_{\theta,\phi}(\vec{r}_{N-1} - \vec{r}_j) + \vec{r}_j \end{aligned} \tag{2.7}$$

3. Check if $|\vec{r'}_{n+1} - \vec{r'}_n| \equiv a$, within uncertainty 10^{-12}.

4. After pivot rotation, the components of a vector change to,

$$\begin{aligned} r_x &\rightarrow r'_x = r_x \cos\theta - r_y \sin\theta \\ r_y &\rightarrow r'_y = \cos\phi(r_x \sin\theta + r_y \cos\theta) - r_z \sin\phi \\ r_z &\rightarrow r'_z = \sin\phi(r_x \sin\theta + r_y \cos\theta) + r_z \cos\phi \end{aligned} \tag{2.8}$$

2.3.2 Site rotation

Each site excluding two end sites were allowed to rotate freely under following transformation.

1. Consider a chain as shown in Fig. 2.1.

2. Choose sites i and $k > i + 1$.

3. Range over all $j = i + 1, \ldots, k - 1$

4. For each cylindrical coordinate j,

$$\begin{aligned} \hat{e}_z &= \frac{\vec{r}_k - \vec{r}_i}{|\vec{r}_k - \vec{r}_i|} \\ z_j &= (\vec{r}_j - \vec{r}_i).\hat{e}_z \\ \vec{\rho}_j &= (\vec{r}_j - \vec{r}_i) - z_j.\hat{e}_z \end{aligned} \tag{2.9}$$

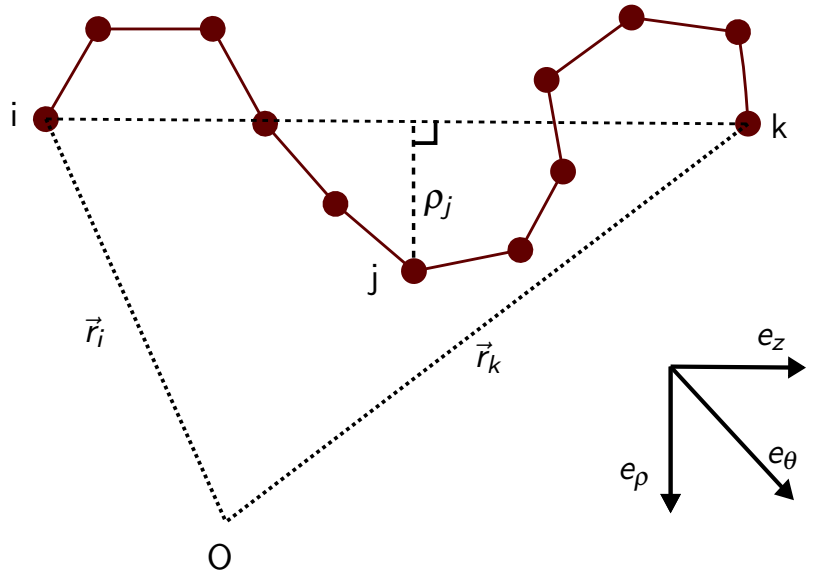

Figure 2.1. Diagrammatic representation of a chain depicting chain parameters and unit vectors in cylindrical coordinate system for site rotation.

5. Rotate $\vec{\rho}_j$ to $\vec{\rho}'_j$ such that

$$\begin{aligned}\vec{\rho}'_j &= \rho_j(\cos\theta\hat{e}_\rho + \sin\theta\hat{e}_\theta) \\ &= \cos\theta\vec{\rho}_j + \rho_j \sin\theta(\hat{e}_j \times \hat{e}_\rho) \\ &= \cos\theta\vec{\rho}_j + \sin\theta(\hat{e}_j \times \vec{\rho}_j)\end{aligned} \tag{2.10}$$

6. Plugging in the value of $\vec{\rho}_j$ from Eq. (2.9) to Eq. (2.10),

$$\vec{\rho}'_j = [(\vec{r}_j - \vec{r}_i) - \hat{e}_z(\vec{r}_j - \vec{r}_i)\cdot\hat{e}_z]\cos\theta + [\hat{e}_z \times (\vec{r}_j - \vec{r}_i)]\sin\theta \tag{2.11}$$

7. Finally the rotated j site position is:

$$\vec{r'}_j = \vec{r}_i + z_j\hat{e}_z + \vec{\rho}'_j \tag{2.12}$$

8. Each j site was allowed to rotate to a position given by Eq. (2.12).

2.3.3 Metropolis algorithm

1. Initialize the chain state, in our case the chain was chosen to be straight.

2. Generate the proposed state by implementing pivot and site rotation.

3. Compute the energy of the proposed state by using Eq. (1.15) and henceforth the transition probability.

4. Generate the random number $x \in [0, 1]$. If the probability is larger than the random number or the energy is lowered the move is accepted. If not, step 2 to 4 is repeated.

5. Once the next step is accepted, values of observables are recorded.

2.3.4 Efficient sampling techniques

To prevent the simulation from getting stuck in local minima, we incorporated some of the sampling techniques like parallel tempering and dynamic biasing force. These are discussed below.

Parallel tempering technique

We used replica exchange parallel tempering [88] as given by the algorithm below.

1. M noninteracting copies of the system are simulated in parallel at different temperatures $T_1, T_2, \ldots, T_M$.

2. After one complete Monte Carlo sweep two copies at neighboring temperatures T_i and T_{i+1} are exchanged with a probability:

$$p[(E_i, T_i) \rightarrow (E_{i+1}, T_{i+1})] = \min\left[1, \exp[(E_{i+1} - E_i)(1/k_B T_{i+1} - 1/k_B T_i)]\right] \tag{2.13}$$

Dynamic Biasing force

Dynamic biasing force was also used as another option for an efficient sampling. The force was applied along the direction of end-to-end length vector. The biased energy hamiltonian has the form in Eq. (2.14),

$$H' = H - \vec{F} \cdot (\vec{r}_{N-1} - \vec{r}_0) \tag{2.14}$$

CHAPTER 3

ESCAPE RATE ANALYSIS IN ONE DIMENSION

3.1 Introduction

In pulling experiments using optical tweezers [82], the determination of landscape features has historically been carried out based on Bell-Evans phenomenological theory [58–60, 67, 83], which assumes that the rate constant $k(F)$ scales up exponentially with applied force from its unperturbed, intrinsic value k_0 according to Eq. (1.6). In what follows, we use conventional notation: $\beta^{-1} = k_B T$ is the thermal energy scale set by the aqueous environment, and $x^{\ddagger}$ is the minimum-to-barrier distance of the effective one-dimensional potential $U(x)$, a continuous (but not necessarily smooth) function of the end-to-end extension.

A common experimental situation involves the application of a pulling force $F = KVt$ that grows linearly in time until the rupture force F_c is reached. Although other pulling protocols are sometimes employed [51, 56, 89–91], we focus on the case of fixed loading rate (KV = constant), and we ignore instrument-specific issues of compliance [57, 92, 93].

It is recognized that a description of pulling experiments based on the Bell-Evans formula for the force-induced rupture rate is in poor accord with results from numerical simulations [61]. The naive thermal-activation picture, represented by Bell-Evans, suffers from various inadequacies that are important to address. To begin, Eq. (1.6) is strictly applicable only in the limit of low pulling rate ($KV \lesssim KV_{\min} = k_0/\beta x^{\ddagger}$) and ultra high barrier ($\Delta G^{\ddagger} \gg F x^{\ddagger}, k_B T$). Even in the moderate pulling regime, it incorrectly predicts the rupture force distribution. It also ignores self-consistency effects in the sense that it does not account for the fact that the distance $x^{\ddagger}$ and the energy barrier $\Delta G^{\ddagger}$ are themselves force-dependent and both diminish with increasing F as the energy landscape is tilted. Nor does it properly account for the shape of the barrier, which plays a vital role in

establishing the escape rate and the nature of the escape trajectory for more modest, biologically relevant barrier heights.

Consequently, there are many situations in which the phenomenological theory incorrectly predicts the results of pulling experiments. It tends to overestimate the rate of rupture $k(F)$ at a given force F and to underestimate the mean and most-probable rupture forces. Hence, when the Bell-Evans rate, $k_{\mathrm{BE}}(F)$, is used as the basis for a fit to experimental data, the extracted parameters, $\Delta G^{\ddagger}$, $x^{\ddagger}$, and k_0, may be incorrectly predicted. Our main concern here lies in the reliable extraction of these physical quantities.

Attempts have been made to improve on Bell-Evans by introducing additional fitting parameters [62, 94], sometimes in an ad hoc way. Dudko and coworkers have tried to make the analysis more rigorous [68]. They calculated $k(F)$ and the corresponding probability density of the rupture force $p(F_c)$ within the framework of Kramer's Theory [34] for two specific free energy surfaces—the cusp surface and the linear cubic surface—and showed that these two examples can be subsumed into a single result [appearing as Eq. (1.7) in this document and as Eq. (3) in Ref. 68], with interpolation provided by a shape parameter ν. This encompasses the Bell-Evans result, since $k_{\mathrm{D}}(F) \to k_{\mathrm{BE}}(F)$ as $\nu \to 1$. It is clear, however, that for all $\nu \neq 1$, Eq. (1.7) has a dangerous point of nonanalyticity. The vanishing of the rate $k_{\mathrm{D}}(F) \to 0$ as $F \to \Delta G^{\ddagger}/x^{\ddagger}\nu$ (for shape parameters in the range $0 < \nu < 1$) is manifestly unphysical; hence the Dudko expression is only appropriate for the pulling regime in which $F \ll \Delta G^{\ddagger}/x^{\ddagger}\nu$. In fact, the region of validity is more constrained still, since we should further require that the escape rate grow with pulling force. As it turns out, the function $k_{\mathrm{D}}(F)$ is monotonically increasing only for up to the force threshold given by Eq. (1.8).

We pursue a different approach that produces no nonanalyticity and no obviously unphysical behavior. We compute $\log k(F)/k_0$ order by order in the pulling force. Rather than truncate the expansion, we approximate the higher order terms as a resummation by geometric series—similar in spirit to the Random Phase Approximation or the infinite summation of ladder diagrams in

many-body theory—which yields

$$k(F) = k_0 \exp\left(\frac{\beta F x^\ddagger}{1 + F/2\kappa^\ddagger x^\ddagger} \right). \tag{3.1}$$

Here, $\kappa^\ddagger$ is the reduced curvature of the well and barrier. The route to Eq. (3.1) is nothing more than a mathematical trick, but it rather elegantly cures the ill behavior of a truncated expansion, and it fortuitously leads to a closed-form expression for the cumulative probability distribution.

Our attempts to benchmark Eq. (3.1) fall into two categories: prediction and parameter extraction, which correspond to the forward and inverse problems. In the forward direction, we determine the escape rates and the cumulative probability distribution of the critical force following the numerical method described in Sec. 5.3. We compare the simulated behavior to the various analytical predictions. We find that our proposal outperforms the Bell-Evans and Dudko expressions, across many different choices of energy landscape and over a broad range of pulling rates. In the inverse direction, analytical forms for the cumulative probability distribution $P(F_c)$ are fit to the simulated data to extract the optimal values of the intrinsic parameters k_0, $x^\ddagger$, and $\kappa^\ddagger$.

The results we achieve are compelling. The values of the three parameters that we extract are in excellent agreement with the actual values that characterize the underlying energy landscape. Moreover, the agreement appears to hold over an unexpectedly large range of pulling rates, with $KV/KV_{\min}$ spanning six or seven orders of magnitude.

In contrast, fits of simulation data to the Bell-Evans cumulative probability distribution, insofar as they are able to produce good values of k_0 and $x^\ddagger$ at all, only do so at the very slowest pulling rates. It is difficult to speak definitively of how well Dudko's expression performs, since in that context fits must be carried out in conjunction with a force cutoff somewhere below the point of nonanalyticity. This is an unwelcome complication. The cutoff itself introduces a significant element of uncertainty in the fit, since where best to put the cutoff cannot be determined if the landscape is not yet known.

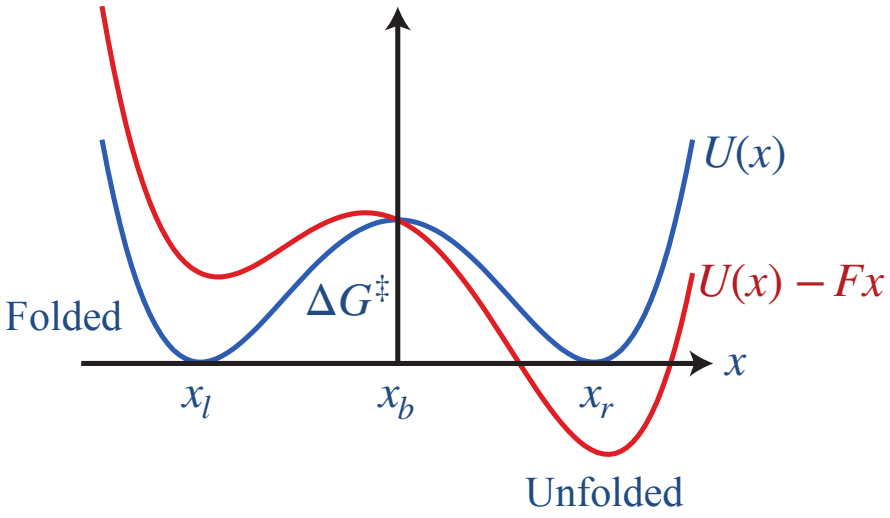

Figure 3.1. (Blue) The double-well potential has equilibrium positions at x_l and x_r, separated by a barrier at x_b. A particle escaping from left to right experiences a barrier of height $\Delta G^{\ddagger} = U(x_b) - U(x_l)$, peaked at a distance $x^{\ddagger} = x_b - x_l$ from the bottom of the left well. (Red) After application of a pulling force F, the energy landscape has tilted to favor the destination well on the right. Observe that the well positions have shifted and that the height of the barrier holding the particle in the left well has decreased.

3.2 Formal development

Kramers theory tells us that the escape rate depends weakly (polynomially) on the curvature at the bottom of the well and the top of the barrier but strongly (exponentially) on the height of the apparent energy barrier in the direction of travel [34, 37]. We consider a double well potential $U(x)$, with wells at positions x_l and x_r separated by a barrier at x_b ($x_l < x_b < x_r$), as illustrated in Fig. 4.1. The well escape rate from left to right is given by $k_0 \sim \exp(-\beta\Delta U)$, where $\Delta U = U(x_b) - U(x_l)$.

We allow for a pulling force F that tilts the potential landscape according to

$$\tilde{U}(x) = U(x) - Fx. \tag{3.2}$$

The corresponding rate equation becomes

$$k(F) \sim \exp\left[-\beta\left(\tilde{U}(x_b + \delta x_b) - \tilde{U}(x_l + \delta x_l)\right)\right], \tag{3.3}$$

where δx_l and δx_r denote the shifts in the well positions as a result of the tilt. Taylor expansions of the extremal conditions $\tilde{U}'(x_l + \delta x_l) = 0$ and $\tilde{U}'(x_b + \delta x_b) = 0$ around x_l and x_b up to first order in δx_l and δx_b give $\delta x_l = F/U''(x_l) = F/\kappa_l$ and $\delta x_b = F/U''(x_b) = -F/\kappa_b$. A further expansion of $\tilde{U}(x_b + \delta x_b)$ and $\tilde{U}(x_l + \delta x_l)$ around x_b and x_l, respectively, up to second order in F, yields a rate equation of the form

$$k(F) = k_0 \exp\left[\beta F x^\ddagger \left(1 - \frac{F}{2\kappa^\ddagger x^\ddagger}\right)\right]. \tag{3.4}$$

Here, $x^\ddagger = x_b - x_l$, and $\kappa^\ddagger$ is given by Eq. (1.5).

Successive terms in the expansion of $\log k(F)/k_0$ have alternating sign, which is important for proper convergence of the series. Indeed, there is no polynomial expression, arising as a truncation of the series at finite order, that does not either substantially over- or undershoot the true rate for large applied F. The negative-prefactor terms at even powers of F are particularly troublesome, because they lead to nonmonotonicity. As a workaround, we make use of the idea of infinite resummation, $1 - \epsilon + \epsilon^2 - \cdots \approx 1/(1+\epsilon)$, which transforms Eq. (3.4) into Eq. (3.1), at least up to discrepancies at $O(F^3)$. The transformed expression is well-behaved everywhere and displays no obviously unphysical behavior. See Fig. 3.2. Moreover, it leads to a closed-form expression for the cumulative probability distribution (with the correct normalization $P(F_c) \to 1$ as $F_c \to \infty$; Dudko's expression, in contrast, cannot be properly normalized).

In the usual adiabatic limit, the expression for the cumulative probability distribution of the rupture force is given by

$$P(F_c) = 1 - \exp\left[-\int_0^{F_c} \frac{dF}{\dot{F}} k(F)\right]. \tag{3.5}$$

Equations (1.6) and (3.5) together give the cumulative probability distribution of the rupture force as predicted by the Bell-Evans phenomenological model,

$$P_{\mathrm{BE}}(F_c) = 1 - \exp\left[\frac{k_0}{KV\beta x^\ddagger}\left(1 - e^{\beta F_c x^\ddagger}\right)\right]. \tag{3.6}$$

If instead we put Eq. (3.1) into Eq. (3.5), we get a more complicated result, but one that is still

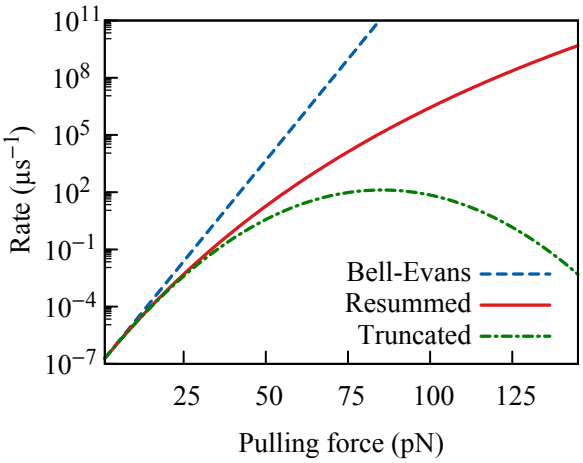

Figure 3.2. The well escape rate $k(F)$ is plotted against the applied pulling force F. The upper (bashed blue) curve corresponds to the Bell-Evans (BE) rate [Eq. (1.6)]; the middle (solid red) to our proposed infinite-resummation expression [Eq. (3.1)]; and the lower (dot-dashed green) to an expansion truncated at second order in the pulling force [Eq. (3.4)]. The BE result grows exponentially without bound (but shows as a straight line because of the log-linear scale). The truncated expression turns over and becomes unphysical around 80 pN. The resummed form strikes a middle course, growing monotonically but saturating at a large, finite value, $k_0 \exp\left[2\beta\kappa^{\ddagger}(x^{\ddagger})^2\right]$.

simple enough to use for fitting (e.g., via Marquardt-Levenberg):

$$P(F_c) = 1 - \exp\left[\frac{k_0}{KV}\left(F_1 + F_2 - 2x^{\ddagger}\kappa^{\ddagger}\right)\right]. \tag{3.7}$$

The quantities F_1 and F_2 have units of force and are explicit functions of the critical value F_c:

$$\begin{aligned} F_1 &= \left(F_c + 2x^{\ddagger}\kappa^{\ddagger}\right)\exp\left(\frac{2F_c x^{\ddagger 2}\beta\kappa^{\ddagger}}{F_c + 2x^{\ddagger}\kappa^{\ddagger}}\right), \\ F_2 &= 4x^{\ddagger 3}\beta\kappa^{\ddagger 2}\exp\left(2x^{\ddagger 2}\beta\kappa^{\ddagger}\right)\left[\mathrm{Ei}\left(-\frac{4x^{\ddagger 3}\beta\kappa^{\ddagger 2}}{F_c + 2x^{\ddagger}\kappa^{\ddagger}}\right) - \mathrm{Ei}\left(-2x^{\ddagger 2}\beta\kappa^{\ddagger}\right)\right]. \end{aligned} \tag{3.8}$$

The exponential integral $\mathrm{Ei}(x) = -\int_{-x}^{\infty} dt\, t^{-1}e^{-t}$ is a standard special function that is available in most data analysis software.

The choice $F = KVt$ is helpful here but not essential. Its main advantage is that the differential appearing in Eq. (3.5) simplifies to $dF/\dot{F} = (KV)^{-1}dF$, and hence the integration measure is trivial. The closed form expression that we obtain in Eqs. (3.7) and (3.8) does depend

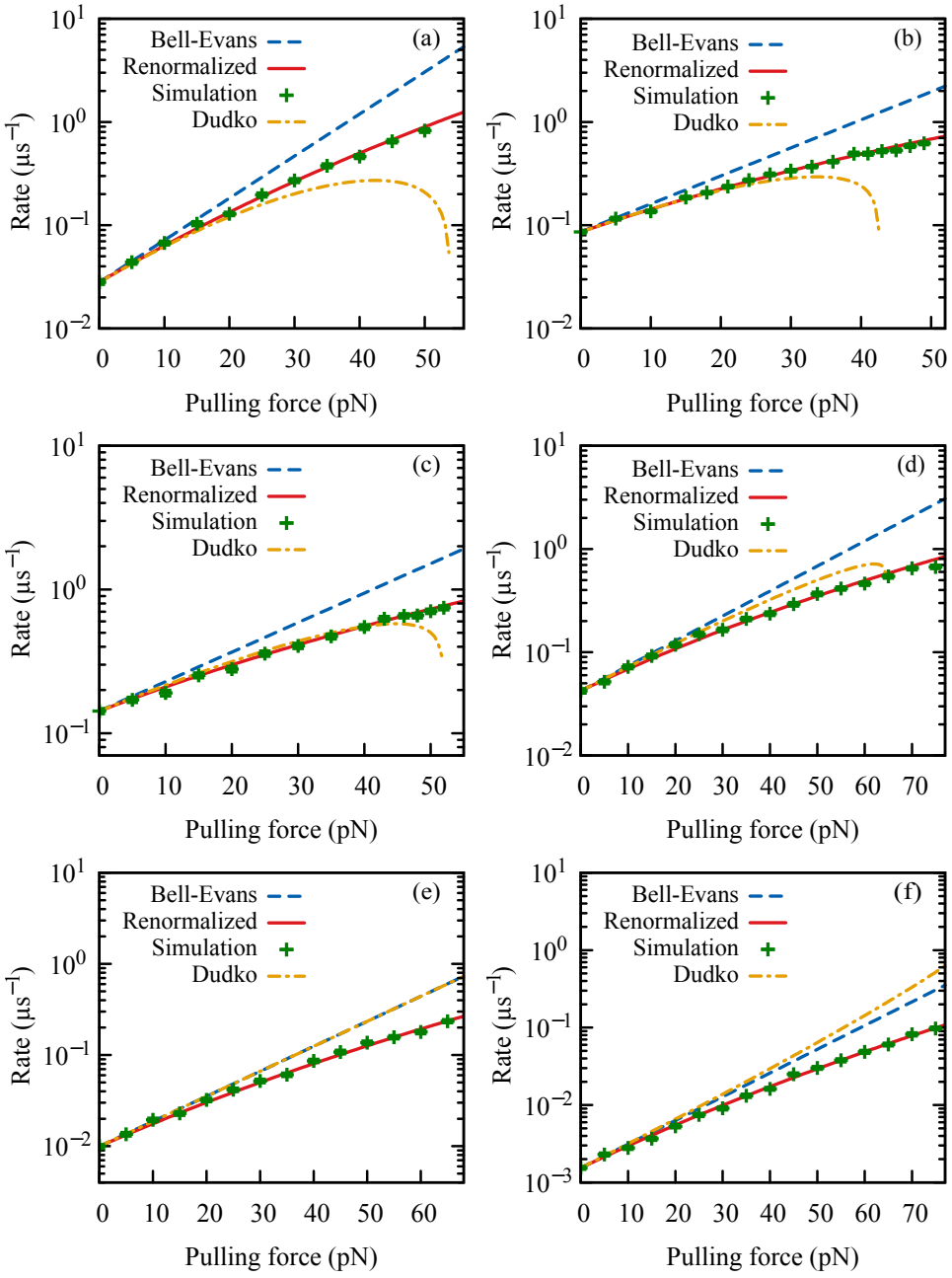

Figure 3.3. Numerical measurements of the escape rate (green data points with error bars) are plotted versus the applied pulling force. Also shown for comparison are the predictions of Bell-Evans [Eq. (1.6), blue dashed line], Dudko [Eq. (1.7), orange dot-dashed], and our renormalized rate equation [Eq. (3.11) with a common value $\alpha = 1/3$, solid red]. The simulations were carried out for potentials with various values of $\nu = 2\Delta G^{\ddagger}/\kappa^{\ddagger}(x^{\ddagger})^2$, the shape parameter: in the top row, panels (a), (b), (c) correspond to $\nu = 0.66, 0.75, 0.82$; in the bottom row, (d), (e), (f) correspond to $\nu = 0.9, 1.0, 1.1$. We note the remarkable agreement between simulation and the renormalized form. No fitting is involved.

on this choice. But any pulling schedule $F(t)$ that is monotonically increasing (so that $\dot{F}$ never vanishes or goes negative) and growing at most as a polynomial in t can be treated similarly.

We now comment on the connection to the prior work of Dudko and coworkers. The unperturbed potential $U(x)$ can be expanded to quadratic order around the bottom of the well, $U_l(x) = U(x_l) + (\kappa_l/2)(x - x_l)^2$, and around the peak of the barrier, $U_b(x) = U(x_b) - (\kappa_b/2)(x - x_b)^2$. We identify the position $x^* = (\kappa_b x_b + \kappa_l x_l)/(\kappa_l + \kappa_b)$ where the two approximations take a common slope and match the functions smoothly there. The resulting piecewise composite curve has a total rise of

$$U_l(x^*) - U(x_l) + U_b(x^*) - U(x_b) = \frac{\kappa_l \kappa_b (x_b - x_l)^2}{2(\kappa_l + \kappa_b)} = \frac{1}{2}\kappa^\ddagger (x^\ddagger)^2, \tag{3.9}$$

which differs from the the true barrier height $\Delta G^\ddagger = U(x_b) - U(x_l)$ by a factor that Dudko labels $1/\nu$. That is,

$$\frac{\Delta G^\ddagger}{\nu} = \frac{1}{2}\kappa^\ddagger (x^\ddagger)^2. \tag{3.10}$$

The equality $\nu = 2/3$ holds for any degree-three polynomial. If the energy landscape is represented by a higher-degree polynomial, then the value of the shape parameter is idiosyncratic and should be viewed as drawn from a distribution with average $\langle 1/\nu \rangle < 3/2$. For smooth potentials (no cusps or discontinuities), typical values of the shape parameter ν range between $2/3$ and ≈ 1.1. An advantage of working in terms of ν, rather than the effective curvature $\kappa^\ddagger$, is that the former can be defined even if the derivatives $U''(x_l)$ and $U''(x_b)$ vanish (e.g., a quartic well or barrier) or are not well defined (e.g., a cusp barrier).

With Eq. (3.10) in mind, matching our resummed rate expression to that of Dudko order by order in the small-pulling-force, large-barrier-height limit suggests the form

$$k(F) = k_0 \exp\left[\frac{\beta F x^\ddagger}{(1 + \alpha/\beta\Delta G^\ddagger)(1 + \nu F x^\ddagger/4\Delta G^\ddagger)}\right], \tag{3.11}$$

where $\alpha > 0$ is a pure number with a weak dependence on the shape parameter. Equation (3.11) can be understood as a rewriting of Eq. (1.6), the Bell-Evans phenomenological rate, with an upward renormalization of the temperature, $\beta \to \beta/(1 + \alpha/\beta\Delta G^\ddagger)$, and a downward renormalization of

the barrier distance $x^\ddagger \to x^\ddagger/(1 + \nu F x^\ddagger/4\Delta G^\ddagger)$. Unlike Eq. (1.7), Eq. (3.11) is well-behaved everywhere.

In the case of an ultra-high barrier, defined by the double limit $\beta\Delta G^\ddagger \gg 1$ and $\Delta G^\ddagger \gg F x^\ddagger$, Eq. (3.11) reduces to Eq. (1.6). For more modest barriers or higher temperatures, one or both of the factors $(1 + \alpha/\beta\Delta G^\ddagger)$ and $(1 + \nu F x^\ddagger/4\Delta G^\ddagger)$ may differ appreciably from 1; this allows the rate expression to become aware of the details of the barrier's height and shape through the factor $\Delta G^\ddagger/\nu$.

The reliability of Eq. (3.11) was tested for six potential landscapes with different values of ν using the simulation scheme described in the next section. In every test example (see Fig. 3.3), our renormalized equation closely tracked the empirical escape rate determined from simulations. It noticeably outperformed the Bell-Evans and Dudko escape rate equations.

3.3 Numerical Simulations

The reaction coordinate x was made to execute Langevin dynamics according to Eq. (2.1). This was implemented using a modern reformulation [85] of the Verlet algorithm [86]. We mimicked the experimental situation by assuming stochastic motion of a molecule of effective mass $m = 2\,\mathrm{pg}$ in a biquadratic potential. The data that appear in Figs. 3.4–3.7 correspond to the choice $U(x) = 4x^4 - 32x^2 + 64$ (with x measured in nm and U in pN nm). The molecule was assumed to be pulled from two ends along the reaction coordinate x by a laser potential with force constant K and pulling velocity V; i.e., with an instantaneous force $F = KVt$ that increases linearly in time. For the given potential, the energy barrier was $\Delta G^\ddagger = 64\,\mathrm{pN\,nm}$, the minimum-to-barrier distance $x^\ddagger = 2\,\mathrm{nm}$, and the effective curvature $\kappa^\dagger = 42.7\,\mathrm{pN\,nm^{-1}}$. The stochastic forces $\xi(t)$ on the molecule were drawn randomly from a Gaussian distribution of width $(2m\gamma k_B T\delta t)^{1/2}$ with $k_B T = 4.1\,\mathrm{pN\,nm}$, $\gamma = 7\,\mu\mathrm{s^{-1}}$, and a discrete timestep δt ranging from $10^{-2}\,\mu\mathrm{s}$ to $10^{-6}\,\mu\mathrm{s}$.

Note that, for generality, small inertial effects were included in the numerics. The simulations were not run in the strongly over-damped, diffusion-only limit: parameter values were chosen to be physically plausible but also to produce a non-extreme limit (neither $\gamma \ll \omega_b$ nor $\gamma \gg \omega_b$) of

the prefactor to the exponential in the Kramers rate [which will appear in Eq. (3.12)].

Pulling rates for the force $F = KVt$ are measured with respect to $KV_{\min} = k_0/\beta x^{\ddagger}$, which is the minimum rate for effectual pulling. Below $KV_{\min}$, the probability density $p(F_c)$ is peaked at $F_c = 0$; the particle escapes the well on its own before the applied force has appreciably modified the energy landscape. On the other hand, for rates above $KV/KV_{\min} \approx 10^6$, the barrier vanishes too quickly, long before the particle has moved any significant distance. Accordingly, we worked in the regime of pulling rates between these two extremes.

The simulation was initialized in the left well by drawing starting values of velocity v and position x from the distributions $e^{-\beta m v^2/2}$ and $e^{-\beta U(x)}\Theta(x_b - x)$, respectively, so that the each simulation began fully thermalized. The simulation flagged the value of pulling force at which x convincingly crossed the barrier or the barrier vanished; we took this to be the rupture or critical force F_c. For each value of the pulling rate KV, the simulation was carried out 2500 times, each run generating a unique value of the rupture force. The cumulative probability distribution $P(F_c)$ was constructed in the standard way—by sorting the measured rupture forces in ascending order and then pairing them with a uniform grid of values running from 0 to 1. The plot for $P(F_c)$ so obtained was tested against Eq. (3.7) and against the Bell-Evans form, Eq. (3.6). The process was repeated for pulling rates ranging from $KV = 10^{-7}\,\mathrm{pN}\,\mu\mathrm{s}^{-1}$ to $0.6\,\mathrm{pN}\,\mu\mathrm{s}^{-1}$ (roughly $1 \lesssim KV/KV_{\min} \lesssim 10^7$) to determine how these expressions fare in the slow, intermediate, and fast pulling regimes.

In order to test parameter extraction, the original $P(F_c)$ dataset for each pulling rate was bootstrapped 100 times to generate 100 new instantiations. These data were fitted with Eq. (3.7) to extract the intrinsic parameters of the potential landscape: k_0, $x^{\ddagger}$ and $\kappa^{\ddagger}$. The spread in fit values was used to generate error estimates.

The datasets were also fitted to the Bell-Evans form given by Eq. (3.6) in order to extract the values of k_0 and $x^{\ddagger}$ ($\kappa^{\ddagger}$ does not appear in the Bell-Evans expression). The bootstrap-average values of the extracted parameters were compared to their known values. The theoretical intrinsic

rate k_0 was computed according to the usual Kramers result,

$$k_0 = \frac{\omega_l}{2\pi} \frac{\sqrt{\gamma^2/4 + \omega_b^2} - \gamma/2}{\omega_b} \exp\left(-\beta \Delta G^{\ddagger}\right). \tag{3.12}$$

Our test potential corresponded to $\omega_l = \sqrt{\kappa_l/m} = 8\,\mu\text{s}^{-1}$ and $\omega_b = \sqrt{\kappa_b/m} = 5.65\,\mu\text{s}^{-1}$. We verified that the theoretical value of $k_0 = 1.192 \times 10^{-7}\,\mu\text{s}^{-1}$ was in agreement with numerical measurements of the escape rate for the nontilted energy landscape.

3.4 Results and Conclusions

In the left column of Fig. 3.4, the rupture force distributions predicted by Eqs. (3.6) and (3.7) are compared to the results from simulation for three different pulling rates (corresponding to $KV/KV_{\text{min}} \approx 10^1, 10^3, 10^5$). For slow pulling (top row), the Bell-Evans theory and our resummed expression are well-matched to each other and to the numerics. For intermediate pulling (middle row), the Bell-Evans result begins to deviate significantly, whereas our proposal continues to give accurate results (i.e., the solid green and red dotted lines coincide). Only at the highest pulling rates (bottom row) do we find significant deviation from the simulated rupture force distributions for both Eqs. (3.6) and (3.7); although, even there, our expression performs better and is in good agreement up to $\sim 25\,\text{pN}$.

It is instructive to look at the corresponding probability density of the rupture force, $p(F_c) = P'(F_c)$, obtained from Bell-Evans and our resummed form, as shown in the right column of Fig. 3.4. The Bell-Evans result systematically underestimates the pulling force required to traverse the barrier—and increasingly so for faster pulling. One observes that both its peak (typical rupture force) and its overall weight (mean rupture force) are positioned too far to the left (toward low force values). The same information is contained in the average critical force $\langle F_c \rangle$, which we obtained from the cumulative probability distributions, Eqs. (3.6) and (3.7), by numerical integration. Figure 3.5 shows a plot of $\langle F_c \rangle$ as a function of the relative pulling rate. One can readily identify an intermediate regime ($10^2 \lesssim KV/KV_{\text{min}} \lesssim 10^5$) in which the curve computed

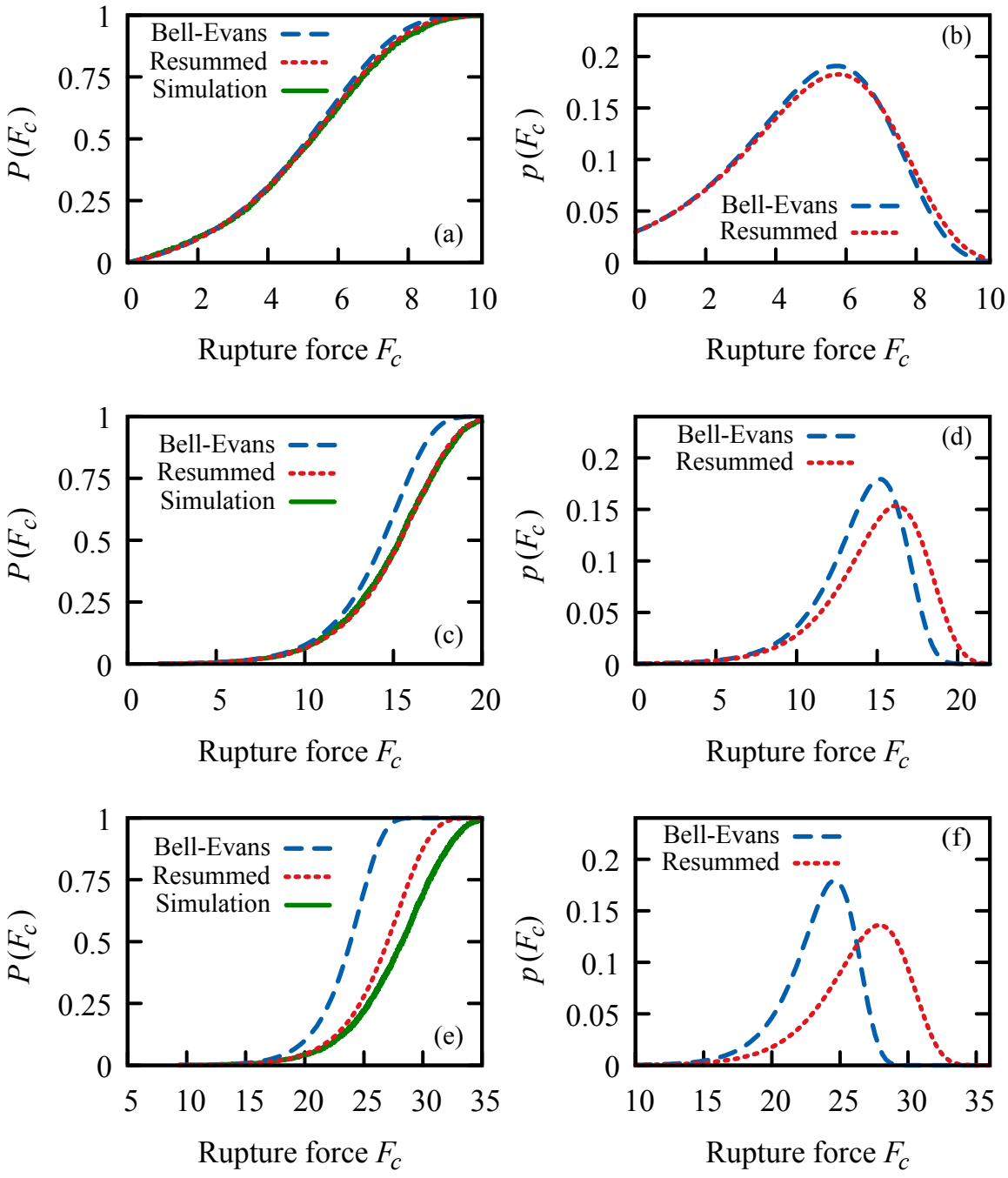

Figure 3.4. Plots paired on the left and right show the cumulative probability distribution $P(F_c)$ and the corresponding probability density $p(F_c) = P'(F_c)$ of the rupture force. Each row shows results for successively faster pulling rates: $KV = 4\times10^{-6}$ pN μs^{-1} for (a) and (b), 4×10^{-4} pN μs^{-1} for (c) and (d), and 4×10^{-2} pN μs^{-1} for (e) and (f).

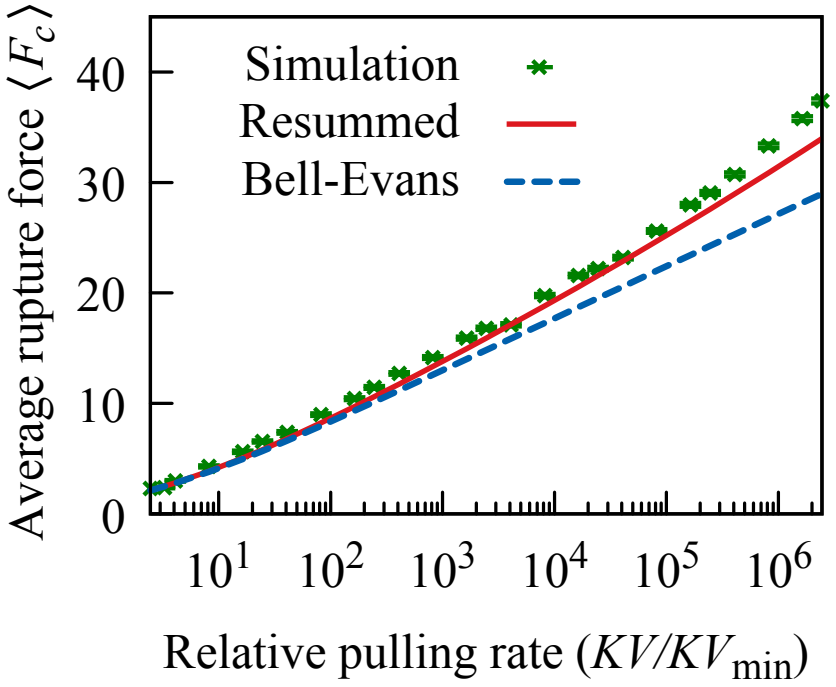

Figure 3.5. The average rupture force $\langle F_c \rangle = \int dF\, FP'(F)$, determined by numerical integration with $P(F)$ taken from Eqs. (3.6) (dashed blue line) and (3.7) (red line), is compared to the empirical values from simulation (green crosses).

from the resummed rate tracks the true, numerically determined values of the average rupture force. In that same regime, the Bell-Evans curve deviates significantly.

The second part of the numerical analysis focused on the inverse problem. Here, the simulated data were fitted using Eq. (3.7), and the intrinsic parameters of the energy landscape, viz., k_0, $x^\ddagger$ and $\kappa^\ddagger$, were determined by minimizing discrepancies between theory and data in the least-squares sense. The process was repeated for Eq. (3.6), but only with k_0 and $x^\ddagger$ (since $\kappa^\ddagger$ does not appear in the fitting function). We found unambiguously that the parameter extraction is much more reliable using our resummed form. Indeed, use of the Bell-Evans theory was often quite misleading, because it would produce an apparently good fit that corresponded to incorrect values of the landscape parameters.

The top panel of Fig. 3.6, which shows a fast-pulling example with $KV = 4 \times 10^{-2}\,\mathrm{pN}\,\mu\mathrm{s}^{-1}$,

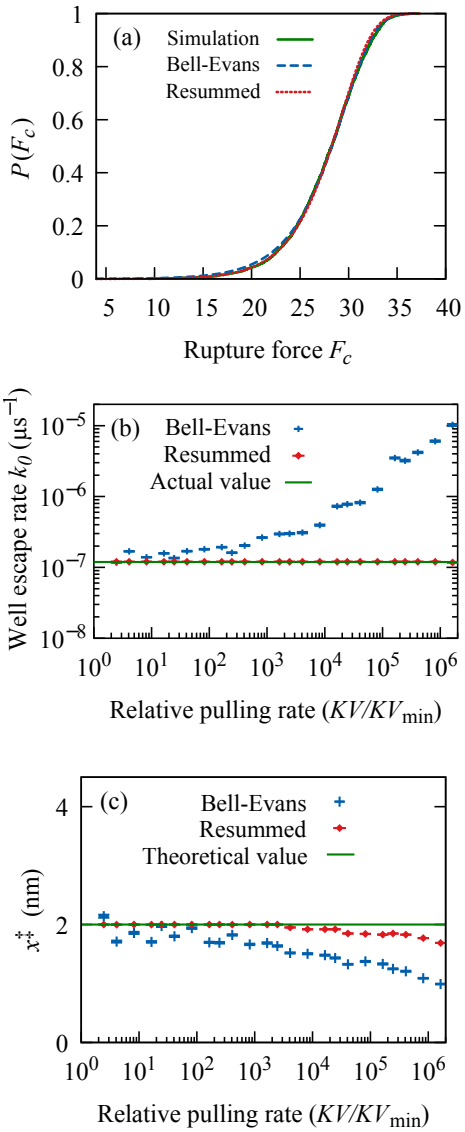

Figure 3.6. (a) The cumulative probability distribution of the rupture force, computed from 2500 simulated pulling experiments at rate $KV = 0.04\,\mathrm{pN}/\mu\mathrm{s}$ (green line), is plotted alongside the best fits for Eqs. (3.6) (blue dashed line) and (3.7) (red dotted line). The near indistinguishability of the curves illustrates the strong tendency toward overfitting. The Bell-Evans expression, though ill-suited for describing the behavior at this high pulling rate, is able to mimic the numerical data—but at the cost of producing fitting parameters that have drifted far from their true values. This is in contrast to the poor agreement in Fig. 3.4(e), where there is no fitting and the known values of k_0 and $x^\ddagger$ are used. Estimates of the intrinsic escape rate k_0 (b) and the barrier distance $x^\ddagger$ (c), as determined from fits of Eqs. (3.6) (blue crosses) and (3.7) (red diamonds) to simulation data over a range of pulling rates, are plotted alongside the actual value (green line).

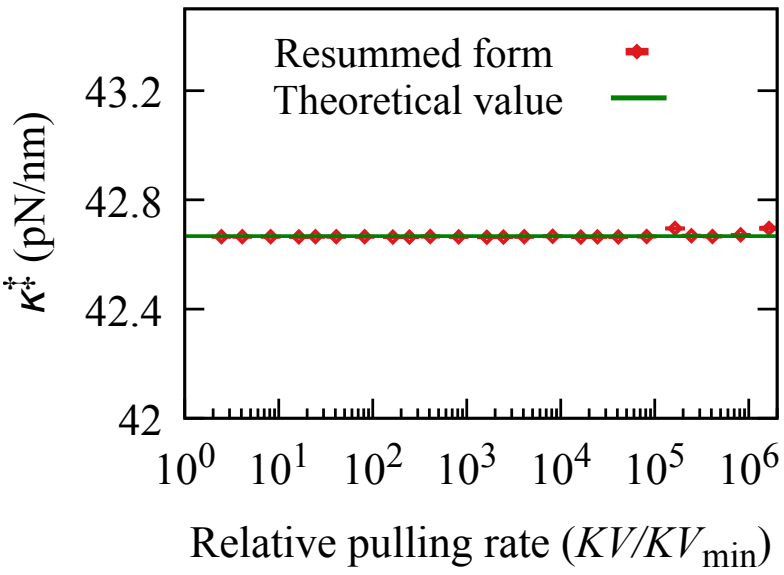

Figure 3.7. The plotted points (red diamonds) are estimates of the reduced curvature $\kappa^{\ddagger}$, as determined from fits of Eq. (3.7) to simulation data. They compare favorably to the actual value (green line) over a range pulling rates spanning many decades.

emphasizes this point. The cumulative probability distribution appears to be equally well fit by Eqs. (3.6) and Eq. (3.7). The middle and bottom panels reveal this to be illusory. In the Bell-Evans analysis, the value of k_0 is systematically overestimated and $x^{\ddagger}$ underestimated, and both ever more so as the pulling rate is ramped up. On the other hand, the analysis based on our resummed form yields values consistent with the correct landscape parameters. Moreover, even at low pulling rates, where Bell-Evans performs not too badly, our proposal is more reliable and produces less scatter in the parameter values.

We remark that fits of the simulation data to Eq. (3.7) yield astonishingly good values of $\kappa^{\ddagger}$, the effective curvature. See Fig. 3.7. In almost every case, regardless of pulling rate, the predicted value of $\kappa^{\ddagger}$ coincides with the true value. This suggests to us that our inclusion of higher-order corrections in the rate equation plays an important role in improving the overall quality of the parameter extraction.

To conclude, our work highlights the known inadequacies of the Bell-Evans phenomeno-

logical well escape rate. It also suggests that the celebrated equation due to Dudko and coworkers is not an adequate fix. We propose a new expression, Eq. (3.1), that improves on Bell-Evans by including beyond-Arrhenius contributions from the shape of the energy potential. Equation (3.1) clearly outperforms the Bell-Evans and Dudko expressions in terms of predicting the well escape rate (as is evident from Fig. 3.3). Crucially, it avoids the unphysical behavior that plagues Dudko's rate equation at large pulling force.

Of particular utility is that Eq. (3.1) integrates to give a manageable, closed-form expression for the cumulative probability distribution. The resulting Eq. (3.7) is straightforward to implement as a fitting function and can be incorporated into existing workflows with little additional effort. Rigorous numerical tests (illustrated in Figures 3.6 and 3.7) confirm that fits to Eq. (3.7) can be used to reliably extract the parameters that characterize the underlying energy landscape.

CHAPTER 4

UNIVERSALITY IN BIASED ACTIVATED BARRIER CROSSING

4.1 Introduction

The purpose of this chapter is to describe universal aspects of the biased activated-barrier-crossing process that we have uncovered in numerical simulations of various one-dimensional potentials. Our work points the way to an alternative data analysis technique that would allow for the determination of otherwise unknown landscape details by overlaying data from multiple experiments and adjusting free parameters until the scattered data align along a common curve.

The concept of universality comes to us from the study of critical phenomena [95]. In that context it allows us to understand how phase transitions can be characterized and grouped into families according to common critical exponents, wholly independent of the microscopic details of the underlying models; it also explains the existence of scaling relations that govern how thermodynamic quantities behave in the vicinity of criticality. An important mark of universality is that data from different models or different physical systems can be plotted in reduced variables so that they collapse onto a single universal curve [96–98].

Criticality has previously been invoked by Singh, Krishan, and Robinson in the context of the unbiased-activated-barrier crossing problem [99, 100]. They considered the non-Markovian crossing of a quadratic barrier, where the frictional term in the Langevin equation includes a memory kernel with a long time scale. The authors proposed a scaling hypothesis, making analogy with the criticality of the Ising model, and were able to derive scaling relations for the reduced rate near a critical value of the memory kernel time scale.

Our approach here is rather different. We focus on the relative change in the escape rate as a function of an applied pulling force—both for uniform pulling (F constant) and steady loading

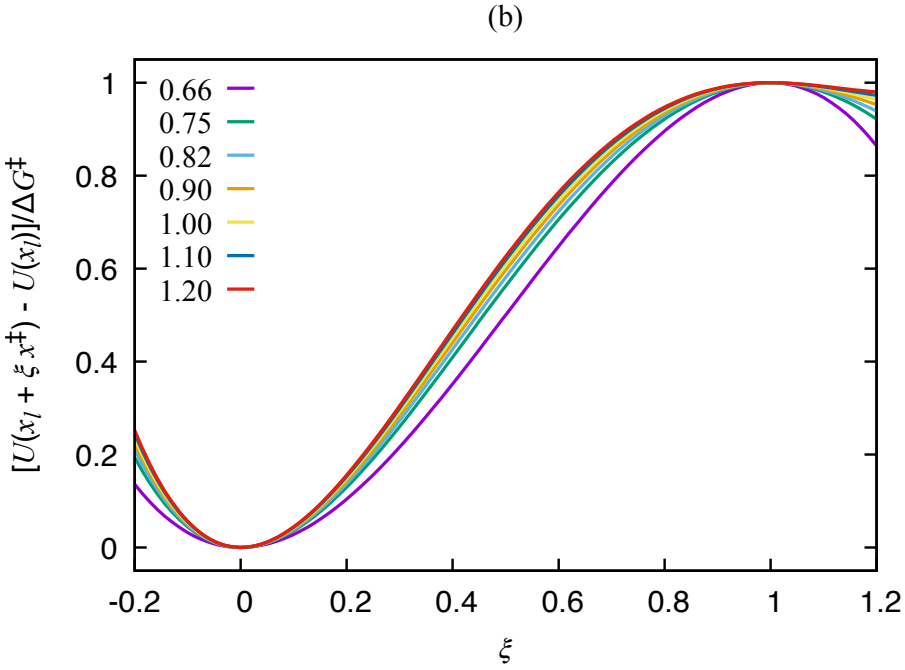

Figure 4.1. Seven energy profiles are depicted, rescaled so that the bottom of the well and top of the barrier coincide. The color key shows the shape parameter (ν) values for each curve.

($F = KVt$ with KV constant). We propose that F exists alongside two other important force scales and that the two independent ratios that can be formed serve as arguments to a scaling function. We have carried out Langevin-type simulations of a particle in a one-dimension energy potential, coupled to a heat bath. Many thousands of instantiations provide us with a large data set that offers good coverage of the model space. What is so striking is the almost unreasonable effectiveness of the scaling ansatz, which appears to be valid over a huge variety of well shapes and barrier heights and over loading rates spanning many orders of magnitude.

4.2 Scaling ansatz

We argue that the barrier-crossing process is controlled by the relative magnitudes of three intrinsic force scales: the typical thermal force that provides the kick out of the well ($F_T \approx 1/\beta x^{\ddagger}$); the larger applied force required to fully extinguish the barrier ($F_B \approx \kappa^{\ddagger} x^{\ddagger}$); and the pulling force used as an external bias (F). In our notation, β is the inverse temperature, and $x^{\ddagger}$, $\kappa^{\ddagger}$ are the barrier

distance (see Fig. 4.1) and effective curvature [84]. In particular, we propose that the rescaled, logarithmic relative escape rate $(F_T/F_B)\log[k(F)/k_0]$, when plotted against the reduced pulling force F/F_B, collapses onto a universal curve. The function $k(F)$ is the escape rate associated with the potential landscape under bias, and k_0 is the corresponding rate in the untilted landscape.

More precisely, the claim is that

$$\begin{aligned} Y(F) = \log\frac{k(F)}{k_0} &= \left(\frac{F_T}{F_B}\right)^{-1} \mathbb{Y}(F/F_B, F_T/F_B) \\ &= \left(\frac{F_T}{F_B}\right)^{-1} \left[\mathbb{Y}(F/F_B, 0) + \left(\frac{F_T}{F_B}\right)^{\omega} \mathbb{W}(F/F_B) + \cdots\right]. \end{aligned} \tag{4.1}$$

Up to subleading corrections (characterized by an exponent $\omega > 0$), the escape behaviour is controlled by a universal function $\mathbb{Y}(x, y)$ that satisfies $\mathbb{Y}(x, 0) = x + O(x^2)$. Further justification for this form is presented in Sec. 4.4. The implication of Eq. (4.1) is that a plot of $(F_T/F_B)Y$ versus $f = F/F_B$ should produce data collapse regardless of the microscopic details of the simulation.

In the context of dynamical pulling, there is another useful analysis. A population of particles trapped in the originating well is depleted according to $-dn/dt = k(KVt)n(t)$, a product of the instantaneous escape rate and the current population. The half-life of such a population is characterized by $\log 2 = \int_1^{1/2} dn/n = -(1/KV)\int_0^{\hat{F}} dF\, k(F)$. Here, $\hat{F} = KV\hat{t}$ is the typical applied force that is in effect during barrier transit, and $\hat{t}$ is the median elapsed time for escape. It follows from Eq. (4.1) that $\hat{F}$ (measured with respect to the thermal force F_T) must be a monotonic, universal function of $\dot{F} = KV$ (measured with respect to k_0F_T, a loading rate threshold defined by the thermal processes in the potential well). Hence, there is an additional data collapse analysis that can be used to independently test the validity of the scaling hypothesis.

In our numerical experiments, the external bias is applied in two ways: (i) as a time-invariant pulling force of constant strength and (ii) as a linearly time-varying force with a constant loading rate. In the case of constant pulling, the system is prepared in the equilibrium state of the tilted energy profile [viz. $\tilde{U}(x) = U(x) - Fx$] and remains in thermal equilibrium throughout the simulation. In the case of steady loading, the system is prepared in the equilibrium state of

the unbiased profile ($F = 0$ for all $t \leq 0$), but as time elapses it is driven away from equilibrium ($F = KVt$ for all $t > 0$) in proportion to how much KV exceeds $k_0 F_T$.

In both cases, the role of F is to gently tilt the landscape (statically or dynamically), as depicted in Fig 1.5. There, the purple curve depicts the potential profile in its unbiased state; the green curve shows the profile after application of the external bias. Generically, the force-dependent values of the barrier distance $x^{\ddagger}(F)$ and barrier height $\Delta G^{\ddagger}(F)$ are monotonically decreasing in F, and hence the barrier crossing process becomes energetically less costly (and crossing events more frequent) as the external bias is ramped up.

4.3 Numerical results

We carried out a thorough and comprehensive Langevin simulation study. At the start of each run, the system was prepared in a properly equilibrated state: an initial position and velocity were drawn from the heat bath distribution of the appropriate energy profile, with the constraint that the particle be situated on the originating-well side of the barrier. Forward evolution was carried out with adaptive time steps taken small enough that the discretization error could be shown to be negligible. The simulation made use of a high-quality, long-period pseudorandom number generator that guaranteed the statistical independence of the instantaneous thermal forces.

We considered seven different potentials having shape parameter [68] $\nu = 0.66$, 0.75, 0.83, 0.9, 1, 1.1, 1.2; these values step through the full range of possibilities for smooth potentials based on polynomials. This family of energy potentials—translated and rescaled to coincide at the bottom of the originating well and at the top of the barrier so as to emphasize the shape difference—is displayed in the lower panel of Fig 4.1. We also considered eight barrier regimes, with $1/\beta\Delta G^{\ddagger} = k_B T/\Delta G^{\ddagger}$ taking values 0.25, 0.3, 0.35, 0.40, 0.45, 0.50, 0.55, 0.60, a list that includes temperatures high enough (or, equivalently, barriers low enough) to be outside the range of validity for pure Arrhenius-law behavior. Simulations were carried out in both the constant-force and steady-loading modes, with relative applied forces (F/F_B) and relative loading rates ($KV/k_0 F_T$) each spanning nearly 10 orders of magnitude. For each run, the trajectory leading to

barrier traversal was captured and analyzed.

The numerical simulations were carried out using a modified version [85] of the standard Verlet algorithm [86]. In each run, a critical time t_c, taken to be either the first-passage time of the particle over the barrier or the moment at which the barrier vanished, was recorded. For each energy potential profile and simulation mode, 3000 instantiations were generated.

In the constant-force mode, the rate $k(F)$ was computed from the mean escape time: $k(F) = 1/t_{\text{avg}}$, where $t_{\text{avg}} = (1/3000)\sum_{i=1}^{3000} t_c^{(i)}$. In the steady-loading mode, the linear correspondence $F_c = KVt_c$ gave rise to 3000 critical force values, on the basis of which further analyses were performed. First, the F_c values were sorted to identify their median value, which corresponds to the half-life force $\hat{F}$ (the force at which half of a population of independent particles would have escaped the well). Second, the F_c values were bootstrapped [101] to obtain the cumulative probability distribution $P(F_c) = \int_0^{F_c} dF\, p(F)$ and probability density $p(F_c) = P'(F_c)$. Finally the value of $k(F) = k(KVt)$, the instantaneous rate of barrier crossing at a particular bias strength, was obtained using the relation $k(F_c) = KVp(F_c)/(1 - P(F_c))$ [68].

The next step was to test the universality proposition by graphical means. We found strong evidence in its favor: the data collapse predicted by Eq. (4.1) is revealed in Fig. 4.2. In order to perform the conversion to reduced variables, each data point was associated with an individualized value of F_B and F_T. The former was obtained numerically, simply by solving for the applied force required to extinguish the barrier; the latter was estimated according to

$$\frac{1}{F_T} = \beta x^{\ddagger} + \frac{R_{1,2}^{\ddagger}}{2\kappa^{\dagger 2}} = \beta(x_b - x_l) + \frac{1}{2}\left(\frac{R_b}{\kappa_b^2} + \frac{R_l}{\kappa_l^2}\right). \tag{4.2}$$

The new symbols here refer to the curvature and skew at the bottom of the left well and at the top of the barrier: $\kappa_l = U''(x_l)$ and $\kappa_b = -U''(x_b)$; $R_l = -U'''(x_l)$ and $R_b = -U'''(x_b)$. A full rationale for Eq. (4.2) is given in Sec. 4.4.

Figure 4.2(a) presents a linear-log plot of $(F_T/F_B)Y(F) = (F_T/F_B)\log(k(F)/k_0)$ versus $f = F/F_B$. The data points for the steady-loading analysis are colored according to the simulation-

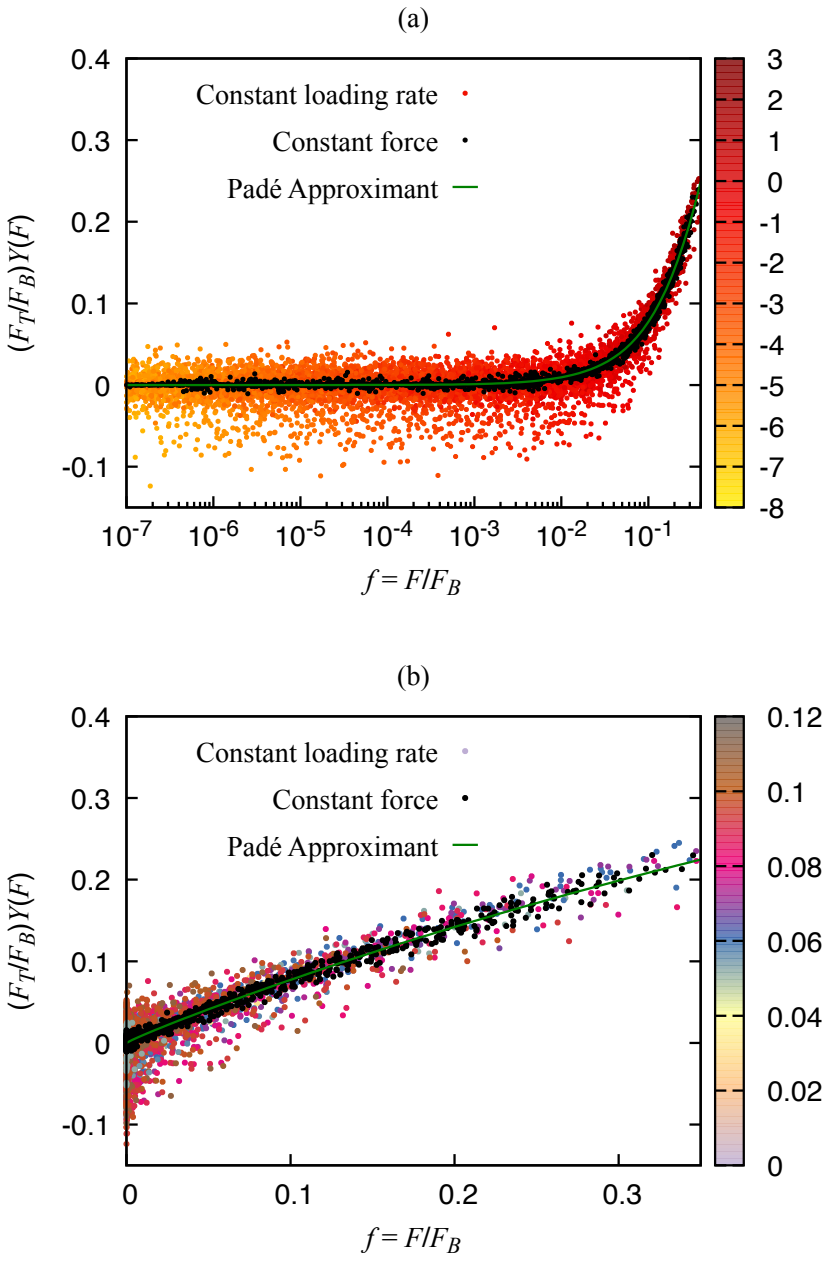

Figure 4.2. The upper and lower panels show plots of $(F_T/F_B)Y(F) = (F_T/F_B)\log(k(F)/k_0)$ versus $f = F/F_B$ and offer different views of the same underlying data set. Black circles correspond to simulations executed in the constant-force mode, and the green line is a low-order Padé approximant fit through these data points. Colored solid circles denote data from steady-loading runs. (a) The horizontal axis uses a log scale. Color intensity increases with the relative pulling rate, $r_T = KV/(k_0F_T)$. Numbers on the palette legend show the order of magnitude, $\log r_T$. (b) Both axes are linear. Colors now represent $F_T/F_B \approx 1/\beta\kappa^{\ddagger}x^{\ddagger 2} \approx \nu/2\beta\Delta G^{\ddagger}$, which characterizes the barrier regime.

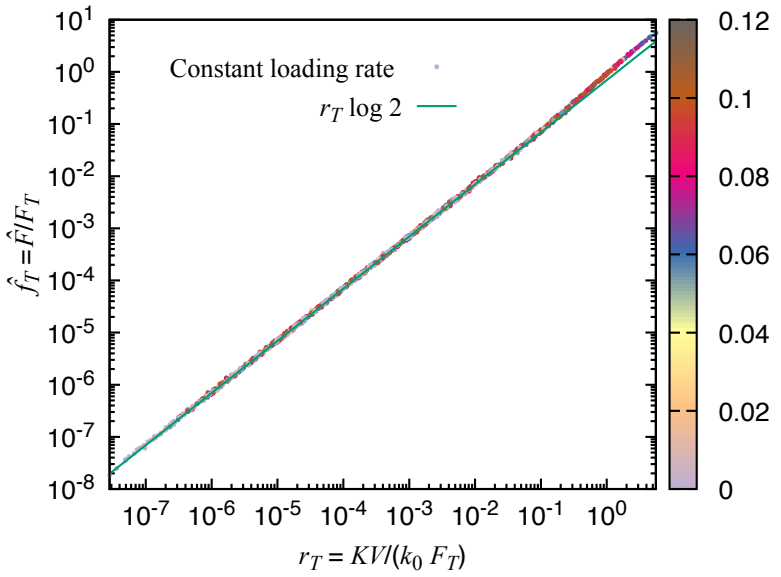

Figure 4.3. These data are from simulations performed with dynamic tilting of the potential at a constant loading rate. Shown here is $\hat{f}_T = \hat{F}/F_T$, the force at half-life measured with respect to the thermal force scale, plotted against the effective pulling rate, $r_T = KV/(k_0 F_T)$. Each data point is a solid circle, colored as per the legend according to its F_T/F_B value.

specific loading rate, and one can observe the smooth progression of data-point placement, weak loading to strong, tracing out the universal curve from left to right. The constant-force data (black circles) show considerably less scatter, but the two data sets are remarkably consistent. What makes this result so compelling is that the data collapse holds over a huge diversity of energy profiles and simulation conditions. We also remark that the steady-loading and constant-force approaches require quite different styles of simulation and analysis, but both yield the same underlying curve; Padé approximants fit to one or the other data set produce nearly identical functions.

Figure 4.2(b) shows the same data plotted on a linear scale. This view highlights the behavior at large forces, a regime in which the barrier is already substantially reduced at the time of barrier traversal. Here, the false color emphasizes the diversity in barrier height regimes, and we can see that data collapse holds over a wide range of ratios F_T/F_B.

Figure 4.3 presents a wholly different data collapse scheme, based only on simulations performed in the steady-loading mode. There, the reduced half-life force $\hat{f}_T = \hat{F}/F_T$ is plotted

versus the reduced loading rate $r_T = KV/(k_0 F_T)$. It is worth emphasizing again that the complete data set comes from simulations with seven different potential landscapes covering the full range of plausible ν values, $1/(\beta\Delta G^{\ddagger})$ ranging from 0.2 to 0.6, and loading rates running from $r_T = 10^{-8}$ to 100. Despite encompassing a large collection of different systems in distinct physical regimes, these data show an astonishing degree of collapse.

4.4 Theoretical motivation

In this section, we briefly review some of the theoretical considerations that originally led us to believe that scaling and data-collapse behavior are likely to manifest.

4.4.1 Locally quadratic approximation

We consider a one-dimensional, double-well energy landscape $U(x)$ with minima on the left and right, at positions x_l and x_r, separated by a barrier at x_b. A barrier of height $\Delta G^{\ddagger} = U(x_b) - U(x_l)$ impedes transitions from left to right. By definition $U'(x_l) = U'(x_b) = U'(x_r) = 0$. In the locally quadratic approximation, we assume

$$U(x) = \begin{cases} U(x_l) + \frac{1}{2}\kappa_l (x - x_l)^2 & \text{for } x \simeq x_l, \\ U(x_b) - \frac{1}{2}\kappa_b (x - x_b)^2 & \text{for } x \simeq x_b, \end{cases} \tag{4.3}$$

where $\kappa_l = U''(x_l)$ and $\kappa_b = -U''(x_b)$ are measures of the curvature at the bottom of the well and at the top of the barrier.

With the application of a bias force F, the extrema of the tilted landscape $\tilde{U}(x) = U(x) - Fx$ are found as follows:

$$0 = \tilde{U}'(x) = U'(x) - F = \begin{cases} +\kappa_l (x - x_l) - F, \\ -\kappa_b (x - x_b) - F. \end{cases} \tag{4.4}$$

At this level of approximation, the bias-induced shifts in the extrema are linear in F. In response to

the applied force ($F > 0$), the well basin moves to the right and the barrier peak moves to the left:

$$\tilde{x}_l = x_l + \frac{F}{\kappa_l},\ \tilde{x}_b = x_b - \frac{F}{\kappa_b}. \tag{4.5}$$

The two points eventually coalesce when $\tilde{x}_l = \tilde{x}_b$; i.e., when

$$x^\ddagger = x_b - x_l = \left(\frac{1}{\kappa_l} + \frac{1}{\kappa_b}\right) F \equiv \frac{F}{\kappa^\ddagger}. \tag{4.6}$$

The particular force value at which Eq. (4.6) holds is the barrier extinction force $\kappa^\ddagger x^\ddagger$. We follow the usual practice of decorating with a double-dagger superscript any quantity that is defined with respect to the barrier and the originating well. This includes the barrier distance $x^\ddagger = x_b - x_l$ and the effective curvature

$$\kappa^\ddagger = \left(\frac{1}{\kappa_b} + \frac{1}{\kappa_l}\right)^{-1} = \frac{\kappa_l \kappa_b}{\kappa_l + \kappa_b}. \tag{4.7}$$

In order to find an expression for the barrier height that is consistent with the approximation in Eq. (4.3), we must match the two piecewise quadratic curves. We do so at the point of common slope, where

$$U'(x^*) = \kappa_l (x^* - x_l) = -\kappa_b (x^* - x_b). \tag{4.8}$$

The reference position

$$x^* = \frac{\kappa_l x_l + \kappa_b x_b}{\kappa_l + \kappa_b}. \tag{4.9}$$

is a weighted average satisfying $x_l \leq x^* \leq x_b$. The height of the barrier in the untilted landscape ($F = 0$) is estimated to be

$$\begin{aligned} \Delta G^\ddagger &= U(x_b) - U(x^*) + U(x^*) - U(x_l) \\ &\approx \frac{1}{2}\kappa_b (x^* - x_b)^2 + \frac{1}{2}\kappa_l (x^* - x_l)^2 = \frac{1}{2}\kappa^\ddagger x^{\ddagger 2}. \end{aligned} \tag{4.10}$$

Formally, the barrier extinction force is given by the derivative of the barrier height with respect to

the barrier position. At the level of approximation of Eq. (4.10), we have

$$\frac{\partial \Delta G^{\ddagger}}{\partial x^{\ddagger}} = \kappa^{\ddagger} x^{\ddagger}. \tag{4.11}$$

4.4.2 Higher-order corrections

We can do better by including further contributions to the energy landscape expansion:

$$U(x) = \begin{cases} U(x_l) + \frac{1}{2!}\kappa_l (x - x_l)^2 - \frac{1}{3!} R_l (x - x_l)^3 + \frac{1}{4!} Q_l (x - x_l)^4 - \cdots, \\ U(x_b) - \frac{1}{2!}\kappa_b (x - x_b)^2 - \frac{1}{3!} R_b (x - x_b)^3 - \frac{1}{4!} Q_b (x - x_b)^4 - \cdots. \end{cases} \tag{4.12}$$

As in Eq. (4.3), the upper expression in Eq. (4.6) is for $x \simeq x_l$; the lower corresponds to $x \simeq x_b$. In addition to the two local curvatures, κ_l and κ_b, we have also defined measures of the skew [$R_l = -U'''(x_l) = -U^{(3)}(x_l)$ and $R_b = -U^{(3)}(x_b)$] and the kurtosis [$Q_l = U^{(4)}(x_l)$ and $Q_b = -U^{(4)}(x_b)$].

The positions of the shifted extrema are once again determined by $0 = U'(x) - F$. This demands that the expression

$$s\kappa_\alpha (x - x_\alpha) - \frac{1}{2} R_\alpha (x - x_\alpha)^2 + \frac{s}{6} Q_\alpha (x - x_\alpha)^3 + \cdots - F \tag{4.13}$$

vanish for both $\alpha = l$, $s = +1$ and $\alpha = b$, $s = -1$. Ensuring that it does so leads to

$$\tilde{x}_\alpha = x_\alpha + \frac{sF}{\kappa_\alpha} + \frac{sR_\alpha F^2}{2\kappa_\alpha^3} + \frac{s(3R_\alpha^2 - Q_\alpha \kappa_\alpha) F^3}{6\kappa_\alpha^5} + \cdots \tag{4.14}$$

and hence to an expression for $\tilde{x}_b - \tilde{x}_l$, the barrier distance in the tilted energy landscape:

$$x^{\ddagger} - \frac{F}{\kappa^{\ddagger}} - \frac{R^{\ddagger}_{1,3} F^2}{2{\kappa^{\ddagger}}^3} - \left(\frac{3\left(R^{\ddagger}_{2,5}\right)^2}{{\kappa^{\ddagger}}^5} - \frac{Q^{\ddagger}_{1,4}}{{\kappa^{\ddagger}}^4} \right) \frac{F^3}{6} + \cdots. \tag{4.15}$$

As a convenience, we have adopted the notation

$$A^{\ddagger}_{m,n} = \kappa^{\ddagger n}\left(\frac{A^m_l}{\kappa^n_l} + \frac{A^m_b}{\kappa^n_b}\right) = \frac{A^m_l \kappa^n_b + A^m_b \kappa^n_l}{(\kappa_l + \kappa_b)^n}. \tag{4.16}$$

If we then repeat the analysis used previously, we can produce expressions for the barrier height and barrier extinction force that are analogs of Eqs. (4.10) and (4.11):

$$\Delta G^{\ddagger} = \frac{1}{2!}\kappa^{\ddagger} x^{\ddagger 2} - \frac{1}{3!}R^{\ddagger}_{1,3} x^{\ddagger 3} + \frac{1}{4!}\left(\frac{3}{\kappa^{\ddagger}}\left[(R^{\ddagger}_{1,3})^2 - R^{\ddagger}_{2,5}\right] + Q^{\ddagger}_{1,4}\right)x^{\ddagger 4} + \cdots \tag{4.17}$$

and

$$\frac{\partial \Delta G^{\ddagger}}{\partial x^{\ddagger}} = \kappa^{\ddagger} x^{\ddagger} - \frac{1}{2}R^{\ddagger}_{1,3} x^{\ddagger 2} + \left(\frac{(R^{\ddagger}_{1,3})^2}{2\kappa^{\ddagger}} - \frac{R^{\ddagger}_{2,5}}{2\kappa^{\ddagger}} + \frac{1}{6}Q^{\ddagger}_{1,4}\right)x^{\ddagger 3} + \cdots \tag{4.18}$$

It is helpful to distinguish the barrier height expressions in Eqs. (4.10) and (4.17) by the labels $\Delta G^{\ddagger}_{\text{quad}}$ and $\Delta G^{\ddagger}$. Their ratio is simply the *shape parameter* defined by Dudko, Hummer, and Szabo [68]:

$$\begin{aligned} \nu = \frac{\Delta G^{\ddagger}}{\Delta G^{\ddagger}_{\text{quad}}} &= \frac{\frac{1}{2}\kappa^{\ddagger} x^{\ddagger 2} - \frac{1}{6}R^{\ddagger}_{1,3} x^{\ddagger 3} + \cdots}{\frac{1}{2}\kappa^{\ddagger} x^{\ddagger 2}} \\ &= 1 - \frac{R^{\ddagger}_{1,3} x^{\ddagger}}{3\kappa^{\ddagger}} + \left(\frac{(R^{\ddagger}_{1,3})^2}{4\kappa^{\ddagger 2}} - \frac{R^{\ddagger}_{2,5}}{4\kappa^{\ddagger 2}} + \frac{Q^{\ddagger}_{1,4}}{12\kappa^{\ddagger}}\right)x^{\ddagger 2} + \cdots \end{aligned} \tag{4.19}$$

That is to say, $1 - \nu$ encodes deviations from the behaviour of the purely quadratic model (in which $R_l = R_b = 0$, etc.). Insofar as Eq. (4.19) is a fast-converging power-series in $x^{\ddagger}$, with each subsequent term much smaller than the previous, it makes sense to view the subleading term on the right-hand-side of Eq. (4.19) as a proxy for those deviations:

$$\begin{aligned} \frac{R^{\ddagger}_{1,3} x^{\ddagger}}{3\kappa^{\ddagger}} &= \frac{(R_l \kappa^3_b + R_b \kappa^3_l)(x_b - x_l)}{3\kappa_l \kappa_b (\kappa_l + \kappa_b)^2} \\ &= 1 - \nu + \text{small corrections}. \end{aligned} \tag{4.20}$$

Hence, via Eq. (4.18), the extinction force can be approximated by its quadratic-model value

[Eq. (4.11)] up to rescaling by a shape-dependent factor:

$$\begin{aligned}\frac{\partial \Delta G^{\ddagger}}{\partial x^{\ddagger}} &= \kappa^{\ddagger} x^{\ddagger} - \kappa^{\ddagger} x^{\ddagger} \frac{R^{\ddagger}_{1,3} x^{\ddagger}}{2\kappa^{\ddagger}} + \cdots \\ &= \kappa^{\ddagger} x^{\ddagger} \Big[1 - \frac{3}{2}(1-\nu)\Big] + \cdots \approx \kappa^{\ddagger} x^{\ddagger} \left(\frac{3\nu - 1}{2}\right).\end{aligned} \tag{4.21}$$

Typical values for smooth energy profiles ($2/3 \lesssim \nu \lesssim 6/5$) suggest $0.5 \lesssim (3\nu - 1)/2 \lesssim 1.3$, so we expect the true extinction force value to be never more than a factor of two away from $\kappa^{\ddagger} x^{\ddagger}$. Of course, when $U(x)$ is known, it is straightforward to compute the extinction force numerically.

4.4.3 Universality of the biased escape rate

The calculations in this section are meant merely as a motivation for the two-force-scale arguments we make in the paper. We assume Langevin behaviour with moderate to strong friction and ignore the complications of non-Markovian dynamics. Following Kramers, the escape rate from the left well of the untilted energy landscape is

$$\begin{aligned}k_0 &\propto \frac{1}{\sqrt{\kappa_l \kappa_b}} \exp\big(-\beta \Delta G^{\ddagger}\big) \\ &= \frac{1}{\sqrt{-U''(x_l) U''(x_b)}} \exp\big(-\beta [U(x_b) - U(x_l)]\big).\end{aligned} \tag{4.22}$$

The corresponding expression for the tilted case can be produced by substituting $U(x_\alpha) \to \tilde{U}(\tilde{x}_\alpha)$. If we expand around the $F = 0$ case and collect terms order by order within the argument of the exponential, we arrive at

$$\begin{aligned}k(F) = k_0 \exp\Bigg[& F\left(\beta x^{\ddagger} + \frac{R^{\ddagger}_{1,2}}{2\kappa^{\ddagger 2}}\right) \\ & - F^2 \left(\frac{\beta}{2\kappa^{\ddagger}} - \frac{R^{\ddagger}_{2,4}}{2\kappa^{\ddagger 4}} + \frac{Q^{\ddagger}_{1,3}}{4\kappa^{\ddagger 3}}\right) \\ & - F^3 \left(\frac{\beta R^{\ddagger}_{1,3}}{6\kappa^{\ddagger 3}} - \frac{2R^{\ddagger}_{3,6}}{3\kappa^{\ddagger 6}} + \cdots\right) + O(F^4)\Bigg].\end{aligned} \tag{4.23}$$

We expect the largest terms to be those proportional to β, which come from the exponential in Eq. (4.22); the contributions originating under the radical in the prefactor are smaller.

An important insight is that the logarithmic relative rate can be written in the form

$$Y(F) = \log \frac{k(F)}{k_0} = \frac{F}{F_T} - \frac{F^2}{2F_T F_B} - \frac{CF^3}{2F_T F_B^2} + \cdots \tag{4.24}$$

In this expression we have introduced two new dimensionful coefficients (with units of force), defined according to

$$\begin{aligned}
\frac{1}{F_T} &= \beta x^\ddagger + \frac{R^\ddagger_{1,2}}{2\kappa^{\dagger 2}} \\
&= \beta x^\ddagger \left\{ 1 + \underbrace{\frac{R^\ddagger_{1,2}}{2\beta\kappa^{\dagger 2} x^\ddagger}}_{\lambda_T} \right\} \equiv \frac{1+\lambda_T}{F_T^{(0)}}, \\
\frac{1}{F_T F_B} &= \frac{\beta}{\kappa^\ddagger} - \frac{R^\ddagger_{2,4}}{\kappa^{\ddagger 4}} + \frac{Q^\ddagger_{1,3}}{2\kappa^{\ddagger 3}} \\
&= \frac{\beta x^\ddagger}{\kappa^\ddagger x^\ddagger} \left\{ 1 - \underbrace{\frac{1}{\beta}\left(\frac{R^\ddagger_{2,4}}{\kappa^{\ddagger 3}} - \frac{Q^\ddagger_{1,3}}{2\kappa^{\ddagger 2}} \right)}_{\lambda_{TB}} \right\} \equiv \frac{1-\lambda_{TB}}{F_T^{(0)} F_B^{(0)}},
\end{aligned} \tag{4.25}$$

along with a dimensionless constant C. Matching the $O(F^3)$ terms in Eqs. (4.23) and (4.24) and invoking Eq. (4.20), we identify $C = 1 - \nu + \cdots$, with the elision hiding additional terms that are shape- and temperature-dependent but small; specifically,

$$C = \frac{R^\ddagger_{1,3} x^\ddagger}{3\kappa^\ddagger} \frac{(1+\lambda_T)}{(1-\lambda_{TB})^2} \left(1 - \frac{4R^\dagger_{3,6}}{3\beta R^\ddagger_{1,3} \kappa^{\ddagger 3}} + \cdots \right). \tag{4.26}$$

The advantage of the rewriting in Eq. (4.24) is that we have picked out two force scales, F_T and F_B, whose magnitude is determined—up to modest renormalization by λ_T and λ_{TB}—by $F_T^{(0)} = 1/\beta x^\ddagger$ and $F_B^{(0)} = \kappa^\ddagger x^\ddagger$. Equation (4.25) implies

$$F_T = F_T^{(0)} \left(\frac{1}{1+\lambda_T} \right), \; F_B = F_B^{(0)} \left(\frac{1+\lambda_T}{1-\lambda_{TB}} \right). \tag{4.27}$$

To give a more physical picture, we interpret F_T as the typical thermal force that provides the kick out of the well and F_B as the applied force required to fully extinguish the barrier: The ratio of the two force scales is

$$\frac{F_B}{F_T} = \beta\kappa^{\ddagger}x^{\ddagger 2}\frac{(1+\lambda_T)^2}{(1-\lambda_{TB})} = \frac{2\beta\Delta G^{\ddagger}}{\nu}(1+\cdots). \tag{4.28}$$

A key observation is that if we view the escape rate as a function of a reduced applied force $f = F/F_B$, measured in units of the barrier extinction force scale, then Eq. (4.24) transforms to

$$\begin{aligned} Y(F) \xrightarrow{F\to F_B f} & \frac{F_B f}{F_T} - \frac{(F_B f)^2}{2F_T F_B} - \frac{C(F_B f)^3}{2F_T F_B^2} + \cdots \\ &= \frac{F_B}{F_T}\left(f - \frac{1}{2}f^2 - \frac{1}{2}Cf^3 + \cdots\right). \end{aligned} \tag{4.29}$$

Note that the terms at order f and f^2 are wholly independent of the details of the system. $(C/2)f^3$ is the leading nonuniversal term, but even there [as per Eq. (4.26)] the shape dependence is quite weak and the temperature dependence almost negligible. This means that truly idiosyncratic contributions do not show up until order f^4, and those we expect to be heavily suppressed just by power reduction; in practice, $f = F/F_B < 1$, since escape almost always precedes complete elimination of the barrier.

Moreover, since physical considerations demand that the escape rate increase with F, it is legitimate to apply a series acceleration transformation by which Eq. (4.29) is expanded in terms of some function of f that is monotonically increasing but slower-growing than the monomial f itself; one might consider $f/(1+f/2)$ (as in Ref. 84) or $\log(1+f)$, say. Then $f-(1/2)f^2-(C/2)f^3+\cdots$ can be recast as

$$\frac{f}{1+f/2} - \left(\frac{C}{2}+\frac{1}{4}\right)\left(\frac{f}{1+f/2}\right)^3 + \cdots \tag{4.30}$$

or

$$\log(1+f) - \left(\frac{C}{2}+\frac{1}{3}\right)\left[\log(1+f)\right]^3 + \cdots . \tag{4.31}$$

Since we expect $-1/5 \lesssim C \lesssim 1/3$ (and often $|C| \ll 1$), Eqs. (4.31) and (4.30) are close to being universal even up to order three. This leads us to posit that the logarithmic relative escape

rate has a form reminiscent of the finite-size scaling ansatz of a critical state:

$$\begin{aligned} Y(F) = \log \frac{k(F)}{k_0} &= \left(\frac{F_T}{F_B}\right)^{-1} \mathbb{Y}(F/F_B, F_T/F_B) \\ &= \left(\frac{F_T}{F_B}\right)^{-1} \left[\mathbb{Y}(F/F_B, 0) + \left(\frac{F_T}{F_B}\right)^{\omega} \mathbb{W}(F/F_B) + \cdots\right]. \end{aligned} \tag{4.32}$$

Here, $\omega > 0$ is the exponent for the subleading corrections to scaling. Since $F_T/F_B \approx 1/(\beta\kappa^{\ddagger}x^{\ddagger 2}) \approx \nu/(2\beta\Delta G^{\ddagger}) \ll 1$, the quantity $(F_T/F_B)Y(F)$ should collapse onto a universal curve when plotted against $f = F/F_B$:

$$\frac{F_T}{F_B} Y(F) = \frac{F_T}{F_B} \log \frac{k(F)}{k_0} \approx \mathbb{Y}(f, 0). \tag{4.33}$$

Other combinations of $(F_T/F_B)Y(F)$ may bring about an even cleaner coincidence. For example,

$$\begin{aligned} \log(1+f) &= \frac{F_T}{F_B} Y(F) + \left(\frac{C}{2} + \frac{1}{3}\right) \left[\log(1+f)\right]^3 + \cdots \\ &= \frac{F_T}{F_B} Y(F) \left\{1 + \left(\frac{C}{2} + \frac{1}{3}\right) \left[\frac{F_T}{F_B} Y(F)\right]^2\right\} + \cdots . \end{aligned} \tag{4.34}$$

Imagine that there is a set of escape rate measurements but the underlying $U(x)$ is unknown. Even without knowledge of a fitting form such as Eqs. (4.33) and Eq. (4.34), graphical collapse onto a common curve can be engineered by careful adjustment of the free parameters F_T and F_B.

4.4.4 Data collapse of the rupture force

A population $n(t)$ of systems prepared in a well and subject to an escape rate $k(F)$ is subject to the rate equation $\dot{n} = -kn$. If the pulling force increases linearly in time, with a constant loading rate KV, then

$$\frac{dn}{dt} = -k(F)n(t) = -k(KVt)n(t). \tag{4.35}$$

The time $\hat{t}$ for half the population to escape is given by

$$\log 2 = \int_1^{1/2} \frac{dn}{n} = -\int_0^{\hat{t}} dt\, k(KVt). \tag{4.36}$$

In the Bell-Evans picture [58, 67], which supposes that the biased rate is simply $k(F) = k_0 \exp\left(\beta F x^{\ddagger}\right)$, Eq. (4.36) becomes

$$\log 2 = \frac{k_0}{\beta KV x^{\ddagger}}\left(e^{\beta KV \hat{t} x^{\ddagger}} - 1\right) = \frac{F_T^{(0)} k_0}{KV}\left(e^{\beta \hat{F} x^{\ddagger}} - 1\right). \tag{4.37}$$

Then $\hat{F}$, the force at half-life, is

$$\hat{F} = F_T^{(0)} \log\left(1 + \frac{KV \log 2}{F_T^{(0)} k_0}\right). \tag{4.38}$$

On the other hand, if the escape rate is represented using the universal part of Eq. (4.31), via $\log[k(F)/k_0] = (F_B/F_T)(f - f^2/2 + \cdots) = (F_B/F_T)\log(1+f)$, then

$$\begin{aligned} k(F) &= k_0 \exp\left[\frac{F_B}{F_T}\log(1+f)\right] = k_0\left(1 + \frac{F}{F_B}\right)^{\frac{F_B}{F_T}} \\ &= k_0\left(1 + \frac{F}{\kappa^{\ddagger} x^{\ddagger}}\right)^{\beta \kappa^{\ddagger} x^{\ddagger 2} + \cdots} \\ &= k_0\left[\left(1 + \frac{F}{\kappa^{\ddagger} x^{\ddagger}}\right)^{\kappa^{\ddagger} x^{\ddagger}}\right]^{\beta x^{\ddagger} + \cdots}. \end{aligned} \tag{4.39}$$

The omitted terms [denoted by $\cdots$ in the exponent of the last line of Eq. (4.39)] are ones that become negligible at low temperature and large barrier height; in that same limit, we can formally take $\kappa^{\ddagger} x^{\ddagger} \to \infty$, which allows us to recover the Bell-Evans expression, $k(F) \to k_0 \exp\left(\beta F x^{\ddagger}\right)$.

We need not resort to such a limit, however, since the half-life can be solved analytically:

$$\begin{aligned}\log 2 &= \int_0^{\hat{t}} dt\, k(F(t)) = \int_0^{\hat{t}} dt\, k(KVt) \\ &= \int_0^{\hat{t}} dt\, k_0 \Big(1 + \frac{KVt}{F_B}\Big)^{\frac{F_B}{F_T}} \\ &= k_0 F_B \Big(\frac{-1 + (1 + KV\hat{t}/F_B)^{1+F_B/F_T}}{(1 + F_B/F_T)KV}\Big).\end{aligned} \tag{4.40}$$

This corresponds to an average rupture force

$$\begin{aligned}\hat{F} = KV\hat{t} &= F_B \Big\{ \Big[1 + \Big(1 + \frac{F_B}{F_T}\Big)\frac{KV\log 2}{k_0 F_B}\Big]^{\frac{F_T}{F_T+F_B}} - 1 \Big\} \\ &= \frac{(\log 2)KV}{k_0} - \frac{(\log 2)^2 (KV)^2}{2F_T k_0^2} + \frac{(2F_B + F_T)(\log 2)^3 (KV)^3}{6F_B F_T^2 k_0^3} + \cdots .\end{aligned} \tag{4.41}$$

A useful resummation is

$$\hat{F} = F_T \log\Big[1 + \frac{KV\log 2}{F_T k_0}\Big] + \frac{2F_B - F_T}{6}\Big(\log\Big[1 + \frac{KV\log 2}{F_T k_0}\Big]\Big)^3 + \cdots , \tag{4.42}$$

the first term of which is identical to the right-hand-side of Eq. (4.38), up to the renormalization $F_T^{(0)} \to F_T$.

In order to put Eq. (4.42) into a scale-invariant form, we define the half-life pulling force with respect to the thermal force scale, $\hat{f}_T = \hat{F}/F_T$, and a dimensionless loading rate, $r_T = KV/(F_T k_0)$. This leads to

$$\begin{aligned}\hat{f}_T &= \log\big(1 + r_T \log 2\big) + \frac{(2F_B/F_T - 1)}{6}\big[\log\big(1 + r_T\log 2\big)\big]^3 \\ &\approx \log\big(1 + r_T \log 2\big) + \frac{(2F_B/F_T - 1)}{6}\hat{f}_T^3.\end{aligned} \tag{4.43}$$

In general, $F_B/F_T \sim 2\beta\Delta G^\ddagger/\nu$ is not small. But so long as $(F_B/F_T)\hat{f}_T^2 = F_B F^2/F_T^3 \ll 1$, it is appropriate to write

$$\hat{f}_T\Big(1 - \frac{(2F_B/F_T - 1)}{6}\hat{f}_T^2\Big) = \log\big(1 + r_T\log 2\big). \tag{4.44}$$

4.5 Conclusion

We have argued for universality in the biased activated-barrier-crossing problem and presented strong numerical evidence in favor of the existence of some underlying scaling function for $Y(F) = \log[k(F)/k_0]$. Our simulated data show collapse onto a single curve when recast into suitably reduced coordinates. This is true for data generated in simulations operating over a wide range of bath temperatures, applied forces, and loading rates and over a family of potential landscapes with different underlying barrier shapes.

These observations suggest the utility of data collapse as a practical tool for analysis. While the original motivation for this work was the mechanical unfolding of biopolymers, the universality we have identified is widely relevant. It applies to situations across many branches of science, wherever the energy landscape picture is germane and the experimental setup involves barrier traversal assisted by active pulling. Our recommendation is that measurements of well-escape statistics be transformed to identify best values of the intrinsic force scales (from which can be inferred some combination of $x^\ddagger$, $\kappa^\ddagger$, $\Delta G^\ddagger$, and ν). F_T and F_B are to be treated as free parameters and tuned until data collapse is achieved and the universal curve emerges.

CHAPTER 5

ESCAPE RATE ANALYSIS IN TWO DIMENSIONS

5.1 Introduction

In pulling experiments, approximations based on a 1D energy profile have generally been successful for small proteins [54, 102], although there exist counterexamples in which multiple dimensions are required to account for the observed behavior—for example, proteins with knots [103] or multiple pathways [104]. We understand that using end-to-end length as a single reaction coordinate cannot offer a full description, as we might encounter multiple conformations that are degenerate in the extension variable, as shown in the left panel of Fig. 1.8. Consequently, the projection of the multidimensional landscape onto a single reaction coordinate is suboptimal in some situations and may prevent us from capturing the full dynamics of the folding/unfolding process. This may lead to poor predictions and incorrect interpretations of experimental measurements [53, 105, 106].

The least disruptive approach is to hold to the 1D analysis but to perform additional statistical analysis to distinguish various states whose signature might be convolved together in the 1D projection [107]. Instead, the approach we pursue is to allow for one additional coordinate, largely complementary to the extension, that can lift the degeneracy (see the right panel of Fig. 1.8). Our goal is to minimize the number of reaction coordinates and yet to address the underlying problems that plague the 1D analysis.

Our tests were performed on an abstract 2D landscape $U(x, y)$ having two minima separated by a saddle barrier. We applied a time-dependent pulling force $F = KVt$ with constant loading rate (rather than a constant pulling force as in Ref. 108); the force was applied allowing for a rotation by angle θ with respect to the primary reaction coordinate, x. The rotation of the potential accounts for

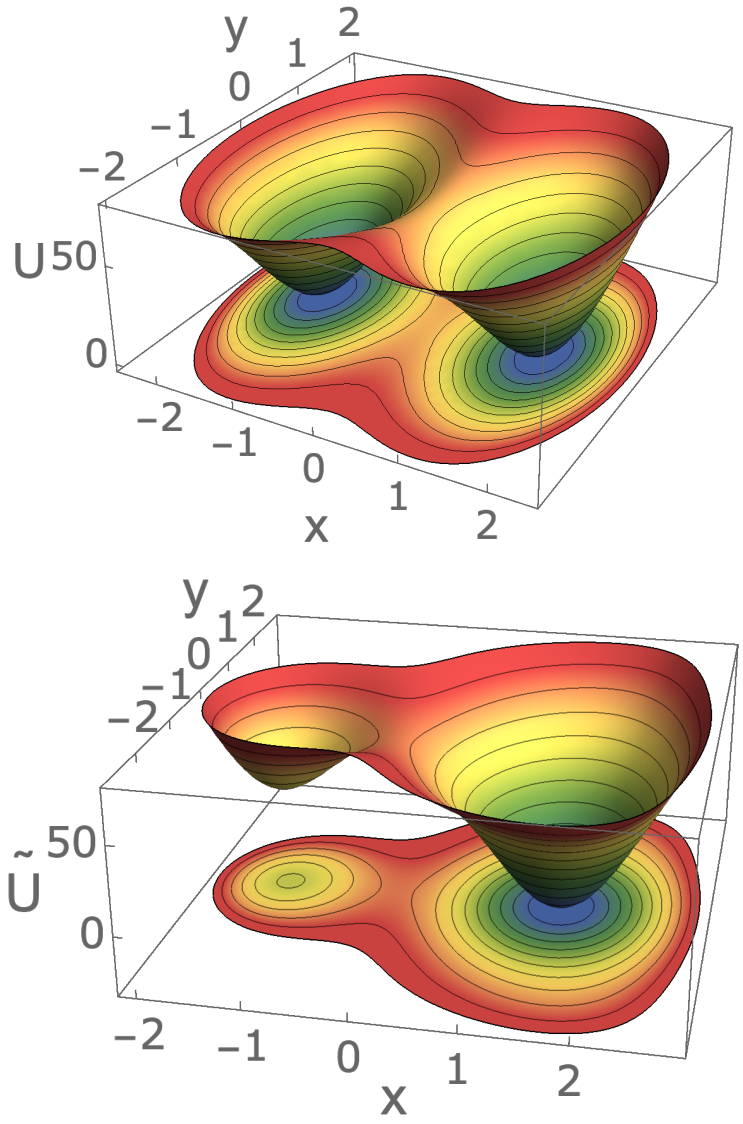

Figure 5.1. Top, 2D double well system at positions (x_l, y_l) and (x_r, y_r) separated by a barrier at (x_b, y_b) $(x_l < x_b < x_r)$. Bottom, tilted landscape after application of rotating pulling force F. Positions of well and barrier get both translational and rotational shift.

the possibility that efficient pulling might not always be directed exactly along the primary reaction coordinate or that the folded and unfolded wells might not always be perfectly aligned along the primary reaction coordinate. We derived our 2D rate equation,

$$k(F) = k_0 \exp\left(\frac{\beta F r^{\ddagger}}{1 + F/2\kappa^{\ddagger} r^{\ddagger}}\right), \tag{5.1}$$

as a generalization of the 1D work [84] that appears in Ch. 3. This is in contrast with the corresponding 2D Bell-Evans form,

$$k_{\mathrm{BE}}(F) = k_0 e^{\beta F r^{\ddagger}}. \tag{5.2}$$

We tested the reliability of Eqs. (5.1) and (5.2) against numerical simulations. The results suggest that Eq. (5.1) is much more reliable than Eq. (5.2), especially at high pulling rates. The match to the probability distribution of the critical force was superior for Eq. (5.1).

As a further check, we projected the 2D landscape onto 1D landscape and tested the agreement between the fully 2D simulation and the 1D simulation of the 2D profile projected onto 1D. After a careful investigation, we concluded that the downward projection of 2D landscape onto 1D landscape is not always easy and reliable. This was highlighted by the disagreement between the 1D and 2D simulations when a rotated 2D landscape was projected onto its corresponding 1D landscape. This meant projection of multidimensional landscape onto 1D landscape might not always produce the desirable result, which corroborates our initial concerns that the 1D analysis can be inadequate. This might be due to the presence of multiple transition trajectories in 2D landscape while going from the unfolded to the folded state unless there is a narrow channel present in between them. The 1D landscape had only one possible trajectory for a transition from folded to unfolded state as shown in Fig. 1.7 unlike 2D landscape which has multiple possible unfolded trajectories.

5.2 Formal Development

We considered a two dimensional potential landscape $U(x, y)$ where, x and y represent the primary and secondary reaction coordinates. We applied the pulling force at an angle θ to the primary reaction coordinate, as shown in Fig. 5.1, such that a term $-F(x\cos\theta + y\sin\theta)$ was induced in the free energy. The pulling force had the form $F = KVt$, which grew linearly in time with constant loading rate KV. The molecule moved in the combined 2D free energy landscape given by

$$\tilde{U}(x, y) = U(x, y) - KVt(x\cos\theta + y\sin\theta). \tag{5.3}$$

If we consider $U(x, y)$ to be a double-well potential with wells at positions (x_l, y_l) and (x_r, y_r) separated by a saddle barrier at (x_b, y_b) with $(x_l < x_b < x_r)$, the well escape rate from left to right during pulling goes as $k(F) \sim \exp\left(-\beta\Delta\tilde{U}\right)$, where $\Delta\tilde{U} = \tilde{U}(x_b, y_b) - \tilde{U}(x_l, y_l)$. Assuming small perturbation around the well positions (x_l, y_l) and (x_b, y_b), the rate equation is

$$k(F) \sim \exp\left[-\beta(\tilde{U}(x_b + \delta x_b, y_b + \delta y_b) - \tilde{U}(x_l + \delta x_l, y_l + \delta y_l))\right]. \tag{5.4}$$

From Eq. (5.3) we get,

$$\begin{aligned}
\tilde{U}(x_b + \delta x_b, y_b + \delta y_b) &= U(x_b + \delta x_b, y_b + \delta y_b) \\
&\quad - F[(x_b + \delta x_b)\cos\theta + (y_b + \delta y_b)\sin\theta] \\
\tilde{U}(x_l + \delta x_l, y_l + \delta y_l) &= U(x_l + \delta x_l, y_l + \delta y_l) \\
&\quad - F[(x_l + \delta x_l)\cos\theta + (y_l + \delta y_l)\sin\theta]
\end{aligned} \tag{5.5}$$

Performing Taylor expansions of $\tilde{U}_x(x, y)$ and $\tilde{U}_y(x, y)$ around (x_l, y_l) and (x_b, y_b) up to first

order in δx_l, δy_l, δx_b and δy_b gives

$$\begin{aligned}
\delta x_l &= F(V^L_{yy}\cos\theta - V^L_{xy}\sin\theta)/V^L_1,\\
\delta y_l &= F/V^L_1(V^L_{xx}\sin\theta - V^L_{xy}\cos\theta)/V^L_1,\\
\delta x_b &= F/V^b_1(V^b_{yy}\cos\theta - V^b_{xy}\sin\theta)/V^b_1,\\
\delta y_b &= F/V^b_1(V^b_{xx}\sin\theta - V^b_{xy}\cos\theta)/V^b_1.
\end{aligned} \tag{5.6}$$

where

$$\begin{aligned}
V^L_{xx} &= \frac{\partial^2 U(x_l,y_l)}{\partial x^2}, \quad V^L_{yy} = \frac{\partial^2 U(x_l,y_l)}{\partial y^2}, \quad V^L_{xy} = \frac{\partial^2 U(x_l,y_l)}{\partial x\partial y},\\
V^b_{xx} &= \frac{\partial^2 U(x_b,y_b)}{\partial x^2}, \quad V^b_{yy} = \frac{\partial^2 U(x_b,y_b)}{\partial y^2}, \quad V^b_{xy} = \frac{\partial^2 U(x_b,y_b)}{\partial x\partial y},\\
V^L_1 &= V^L_{xx}V^L_{yy} - (V^L_{xy})^2, \quad V^b_1 = V^b_{xx}V^b_{yy} - (V^b_{xy})^2.
\end{aligned} \tag{5.7}$$

Furthermore, expanding terms $U(x_b+\delta x_b, y_b+\delta y_b)$ and $U(x_l+\delta x_l, y_l+\delta y_l)$ in Eq. (5.5) around points (x_b, y_b) and (x_l, y_l), respectively, simplifying using the values of δx_b, δy_b, δx_l and δy_l, collecting terms up to second order in F, and finally plugging in the values of $\tilde{U}(x_b+\delta x_b, y_b+\delta y_b)$ and $\tilde{U}(x_l+\delta x_l, y_l+\delta y_l)$ in Eq. (5.4), we get the rate equation of the form

$$k(F) = k_0 \exp\left[\beta F r^{\ddagger}\left(1 - \frac{F}{2\kappa^{\ddagger} r^{\ddagger}}\right)\right]. \tag{5.8}$$

Here, $x^{\ddagger} = x_b - x_l$, $y^{\ddagger} = y_b - y_l$, $r^{\ddagger} = x^{\ddagger}\cos\theta + y^{\ddagger}\sin\theta$ and

$$\kappa^{\ddagger} = \frac{V^L_1 V^b_1}{V^b_1 V^L - V^L_1 V^b} \tag{5.9}$$

with

$$\begin{aligned}
V^L &= (V^L_{yy}\cos^2\theta + V^L_{xx}\sin^2\theta - 2V^L_{xy}\sin\theta\cos\theta),\\
V^b &= (V^b_{yy}\cos^2\theta + V^b_{xx}\sin^2\theta - 2V^b_{xy}\sin\theta\cos\theta).
\end{aligned} \tag{5.10}$$

As before, we make use of the idea of infinite resummation, $1 - \epsilon + \epsilon^2 - \cdots \approx 1/(1+\epsilon)$, which transforms Eq. (5.8) into Eq. (5.1), up to discrepancies at $O(F^3)$. The transformed expression is well-behaved everywhere and displays no obviously unphysical behavior.

In the usual adiabatic limit, the expression for the cumulative probability distribution of the rupture force is given by Eq. (3.5). Using Eq. (5.2) in Eq. (3.5) we obtained the closed form expression for Bell-Evans cumulative probability distribution,

$$P_{\mathrm{BE}}(F_c) = 1 - \exp\left[\frac{k_0}{KV\beta r^{\ddagger}}\left(1 - e^{\beta F_c r^{\ddagger}}\right)\right]. \tag{5.11}$$

Putting Eq. (5.1) into Eq. (3.5), we obtained our form of cumulative probability distribution, given by Eq. (5.12). If instead we put Eq. (5.1) into Eq. (3.5), we get a more complicated result:

$$P(F_c) = 1 - \exp\left[\frac{k_0}{KV}\left(F_1 + F_2 - 2r^{\ddagger}\kappa^{\ddagger}\right)\right]. \tag{5.12}$$

The quantities F_1 and F_2 have units of force and are explicit functions of the critical value F_c:

$$\begin{aligned} F_1 &= \left(F_c + 2r^{\ddagger}\kappa^{\ddagger}\right)\exp\left(\frac{2F_c r^{\ddagger 2}\beta\kappa^{\ddagger}}{F_c + 2r^{\ddagger}\kappa^{\ddagger}}\right), \\ F_2 &= 4r^{\ddagger 3}\beta\kappa^{\ddagger 2}\exp\left(2r^{\ddagger 2}\beta\kappa^{\ddagger}\right)\left[\mathrm{Ei}\left(-\frac{4r^{\ddagger 3}\beta\kappa^{\ddagger 2}}{F_c + 2r^{\ddagger}\kappa^{\ddagger}}\right) - \mathrm{Ei}\left(-2r^{\ddagger 2}\beta\kappa^{\ddagger}\right)\right]. \end{aligned} \tag{5.13}$$

This outlines our 2D work. We obtained modified expressions for rate and cumulative probability distribution as given by equations Eq. (5.1) and Eq. (5.12), respectively. The reliability of these equations were tested against data obtained from numerical simulation.

Next, we focussed on dimension reduction of the potential landscape using an art of projection. As discussed earlier, the projection of multidimensional landscape to the lower dimension landscape would always make the analysis simpler and easier. However, it is also useful to check if there is any loss in information or if the lower dimension analysis is optimal. From 2D landscape, we could generate an effective 1D landscape with a single reaction coordinate by using an art of projection, a mathematical trick shown in the Eq. (5.14). In our particular example, the

integration did not produce closed form expression and we had to use the numerical integration and interpolation technique called spline to generate the 1D landscape.

$$
\begin{aligned}
e^{-\beta U_{\text{eff}}(x)} &= \int_{-\infty}^{\infty} dy\, e^{-\beta U(x,y)} \\
U_{\text{eff}}(x) &= -\frac{1}{\beta} \log \int_{-\infty}^{\infty} dy\, e^{-\beta U(x,y)}
\end{aligned}
\tag{5.14}
$$

The 1D landscape produced from 2D landscape and 2D landscape are represented side by side in Fig. 5.2.

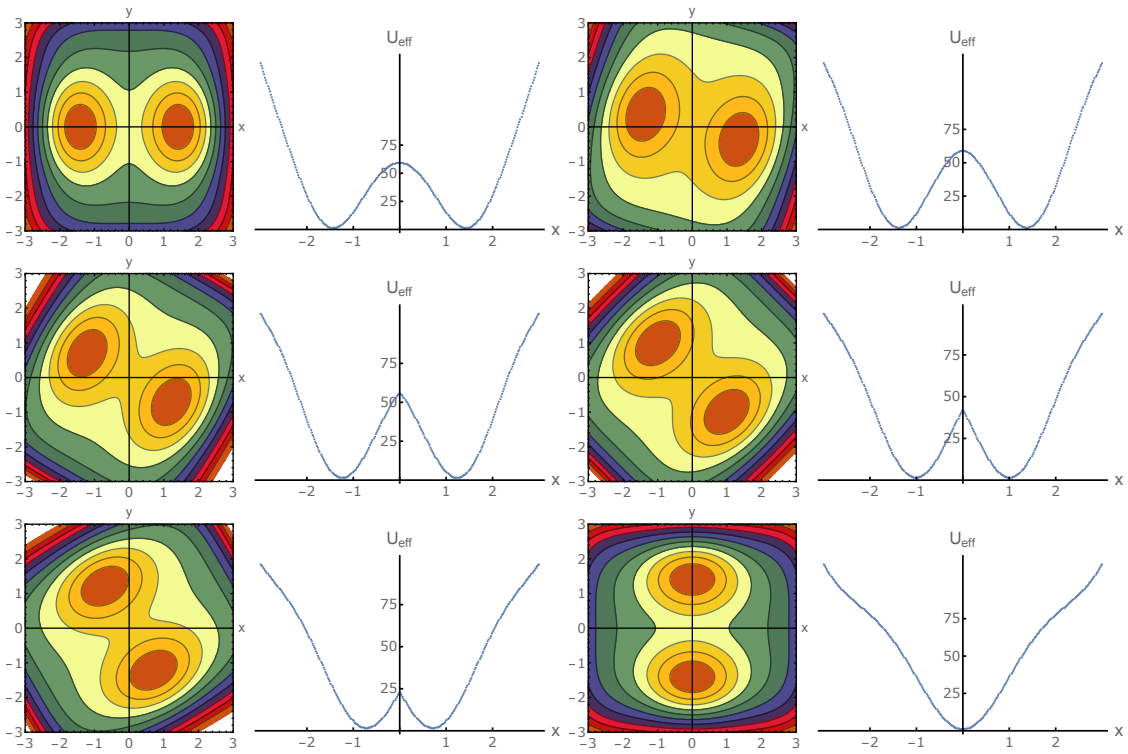

Figure 5.2. The 1D counterparts, figures in columns second and fourth, of 2D landscapes, figures in first and third column respectively, obtained after projection onto single reaction coordinate end-to-end length, x. In 1D Model, two distinct wells slowly get collapsed onto a single well once the potential landscape is rotated by $\pi/2$.

5.3 Numerical Simulations

The analytic work above was tested with the numerical simulation. To mimic the experimental scenario, we considered the motion of a biopolymer molecule defined by 2D Langevin

Equation, Eq. (2.2) which can be broken into two independent equations as in Eq. (2.3) and can be used to address the motion of molecule along two independent directions x and y.

This was implemented numerically by using a modified modern formulation [85] of Verlet algorithm [86], as in 1D analysis. We mimicked the experimental work by assuming the stochastic motion of the molecule of the effective mass $m_x = 2\,\text{pg}$ and $m_y = 2\,\text{pg}$ over a two-dimensional (2D) bi-quadratic potential $U_0(x, y) = x^4 + 5(y/3)^4 - 80\exp\left(-(x-1.5)^2 - 5(y/3)^2\right) - 80\exp\left(-(x+1.5)^2 - 5(y/3)^2\right) + 5\exp\left(2(y/3)^2\right) + 70.45$. The molecule was assumed to be pulled from two ends by a laser potential with force constant K and the constant pulling velocity V with the force $F = KVt$ that increases linearly with time. The chain was assumed to be pulled along positive x-axis (primary reaction coordinate). The saddle energy barrier was considered to be at $(0, 0)$ with height $\Delta G^{\ddagger} = 58.58\,\text{pN}\cdot\text{nm}$. The bottom positions of left and right well were taken at $(-1.43, 0)$ and $(1.43, 0)$ respectively. The stochastic forces on the molecule along x and y direction given by $\xi_x(t)$ and $\xi_y(t)$ respectively, were drawn randomly from the Gaussian Distribution of width $(2m_x\gamma_x k_B T\delta t)^{1/2}$ and $(2m_y\gamma_y k_B T\delta t)^{1/2}$ respectively with $k_B T = 4.1\,\text{pN}\cdot\text{nm}$, $\gamma_x = 20\,\mu\text{s}^{-1}$, $\gamma_y = 20\,\mu\text{s}^{-1}$ and δt ranging from $10^{-1}\,\mu\text{s}$ to $10^{-5}\,\mu\text{s}$ from low to high pulling rates. The act of applying rotating pulling force on 2D potential or rotating the potential and applying the pulling force along x-direction theoretically would have been the same thing. However, practically the latter would make more sense. Hence, we used the latter technique for the numerical simulation.

The simulation was initialized in left well by drawing initial values of velocity (v_x, v_y) from the distributions $(e^{-\beta m v_x^2/2}, e^{-\beta m v_y^2/2})$ so that the each simulation began fully thermalized. For each pulling rate KV, the simulation flagged the value of pulling force at which the particle crossed the barrier or barrier vanished; we took this to be the value of rupture or critical force F_c. The determination of transition region, i.e, the point of time where barrier vanished or particle crossed the barrier was not straightforward. We had to come up with a mini algorithm described in Chap. 2. For each value of KV the simulation was carried out 4000 times, each run generating a unique value of the rupture force. The cumulative probability distribution $P(F_c)$ was constructed in the standard way—by sorting the measured rupture forces in ascending order and then pairing them

with a uniform grid of values running from 0 to 1. The plot for $P(F_c)$ so obtained was tested with our form, Eq. (5.12) and Bell-Evans form, Eq. (5.11) to see the degree of agreement.The process was repeated for different pulling rates $KV = 10^{-5}\,\mathrm{pN/\mu s}$ to $0.06\,\mathrm{pN/\mu s}$ to determine how these expressions fare in the slow, intermediate, and fast pulling regimes. This sums up our numerical work for 2D work.

For the numerical simulation in effective 1D landscape obtained from 2D landscape, since we were unable to produce the closed-form expression for reconstructed 1D landscape, we used the technique of mathematical spline. The work we adopted was similar to Sec. III of Ref. 84, except we used the spline function instead of generic form of 1D landscape. To be precise, we used the cubic spline.

5.4 Results

In this section, we mostly focussed on two aspects: 2D simulation results and the degree of convergence between 2D simulation and 1D simulation for the projected landscape. For 2D simulation results, we inspected the impact of pulling rate and rotation angle on the critical or rupture force and the reliability of Eq. (5.1) over Eq. (5.2). For this part, we used critical force values and cumulative probability distribution of the critical force given by equations Eq. (5.11) and Eq. (5.12).

In Fig. 5.3, we can see the impact of rotating angle on cumulative probability distribution of the rupture force at constant pulling rate. We can clearly observe cumulative probability distribution curves shifting towards the right with increasing pulling angle. This is reasonable as zero angle meant the most efficient pulling (as our wells are aligned perfectly along x-axis) and increasing pulling angle would make the pulling process less and less efficient. So, to generate the equal pulling effect, increase in pulling angle meant pulling rate needed to be higher. As a result, cumulative probability density curves keep shifting towards the right as we keep on increasing pulling angle.

Also, the shift in these curves become less and less apparent as we keep on increasing the value of pulling rate. This is again understandable as faster pulling would have more effect than

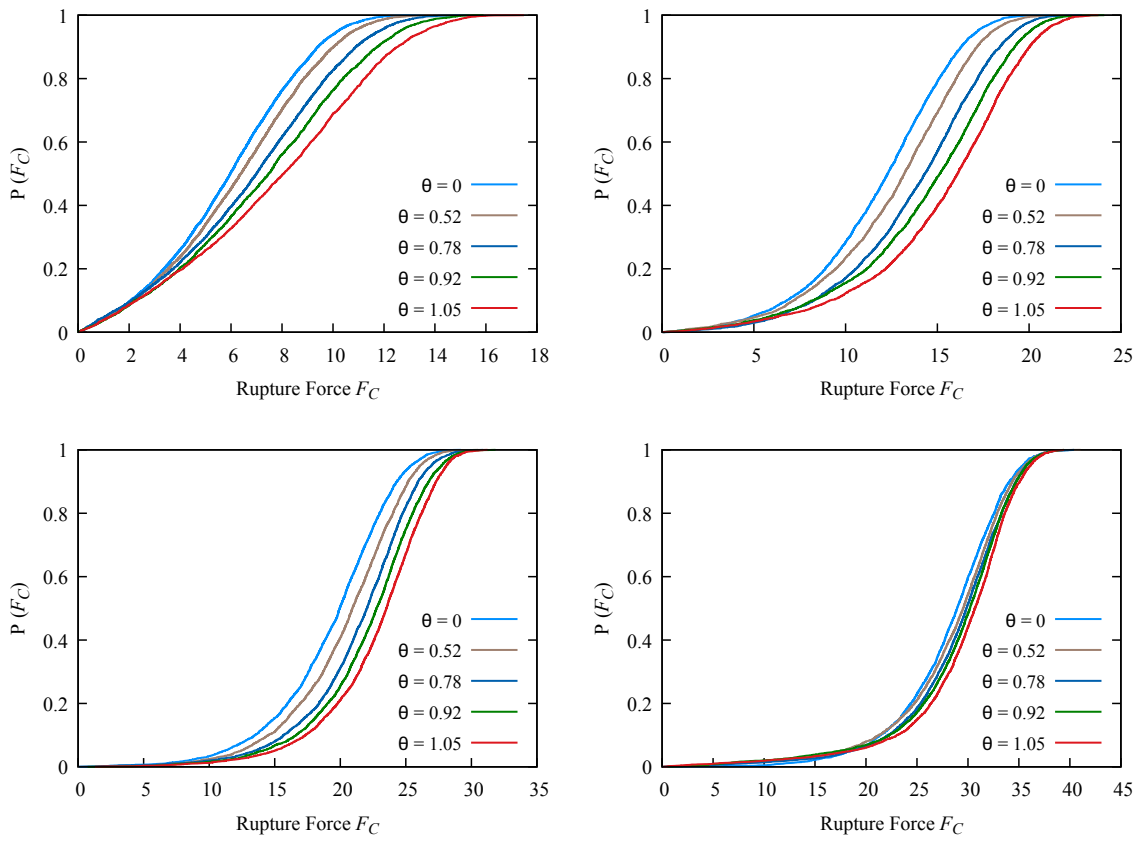

Figure 5.3. Cumulative probability distribution of the critical or rupture force as a function of rotating angle θ measured in radian for different pulling rates: (top left), (top right), (bottom left), (bottom right) for $KV = 2 \times 10^{-5}\,\mathrm{pN\,\mu s^{-1}}, 2 \times 10^{-4}\,\mathrm{pN\,\mu s^{-1}}, 2 \times 10^{-3}\,\mathrm{pN\,\mu s^{-1}}, 2 \times 10^{-2}\,\mathrm{pN\,\mu s^{-1}}$ respectively. Increase in rotating angle θ shifts the cumulative probability density curve towards right. However, the shift becomes almost non existent for higher pulling rates.

the misalignment between two wells.

Similarly as revealed in Fig. 5.4, the increase in pulling rate shifted the cumulative probability of the rupture force towards right which totally makes sense as higher rate of pulling accumulates higher pulling force by the time particle crosses the barrier or barrier vanishes.

We also went ahead and tested the value of the critical force as a function of pulling rates and rotation angle theta. In Fig. 5.5 (top), we can see the plot for the relative critical force as a function of pulling angle for different pulling rates. For lower pulling rates, the increase in theta would significantly increase the value of the rupture force. However, for faster pulling, the rotation angle would produce a small increase in relative rupture force values agreeing the result produced

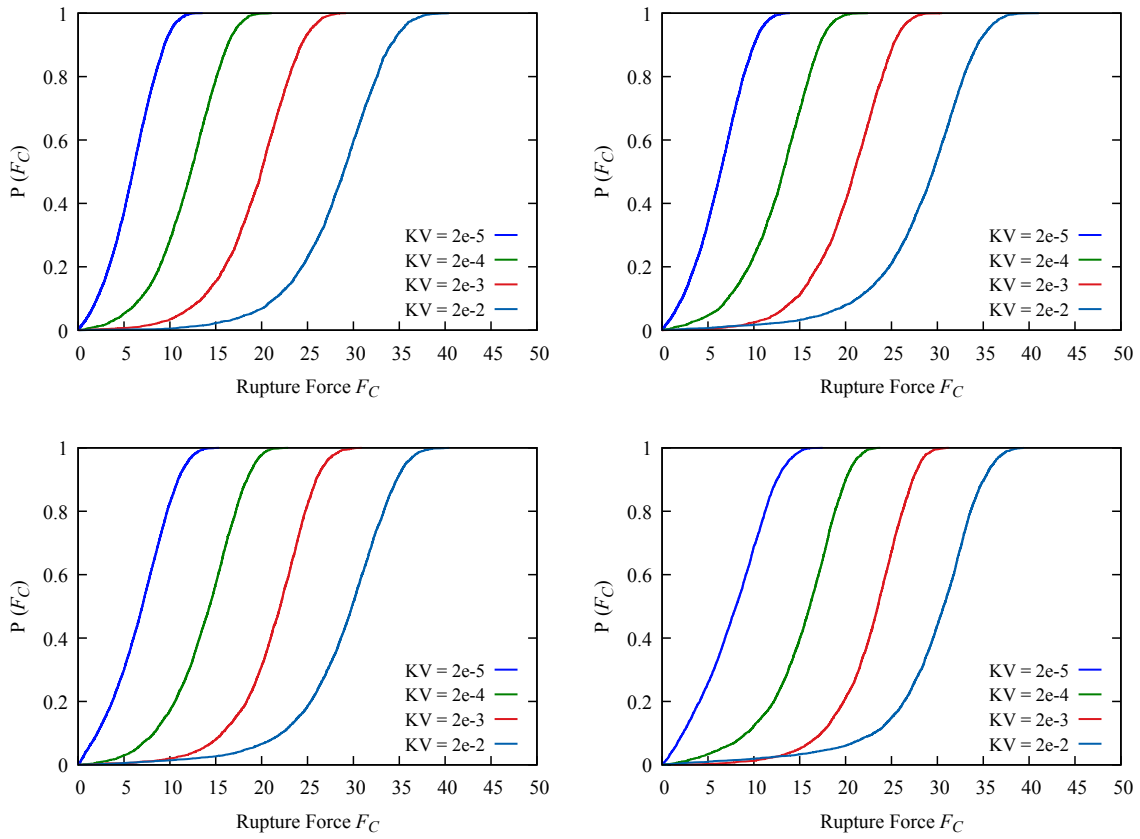

Figure 5.4. Cumulative probability distribution of the critical or rupture force as a function of pulling rate for different pulling angles θ: (top left), (top right), (bottom left), (bottom right), for $\theta = 0, 0.52, 0.78, 1.05$ radians respectively. Increase in pulling rate KV shifts the cumulative probability density curve towards right.

in Fig. 5.3. Also in Fig. 5.5 (bottom), the plot of critical force as a function of pulling rates for different rotation angles can be seen. As seen in the plot, the value of critical force would be larger for higher rotation angle as expected. Also, the difference in the critical force values will be less noticeable as we go on increasing the value of pulling rate. This is totally in agreement with earlier result produced.

We also tried to compute the well escape rate when there was no pulling involved. Just for a sanity check we recorded the value of this intrinsic rate as a function of the rotating angle using numerical simulation. Within error-bars, the values of intrinsic rate were equal for all pulling angles as seen in Fig. 5.6 . This totally makes sense as the well escape rate would not change just

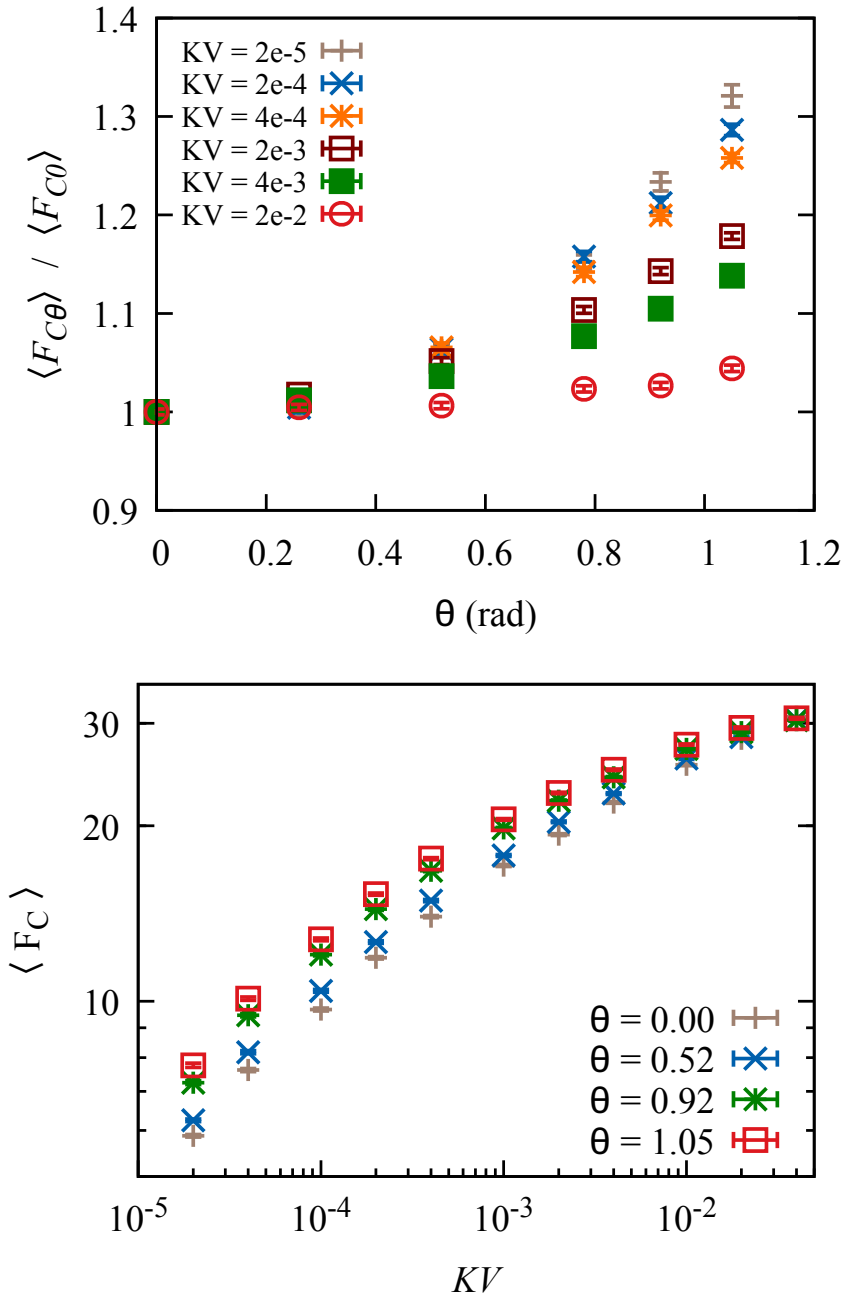

Figure 5.5. Top, relative average values of rupture force as a function of rotating angle θ for different pulling rates. The effect of rotation on rupture force goes on decreasing for increase in pulling rate. Bottom, average rupture force as a function of pulling rates for different pulling angle theta. For larger values of pulling rates rotation does have less impact as compared to smaller pulling rates.

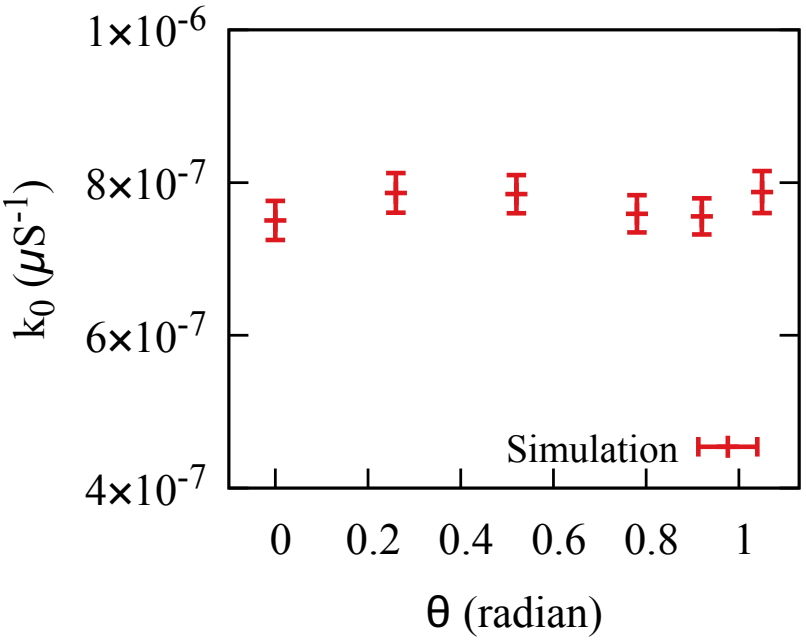

Figure 5.6. Intrinsic well escape rate as a function of rotating angle θ without the application of pulling force. There is no effect of rotation on rate as expected. The values of rate for all angles fall within the error range.

by the rotation of landscape if no pulling force is applied.

Fig. 5.7 reflects the reliability of Eq. (5.12) over Eq. (5.11). As seen in this plot, the simulated data agreed much better with the resummed form than Bell-Evans form up to higher pulling rates. For lower pulling rates 1×10^{-5} pN/μs and 2×10^{-4} pN/μs, both forms agreed nicely with simulation but as pulling rate was increased up to 2×10^{-3} pN/μs, the resummed form agreed better and Bell-Evans form started to deviate significantly from simulation as depicted by Fig. 5.7. This deviation was more pronounced when pulling rate was 2×10^{-2} pN/μs. Hence, the simulated results agreed upto much larger pulling rate with the resummed form than Bell-Evans form. This showcases the reliability of resummed form over Bell-Evans form.

As a next step, the simulation results for 2D landscape and its counterpart 1D landscape obtained from projection were analyzed to see the degree of convergence between them. For this work, we used the cumulative probability distribution analysis. We conducted the simulation for these landscapes using same pulling rate and tried to see if the cumulative probability curves

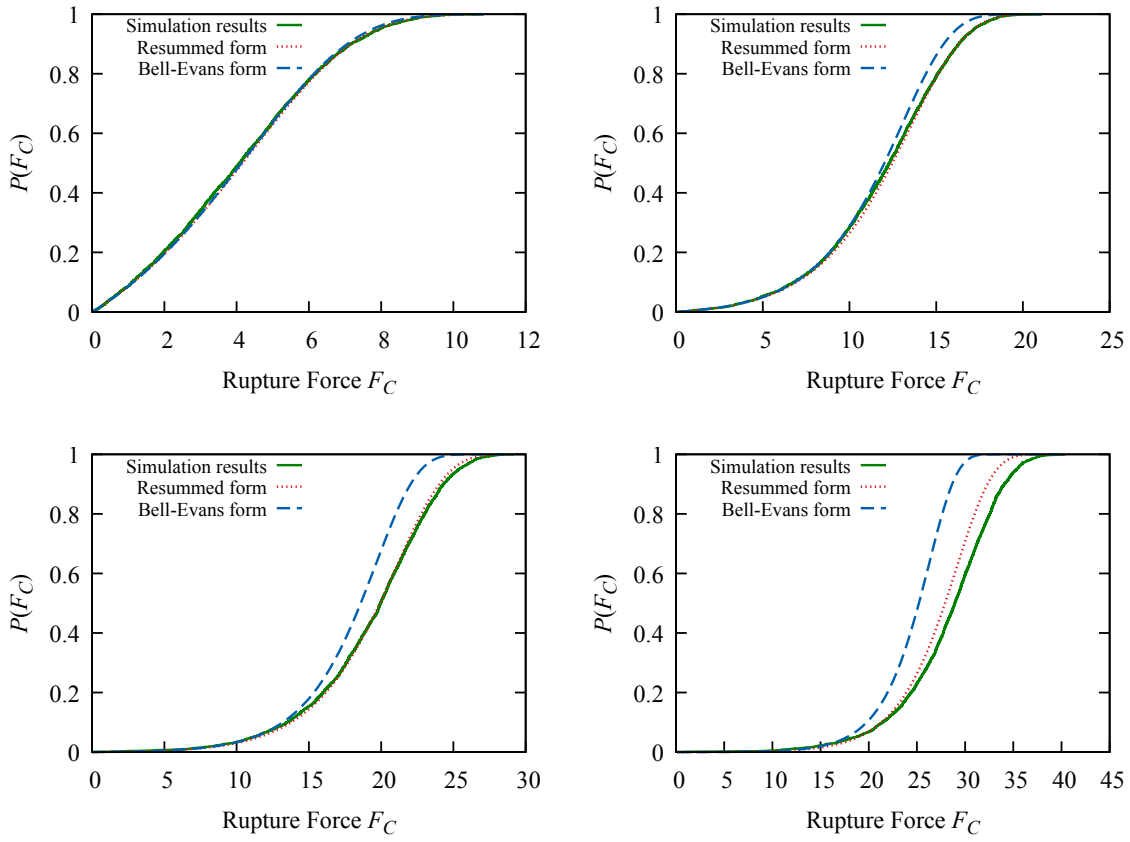

Figure 5.7. Cumulative probability distribution of the critical or rupture force for $KV = 1 \times 10^{-5}$ pN/μs (top left), $KV = 2 \times 10^{-4}$ pN/μs (top right), $KV = 2 \times 10^{-3}$ pN/μs (bottom left), and $KV = 2 \times 10^{-2}$ pN/μs (bottom right) as given by Bell-Evans form and our resummed form tested against simulation data. The resummed form traces the curve for simulated data upto much larger value of pulling rate as compared to Bell-Evans.

coincide with each other. We obtained some promising results as depicted in Fig. 5.8 which shows nice agreement between these two simulations at high damping regime when the 2D landscape was not rotated.

However, this agreement starts to fail if we consider the rotated landscape and its 1D counterpart obtained after projection. This totally makes sense as the hidden variable gets wiped out and can no longer be extracted from the projected 1D landscape obtained from the rotated 2D landscape. Another reason, as pointed earlier, might be multiple possible transition trajectories while going from the unfolded state to the folded state in 2D landscape which is not the case for the 1D landscape. This shortcoming highlights the suboptimal nature of the 1D analysis. That being

said, the agreement between these two simulations was not far off even for the rotated 2D landscape and its projected 1D counterpart. The degree of convergence so obtained was pretty promising. Overall, this work highlighted both the degree of complexity and the reliability of projection of multidimensional landscape onto the lower dimensional landscape.

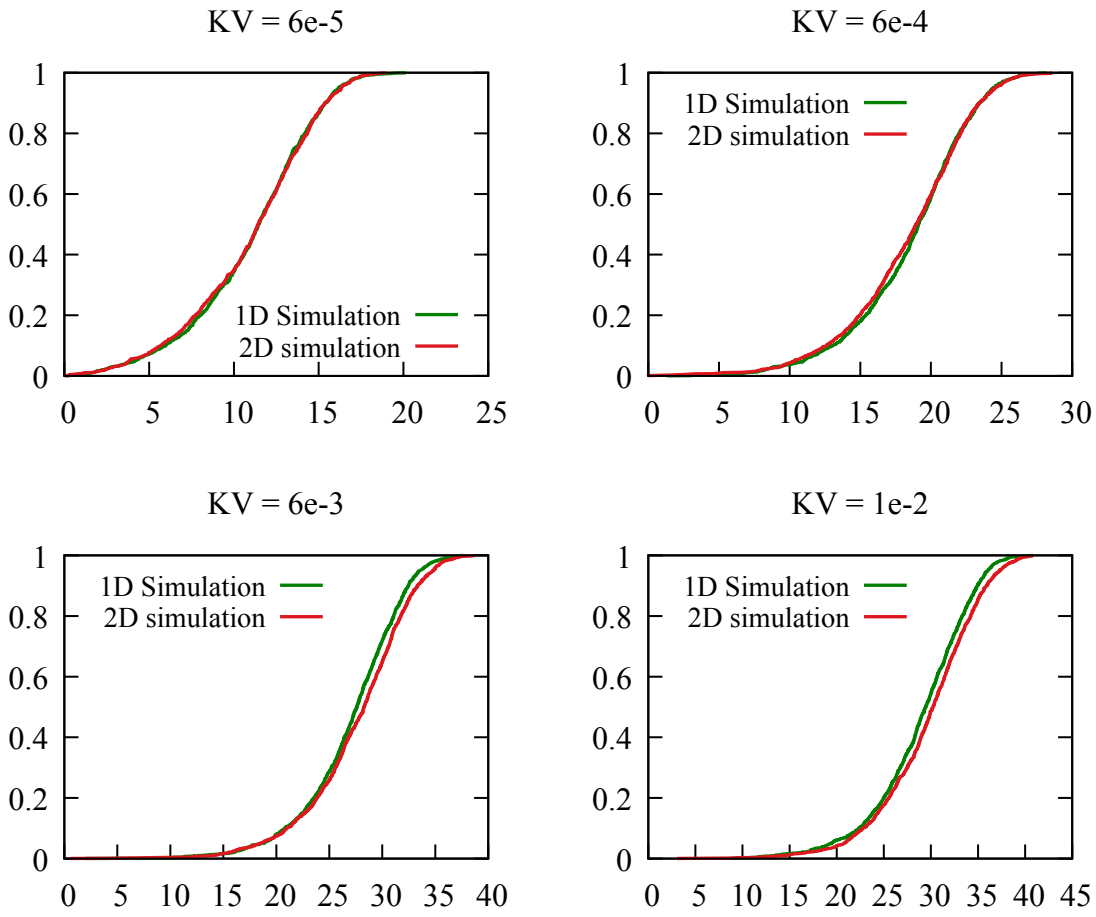

Figure 5.8. Cumulative probability distribution of the critical or rupture force for different pulling rates $KV = 6 \times 10^{-5}$ pN/µs (top left), $KV = 6 \times 10^{-4}$ pN/µs (top right), $KV = 6 \times 10^{-3}$ pN/µs (bottom left), and $KV = 1 \times 10^{-2}$ pN/µs (bottom right) for 2D landscape and reconstructed 1D counterpart. Simulations in both landscapes almost matched perfectly under suitable rescaling.

5.5 Conclusions

To sum up, this work presents a 2D model for well escape rate within certain analytic framework, obtains the more reliable from of rate equation for 2D analysis analytically and showcases

the reliability of this rate equation over preexisting form of rate equation with the help of numerical simulations. It also helps to display the art of projecting 2D landscape onto 1D landscape, highlights the complexities of projection and finally exhibits the degree of convergence between simulations carried out in these two landscapes. It shows how the downward projection of multidimensional landscape onto a lower dimension landscape might be suboptimal and the results obtained from these two landscapes might be different. Above all, this method addresses the suboptimal nature of 1D analysis and somehow overcomes it.

CHAPTER 6

MONTE CARLO SIMULATIONS REVEAL LIMITATIONS OF THE SINGLE-REACTION-COORDINATE PICTURE

6.1 Introduction

A random walk through an energy landscape is a meaningful picture of the motion of a biopolymer. As the walk proceeds, the chains explores the phase space of all possible conformations. Several discrete lattice models [109, 110] have been proposed and implemented to explain random-walk chains but our focus will be on such chains moving in the continuum. Implementation is somewhat more challenging in comparison to the work in discrete lattice space. In our modeling, we have taken into consideration the nearest-neighbor bending cost and various possible long-range interactions, including the excluded volume interaction, hydrophobic attraction, and electrostatic interaction. Each of these interaction terms are cumulatively to produce the complete interaction potential. The interaction potential had the form given by Eq. (1.15). The chain was then allowed to execute the random walk constrained by this interaction potential. Two different kinds of update schemes, pivot and site rotation were incorporated in combination with efficient sampling techniques such as replica-exchange parallel tempering to produce an ergodic and efficient exploration of the phase space. Each the update was accepted or rejected with the standard Metropolis criterion. Complete details were given in Ch. 2.

The main purpose of this work is to implement 2D framework to semi-realistic polymers apart from the 2D abstract energy landscape discussed in Ch. 5 and develop a clear conceptual understanding about the secondary reaction coordinate. It was meant to highlight the limitations of the conventional analysis of pulling experiments that assumes projection onto a single reaction coordinate. Though we are still not clear about the secondary reaction coordinate, we believe

cylindrical radius of gyration could be a possibility. We tested all the preliminary results against the preexisting theories to make sure our simulation setup worked correctly. We extracted the values of different observables and interpreted their physical significance.

6.2 Theoretical model

For this work, we considered a protein chain with N monomers A_i ($i = 0, 1, \ldots, N-1$) of diameter a separated by bond length b. These monomers were assumed to be hydrophobic, positive, negative, or neutral. A monomer site was randomly chosen and the portion of chain after that site was allowed to rotate freely about it—the so-called pivot rotation. Furthermore, each monomer site was allowed to rotate about the line connect its two neighbors in the backbone. This update scheme was called site rotation. The values of pivot and site rotation angles were drawn from the uniform distribution on slice of the interval $(-\pi, \pi)$. We used active feedback to adjust the angular opening of the updates: it was adjusted until the acceptance fraction of the simulation fell in the range 25–75%. The cylindrical coordinate system was taken into consideration as we tried to keep track of secondary reaction coordinate, radius of gyration perpendicular to primary reaction coordinate, end-to-end length as shown in Fig. 1.9.

We incorporated nearest-neighbor bending cost and several possible long-range interactions such as: excluded volume interaction, hydrophobic attraction, and coulomb interaction to construct an interaction potential of the form Eq. (1.15). This potential constrained the motion of chain under different update schemes.

6.3 Numerical work

The numerical simulation for this work was done using Metropolis Monte Carlo simulation [87]. The straight chain was taken as the initial state. It was then allowed to explore the energy space constrained by the interaction potential and using different update schemes mentioned earlier. Next step was accepted if either $\Delta E < 0$ or ratio of probabilities of two successive states, $\exp(-\Delta E/k_B T)$ was greater than a small randomly generated number from uniform distribution

between 0 and 1. At $T = 0$ this was simply a steepest descent problem in energy as shown in Fig. 6.1 but we are simulating at $T > 0$ which allows for the move that explores uphill.

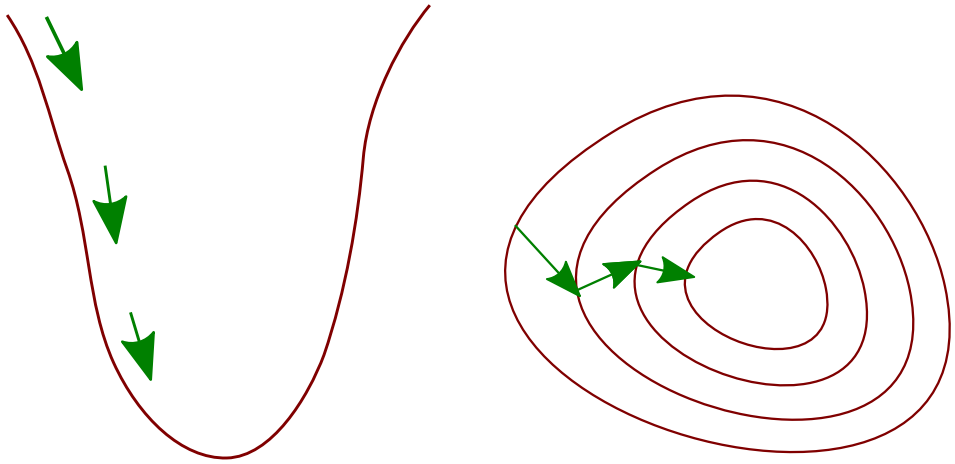

Figure 6.1. The figure showing steepest descent algorithm in 1D landscape (left) and 2D landscape (right).

This simulation was carried out for different values of $k_B T$ and N, the number of monomers in the chain. Initially it was done for a general size of chain but later semi-realistic protein chain were taken into the consideration. We performed the simulation by considering the interaction potential with only bending energy term at the beginning and then adding interaction terms step by step to see their impact. Several parameters such as end-to-end distance, radius of gyration, square of end-to-end distance, and binder ratio were computed in each such steps. We also obtained 2D histogram plot for cylindrical radius of gyration versus end-to-end length to see if we could develop concrete understanding behind secondary reaction coordinate of interest. There were some challenges as simulation got stuck in local minima at times. To overcome this issue we used sampling techniques such as replica exchange parallel tempering and adaptive biasing. These are described in details in Ch. 2. We wrote and implemented the graphical version of code using openGL to visualize the chain evolution. Snapshots of the running simulation are included in Fig. 6.2.

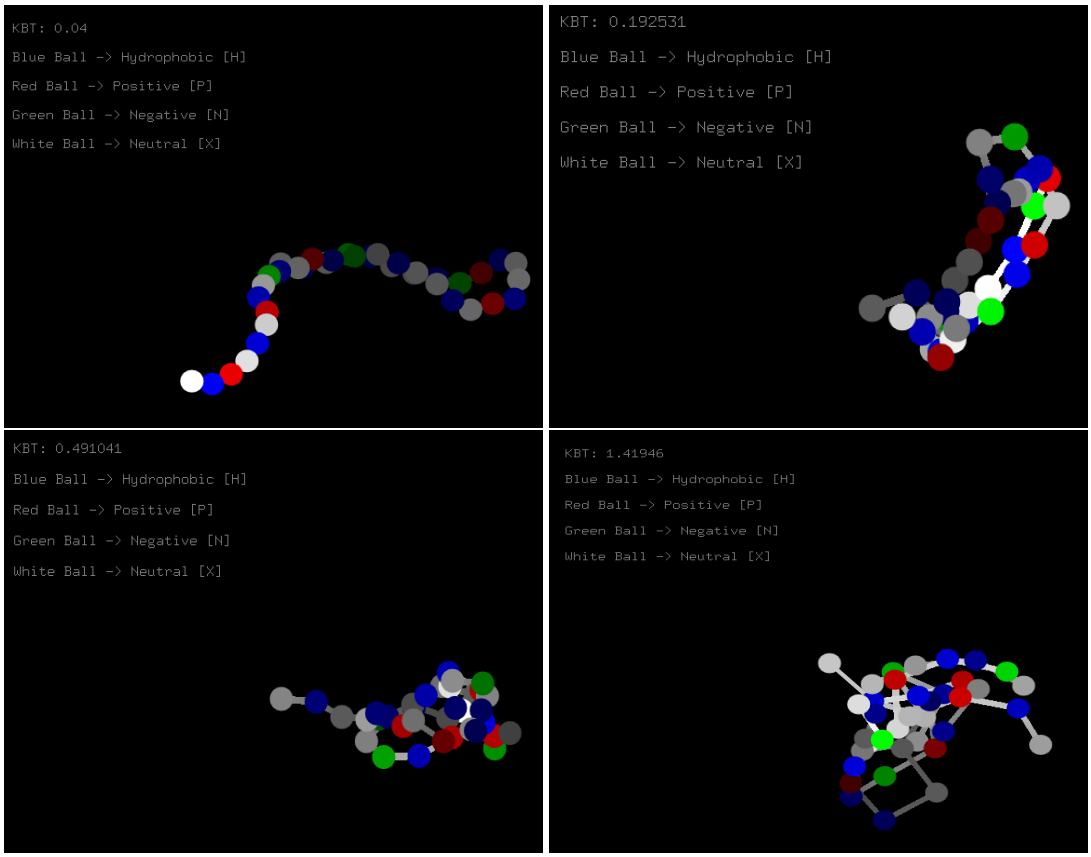

Figure 6.2. The figure showing the snapshots of the chain motion as depicted by our openGL program for different k_BT values. Each of these spheres represented monomers. Different colors are used for different spheres; blue for hydrophobic, red for positive, green for negative and white for neutral. Increase in temperature seem to favor more crumpled state.

6.4 Preliminary Results

The main purpose of this project was to implement our 2D framework to semi realistic protein chain and interpret our results obtained for abstract 2D landscape. For that work the first important step would be to see if the Monte Carlo simulation setup works correctly and produces the data which agrees with the preexisting theories.

As a first step, we took an ideal chain into consideration. We included only the bending term in interaction potential and generated data for $J = 1$. We obtained plots for different parameters like end-to-end length and end-to-end length squared as a function of k_BT as shown in Fig. 6.3 , top panel. We also obtained the plots of end-to-end length and end-to-end length squared as a function

of N as shown in Fig. 6.3, bottom panel, from which we can clearly see that for for low k_BT i.e, $k_BT = 9 \times 10^{-5}$, $\langle L \rangle \sim N$ and $\langle L^2 \rangle \sim N^2$. However, for much higher k_BT i.e, $k_BT = 600$, we could see $\langle L \rangle \sim N^{0.5}$ and $\langle L^2 \rangle \sim N^{2\times0.5}$. The result obtained in Fig. 6.3 corroborates this. Here, we can clearly see the data collapse for both $\langle L \rangle / N^{0.5}$ and $\langle L^2 \rangle / N^{2\times0.5}$ as $k_BT > J$. This meant for $k_BT > J$, $\langle L \rangle \sim N^{0.5}$ and $\langle L^2 \rangle \sim N^{2\times0.5}$. This is in agreement with preexisting theories.

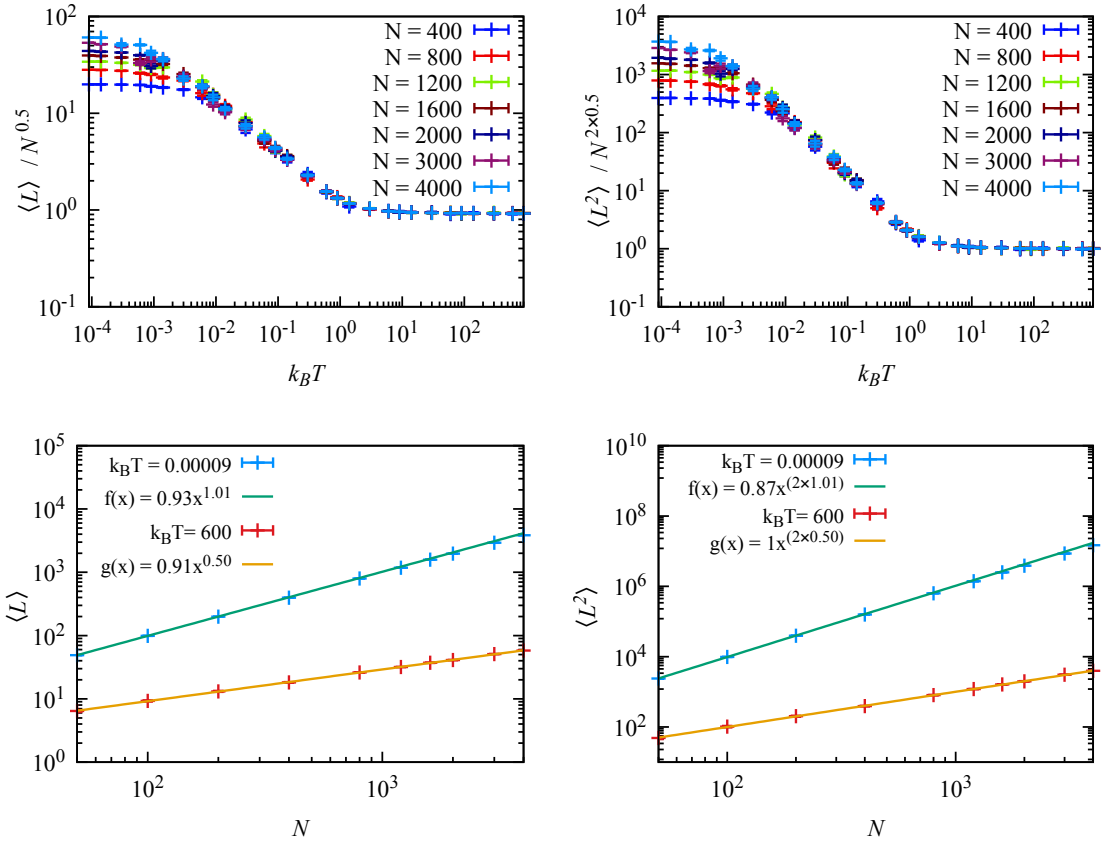

Figure 6.3. (Top left) The average end-to-end length versus k_BT. (Bottom left) The average end-to-end length versus N. (Top right) The average end-to-end length squared versus k_BT. (Bottom right) The average end-to-end length squared versus N.

As a next step, we included the excluded volume interaction term given by $V_{ij}^{EV} = V_0\Theta(a - r_{ij})$ with $V_0 = 100$. Then, we ran the simulation to see the variation of previously mentioned parameters as a function of k_BT. The result was pretty much as expected. We could see the chain exhibiting self avoiding walk (SAW) when $J < k_BT < V_0$ and going towards random walk when $k_BT > V_0$. The plot of $\langle L \rangle / N^{0.59}$ and $\langle L^2 \rangle / N^{2\times0.59}$ both collapsed for single line for different N when $1 <$

$k_BT < 100$ as seen in Fig. 6.4, top panel. In other words the chain exhibited SAW in this range which again agrees totally with preexisting theories. This can also be seen in Fig. 6.4, bottom panel. The fit of $\langle L \rangle$ vs N^{α} produced values of α to be 1.01, 0.58 and 0.54 for $k_BT < J$, $J < k_BT < V_0$ and $k_BT > V_0$ respectively. Similarly, the fit of $\langle L^2 \rangle$ vs $N^{2\alpha}$ produced values of α to be 1.01, 0.58 and 0.54 for $k_BT < J$, $J < k_BT < V_0$ and $k_BT > V_0$ respectively. These results obtained so far highlight the robustness of our simulation.

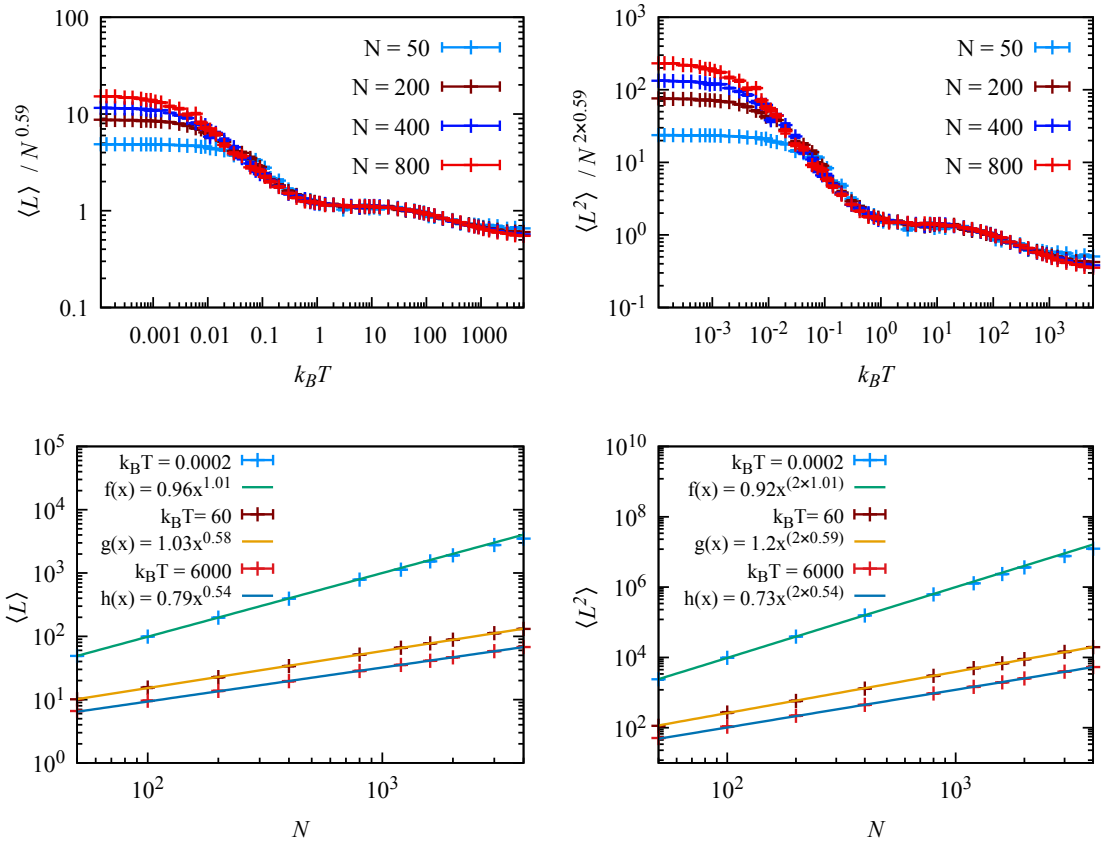

Figure 6.4. (Top left) The average end-to-end length versus k_BT. (Bottom left) The average end-to-end length versus N. (Top right) The average end-to-end length squared versus k_BT. (Bottom right) The average end-to-end length squared versus N.

We also went on to incorporate other long-range interaction terms and obtained two-dimensional grid plots. Some of these plots obtained are depicted in Fig. 6.5. The simulation was carried out for different k_BT values such as 0.02, 0.06, 0.1 and 1. As seen in these plots, the value of average end-to-end length kept on decreasing with increasing temperature favoring the crumpled

state at higher temperatures. However, the average values of cylindrical radius of gyration first increased and again started decreasing with increase in temperature. This is still a work in progress and we are continuously working on it and we even plan to collaborate on this work after my graduation.

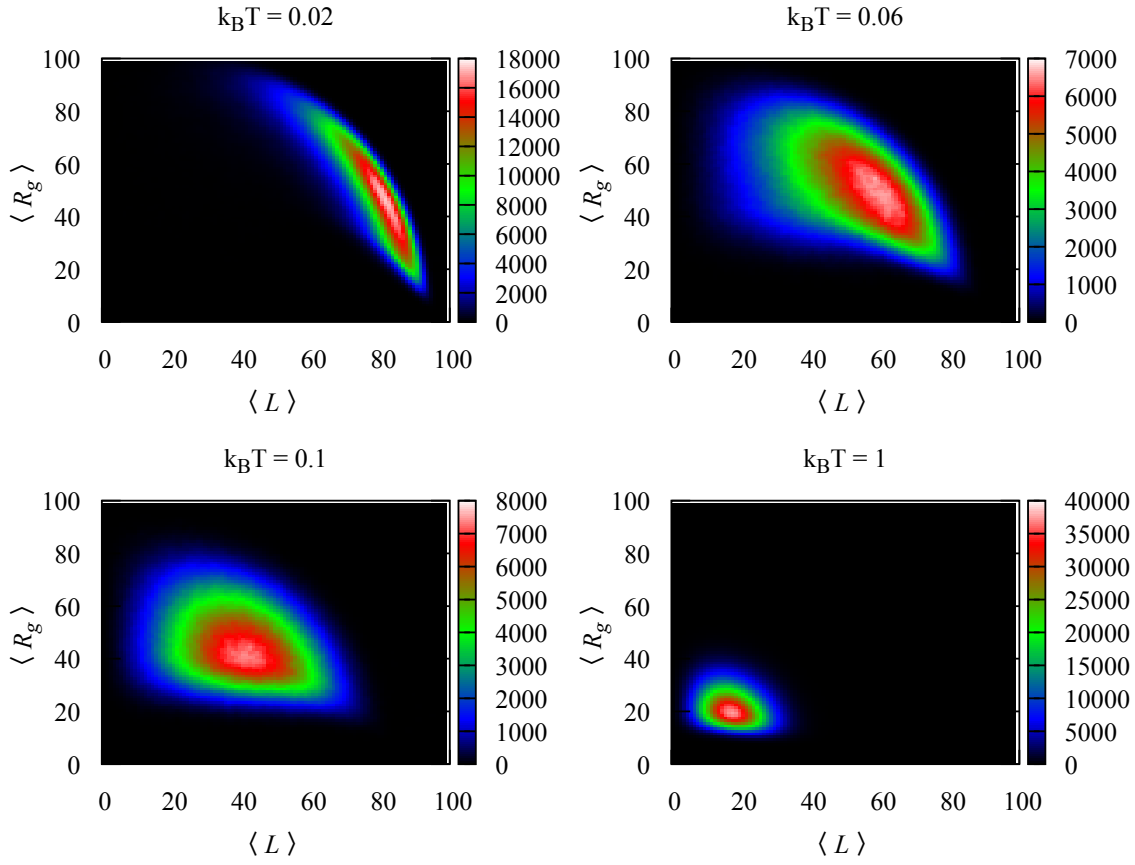

Figure 6.5. Two-dimensional grid plots of end-to-end length $\langle L \rangle$ and radius of gyration $\langle R_g \rangle$ for different values of temperature. The chain seems to favor the crumpled state for larger temperatures.

6.5 Conclusions

This work overall has been promising so far. It still has lots of prospects as the simulation works perfectly fine and data generation, data analysis and data visualization phase is still ongoing. From preliminary results obtained so far, this work seems to strengthen the claim of 1D model being suboptimal. However, there are certain challenges associated with it too. Being able to

fine tune the strength of long range interaction terms to represent the physical system representing biological system is a big challenge. The computational techniques used in this project is widely used in different real life applications such as protein modeling in drug discovery. The immediate next step for this work would be to obtain data for different temperatures from the simulation and obtain two-dimensional grid plot to find two metastable states. It is somewhat similar to the conformational search implemented in a drug discovery projects.

CHAPTER 7

SUMMARY

In this dissertation, we considered the mechanical unfolding of biopolymers, such as proteins, in context of the activated barrier crossing problem. The response of biopolymers to applied force is very important in understanding their mechanical stability and in characterizing the energy barriers that govern their diffusion through unfolding pathways. We have reported on three completed projects and a fourth that is ongoing. The background literature is discussed in Ch. 1. It is comprised of both past and recent developments in the field.

In Ch. 2, the methods adopted in this dissertation, both analytic and numerical, have been explained thoroughly. Particular attention has been paid to the numerical methods for simulation: one-dimensional heat-bath-coupled Langevin dynamics; its two-dimensional generalization with added optimization techniques; and Monte Carlo with some enhanced sampling techniques including replica-exchange parallel tempering and adaptive biasing force. These methods helped in achieving our goals set for the dissertation.

Ch. 3 addressed the reliable extraction of energy landscape properties from the critical force distribution. Using simulated data mimicking pulling experiments carried out with optical tweezers, we flagged the weakness and pathological points in the rate equations that are typically used to fit the measured rate in real experiments. The simulation was carried out using one-dimensional bi-quadratic landscape where a barrier separated the folded and unfolded wells. We proposed our own form of rate equation analytically and showcased with the help of numerical work that this form was more reliable both in case of prediction (forward modeling) and parameter extraction (inverse modeling). This work has been published in the journal Physical Review Research [84].

In Ch. 4, we developed a comprehensive framework for universality in the context of activated barrier crossing under bias. The robustness of this model was validated using data

collpase, obtained from the numerical simulation for a wide range of temperatures and family of potential landscapes with different shape parameters. We were able to obtain a striking agreement between two different kind of analyses, constant force and constant loading rate analysis. A manuscript based on this work is under review at Physical Review Letters and is already available on the arXiv preprint server [111].

One dimensional analysis discussed earlier may not always be optimal, especially protein with knots and multiple transition pathways. At these scenarios, or when the chains are degenerate in length but with different conformational state, one dimensional analysis with single reaction coordinate mostly fails. This motivated us to come up with two dimensional generalization. We explored the possibility of adding a secondary reaction coordinate perpendicular to the primary reaction coordinate and generalized our 1D analytic model to 2D. We then carried out 2D simulation in an abstract 2D landscape and showcased the robustness of our 2D rate equation in both prediction and well parameter extraction. Under certain condition, we were even able to reproduce 1D results from 2D simulation thereby showing a nice degree of convergence between two analyses. This was our third project and is on Ch. 5 of the dissertation.

Finally, we were motivated to test the physical form of secondary reaction coordinate as we found 2D simulation worked well with an abstract 2D landscape. This work is our fourth project and is in Ch. 6. We adopted a different approaches for this work. We created an energy landscape for a protein chain considering backbone interaction and long range interactions such as excluded volume, hydrophobic and electrostatic interaction. Allowing two different kind of update schemes, we let this chain explore the energy space randomly accepting/rejecting next steps using Monte Carlo simulation. We recorded the end-to-end chain length as a primary reaction coordinate and cylindrical radius of gyration as secondary reaction coordinate. Preliminary results show that the cylindrical radius of gyration is a good candidate for the secondary reaction coordinate for 2D analysis. Exploring other forms of secondary reaction coordinates such as ‘native contact’ can be continued in future project.

LIST OF REFERENCES

[1] D. A. Brant, Conformational analysis of biopolymers: Conformational energy calculations, Annual Review of Biophysics and Bioengineering **1**, 369–408 (1972).

[2] J. D. Bryngelson and P. G. Wolynes, Spin glasses and the statistical mechanics of protein folding, Proceedings of the National Academy of Sciences **84** (1987).

[3] J. N. Onuchic, Z. Luthey-Schulten, and P. G. Wolynes, Theory of protein folding: the energy landscape perspective, Annual Reviews of Physical Chemistry **48** (1997).

[4] J. N. Onuchic, H. Nymeyer, A. E. García, J. Chahine, and N. D. Socci, The energy landscape of protein folding: Insights into folding mechanisms and scenarios, Advances in Protein Chemistry **53** (2000).

[5] M. Stöhr and A. Tkatchenko, Quantum mechanics of proteins in explicit water: The role of plasmon-like solute-solvent interactions, Science Advances **5**, 13278–13282 (2019).

[6] J. V. Galzitskaya and A. V. Finkelstein, A theoretical search for folding/unfolding nuclei in three-dimensional protein structures, Proceedings of the National Academy of Sciences **96** (1999).

[7] J. N. Onuchic and P. G. Wolynes, Theory of protein folding, Current Opinion in Structural Biology **14** (2004).

[8] K. A. Dill and J. L. MacCallum, The protein-folding problem, 50 years on, Science **338** (2012).

[9] P. Talkner and D. Ryter, Lifetime of a metastable state at low noise, Physics Letters A **88** (1982).

[10] R. Merkel, P. Nassoy, A. Leung, K. Ritchie, and E. Evans, Energy landscapes of receptor-ligand bonds explored with dynamic force spectroscopy, Nature **397** (1999).

[11] J. Liphardt, B. Onoa, S. Smith, I. .Tinoco, and C. Bustamante, Reversible unfolding of single rna molecules by mechanical force, Science **292** (2001).

[12] P. Li and D. E. Makarov, Simulation of the mechanical unfolding of ubiquitin: Probing different unfolding reaction coordinates by changing the pulling geometry, Journal of Chemical Physics **121** (2004).

[13] P. Hinterderfer and Y. Dufrene, Detection and localization of single molecular recognition events using atomic force microscopy, Nature Methods **3** (2006).

[14] Y. Gilbert, M. Deghorain, L. Wang, B. Xu, P. D. Pollheimer, H. J. Gruber, J. Errington, B. Hallet, X. Haulot, C. Verbelen, P. Hols, and Y. F. Dufrene, Single-molecule force spectroscopy and imaging of the vancomycin/d-ala-d-ala interaction, Nano Letters **7** (2007).

[15] W. J. Greenleaf, M. T. Woodside, and S. M. Block, High-resolution, single-molecule measurements of biomolecular motion, Annual Review of Biophysics and Biomolecular Structure **36** (2007).

[16] K. Neupane, H. Yu, D. A. N. Foster, F. Wang, and M. Woodside, Single-molecule force spectroscopy of the add adenine riboswitch relates folding to regulatory mechanism, Nucleic Acids Research **39** (2011).

[17] D. E. Souza, Pulling on single molecules, Nature Methods **9** (2012).

[18] M. S. Bull, R. M. A. Sullan, H. Li, and T. T. Perkins, Improved single molecule force spectroscopy using micromachined cantilevers, ACS Nano **8** (2014).

[19] D. T. Edwards, J. K. Faulk, A. W. Sanders, M. S. Bull, R. Walder, M.-A. LeBlanc, M. C. Sousa, and T. T. Perkins, Optimizing 1-µs-resolution single-molecule force spectroscopy on a commercial atomic force microscope, Nano Letters **15** (2015).

[20] S. R. Okoniewski, L. Uyetake, and T. T. Perkins, Force-activated dna substrates for probing individual proteins interacting with single-stranded dna, Nucleic Acids Research **45** (2017).

[21] H. Yu, M. G. W. Siewny, D. Edwards, A. W. Sanders, and T. T. Perkins, Hidden dynamics in the unfolding of individual bacteriorhodopsin proteins, Science **355** (2017).

[22] R. Walder, W. J. V. Patten, A. Adhikari, and T. T. Perkins, Going vertical to improve the accuracy of atomic force microscopy based single-molecule force spectroscopy, ACS Nano **12** (2018).

[23] R. Walder, W. J. V. Patten, D. B. Ritchie, R. K. Montange, T. W. Miller, M. T. Woodside, and T. T. Perkins, High-precision single-molecule characterization of the folding of an hiv rna hairpin by atomic force microscopy, Nano Letters **18** (2018).

[24] C. Jarzynski, Nonequilibrium equality of free energy differences, Physical Review Letters **78** (1997).

[25] G. Hummer and A. Szabo, Free energy reconstruction from nonequilibrium single-molecule pulling experiments, Proceedings of the National Academy of Sciences **98** (2001).

[26] N. C. Harris, Y. Song, and C. H. Kiang, Experimental free energy reconstruction from single molecule force spectroscopy using jarzynski's inequlity, Physical Review Letters **99** (2007).

[27] A. N. Gupta, A. Vincent, K. Neupane, H. Yu, F. Wang, and M. T. Woodside, Experimental validation of free-energy-landscape reconstruction from non-equilibrium single-molecule force spectroscopy measurements, Nature Physics **7** (2011).

[28] Q. Zhang, J. Brujic, and E. V. Eijnden, Reconstructing free energy profiles from nonequilibrium relaxation trajectories, Journal of Statistical Physics **144** (2011).

[29] M. C. Engel, D. B. Ritchie, D. A. N. Foster, K. S. D. Beach, and M. T. Woodside, Reconstructing folding energy landscape profiles from nonequilibrium pulling curves with an inverse weierstrass integral transform, Physical Review Letters **113** (2014).

[30] A. P. Manuel, J. Lambert, and M. T. Woodside, Reconstructing folding energy landscapes from splitting probability analysis of single-molecule trajectories, Proceedings of the National Academy of Sciences **112** (2015).

[31] P. R. Heenan, H. Yu, M. G. W. Siewny, and T. T. Perkins, Improved free-energy landscape reconstruction of bacteriorhodopsin highlights local variations in unfolding energy, Journal of Chemical Physics **148** (2018).

[32] N. J. L. Alamilla, M. W. Jack, and K. J. Challis, Analysing single-molecule trajectories to reconstruct free-energy landscapes of cyclic motor proteins, Journal of Theoretical Biology **462** (2019).

[33] N. J. L. Alamilla, M. W. Jack, and K. J. Challis, Reconstructing free-energy landscapes for cyclic molecular motors using full multidimensional or partial one-dimensional dynamic information, Physical Review E **462** (2019).

[34] H. A. Kramers, Brownian motion in a field of force and the diffusion model of chemical reactions, Physica **7** (1940).

[35] R. F. Grote and J. T. Hynes, The stable states picture of chemical reactions. ii. rate constants for condensed and gas phase reaction models, Journal of Chemical Physics **73** (1980).

[36] E. Pollak, Theory of activated rate processes: A new derivation of kramers' expression, Journal of Chemical Physics **85** (1986).

[37] P. Hänggi, P. Talkner, and M. Borkovec, Reaction-rate theory: fifty years after kramers, Reviews of Modern Physics **62** (1990).

[38] G. R. Fleming, S. H. Courtney, and M. W. Balk, Activated barrier crossing: Comparison of experiment and theory, Journal of Statistical Physics **42** (1986).

[39] G. R. Haynes and G. A. Voth, A theory for the activated barrier crossing rate constant in systems influenced by space and time dependent friction, Journal of chemical Physics **101** (1994).

[40] P. Kraikivski, R. Lipowsky, and J. Kierfeld, Barrier crossing of semiflexible polymers, Europhysics Letters **66** (2004).

[41] D. E. Makarov, Barrier crossing dynamics from single-molecule measurements, The Journal of Physical Chemistry B **125** (2021).

[42] R. M, G. M, O. F, F. JM, and G. HE, Reversible unfolding of individual titin immunoglobulin, Science **276** (1997).

[43] K. MS, S. SB, G. HL, and B. C, Folding - unfolding transitions in single titin molecules, Science **276** (1997).

[44] S. T. L, T. J, S. JA, and S. RM, Elasticity and unfolding of single molecules of the giant muscle protein titin, Nature **387** (1997).

[45] M. T. Woodside, C. García-García, and S. M. Block, Folding and unfolding single rna molecules under tension, Current Opinion in Chemical Biology **12** (2008).

[46] G. Žoldák and M. Rief, Force as a single molecule probe of multidimensional protein energy landscapes author links open overlay panel, Current Opinion in Structural Biology **23** (2008).

[47] A. Szabo, K. Schulten, and Z. Schulten, First passage time approach to diffusion controlled reactions, J. Chem. Phys. **72** (1980).

[48] H. S. Chung, J. M. Louis, and W. A. Eaton, Experimental determination of upper bound for transition path times in protein folding from single-molecule photon-by-photon trajectories, Proc. Natl. Acad. Sci. **106** (2009).

[49] S. Chaudhury and D. E. Makarov, A harmonic transition state approximation for the duration of reactive events in complex molecular rearrangements, J. Chem. Phys. **133** (2009).

[50] S. Kirmizialtin, L. Huang, and D. E. Makarov, Topography of the free-energy landscape probed via mechanical unfolding of proteins, Journal of Chemical Physics **122** (2005).

[51] M. T. Woodside, W. M. Behnke-Parks, K. Larizadeh, K. Travers, D. Herschlang, and S. M. Block, Nanomechanical measurements of the sequence-dependent folding landscapes of single nucleic acid hairpins, Proceedings of the National Academy of Sciences **103** (2006).

[52] R. B. Best and G. Hummer, Coordinate-dependent diffusion in protein folding, Proceedings of the National Academy of Sciences (USA) **107** (2010).

[53] O. K. Dudko, T. G. W. Graham, and R. B. Best, Locating the barrier for folding of single molecules under an external force, Physical Review Letters **107** (2011).

[54] A. N. G. H. Yu, X. Liu, K. Neupane, A. M. Brigley, I. Sosova, and M. T. Woodside, Energy landscape analysis of native folding of the prion protein yields the diffusion constant, transition path time, and rates, Proc. Natl. Acad. Sci. U.S.A. **109** (2012).

[55] W. J. V. Patten, R. Walder, A. Adhikari, S. R. Okoniewski, R. Ravichandran, C. E. Tinberg, D. Baker, and T. T. Perkins, Improved free-energy landscape quantification illustrated with a computationally designed protein-ligand interaction, ChemPhysChem **19** (2019).

[56] D. B. Ritchie and M. T. Woodside, Probing the structural dynamics of proteins and nucleic acids with optical tweezers, Current Opinion in Structural Biology **34** (2015).

[57] M. T. Woodside, J. Lambert, and K. S. D. Beach, Determining intrachain diffusion coefficients for biopolymer dynamics from single-molecule force spectroscopy measurements, Biophysical Journal **107** (2014).

[58] E. Evans, D. Berk, and A. Leung, Detachment of agglutinin-bonded red blood cells. i. forces to rupture molecular-point attachments, Biophysical Journal **59** (1991).

[59] M. Rief, F. O. M. Gautel, J. M. Fernandez, and H. E. Gaub, Reversible unfolding of individual titin immunoglobulin domains by afm, Science **276** (1997).

[60] M. Rief, J. M. Fernandez, and H. E. Gaub, Elastically coupled two- level systems as a model for biopolymer extensibility, Physical Review Letters **81** (1998).

[61] G. Hummer and A. Szabo, Kinetics from nonequilibrium single-molecule pulling experiments, Biophysical Journal **85** (2003).

[62] R. W. Friddle, Unified model of dynamic forced barrier crossing in single molecules, Physical Review Letters **100** (2008).

[63] J. C. M. Gebhardt, T. Bornschlögl, and M. Rie, Full distance-resolved folding energy landscape of one single protein molecule, Proceedings of the National Academy of Sciences (USA). **107** (2010).

[64] A. N. Gupta, A. Vincent, K. Neupane, H. Yu, F. Wang, and M. T. Woodside, Experimental validation of free-energy-landscape reconstruction from non-equilibrium single-molecule force spectroscopy measurements, Nature Physics **7** (2011).

[65] M. de Messieres, B. Brawn-Cinani, and A. L. Porta, Measuring the folding landscape of a harmonically constrained biopolymer, Biophysical Journal **100** (2011).

[66] M. T. Woodside and S. M. Block, Reconstructing folding energy landscapes by single-molecule force spectroscopy, Annual Review of Biophysics **43** (2014).

[67] G. I. Bell, Models for the specific adhesion of cells to cells, Science **200** (1978).

[68] O. K. Dudko, G. Hummer, and A. Szabo, Intrinsic rates and activation free energies from single-molecule pulling experiments, Physical Review Letters **96** (2006).

[69] K. C. Neuman and A. Nagy, Single-molecule force spectroscopy: optical tweezers, magnetic tweezers and atomic force microscopy, Nature Methods **5**, 491–505 (2008).

[70] A. Ashkin, J. M. Dziedzic, J. E. Bjorkholm, and S. Chu, Observation of a single-beam gradient force optical trap for dielectric particles, Optics Letters **11**, 288–290 (1986).

[71] A. Ashkin, J. M. Dziedzic, and T. Yamane, Optical trapping and manipulation of single cells using infrared laser beams, Nature **330**, 769–771 (1987).

[72] C. J. Bustamante, Y. R. Chemla, S. Liu, and M. D. Wang, Optical tweezers in single-molecule biophysics, Nature Reviews **1**, 369–408 (2021).

[73] S. B. Smith, L. Finzi, and C. Bustamante, Direct mechanical measurements of the elasticity of single dna molecules by using magnetic beads, Science **258**, 1122–1126 (1987).

[74] L. Chen, A. Offenhausser, and H. J. Krause, Magnetic tweezers with high permeability electromagnets for fast actuation of magnetic beads, Review of Scientific instruments **86** (2015).

[75] K. Mitsui, M. Hara, and A. Ikai, Mechanical unfolding of a2-macroglobulin molecules with atomic force microscope, Research Letters **385**, 29–33 (1996).

[76] J. Zlatanova, S. M. Lindsay, and S. H. Leuba, Single molecule force spectroscopy in biology using the atomic force microscope, Progress in Biophysics and Molecular Biology **74**, 37–61 (2000).

[77] H. C. Schaumann, M. Seitz, R. Krautbauer, and H. E. Gaub, Force spectroscopy with single bio-molecules, Current Opinion in Chemical Biology **4**, 524–530 (2000).

[78] V. Barsegov, D. Klimov, and D. Thirumalai, Mapping the energy landscape of biomolecules using single molecule force correlation spectroscopy: Theory and applications, Biophysics Journal **90**, 3827–3841 (2006).

[79] T. Hoffmann and L. Dougan, Single molecule force spectroscopy using polyproteins, Current Opinion in Chemical Biology **41**, 4781–4796 (2012).

[80] I. Popa, P. Kosuri, J. A. Cebollada, S. G. Manyes, and J. M. Fernandez, Force dependency of biochemical reactions measured by single-molecule force-clamp spectroscopy, Nature Protocols **8**, 1261–1276 (2013).

[81] M. Schlierf and M. Rief, Single-molecule unfolding force distributions reveal a funnel-shaped energy landscape, Biophysics Journal **90** (2006).

[82] R. I. Litvinov, H. Shuman, J. S. Bennett, and J. W. Weisel, Binding strength and activation state of single fibrinogen-integrin pairs on living cells, Proceedings of the National Academy of Sciences **99** (2002).

[83] E. Evans and K. Ritchie, Dynamic strength of molecular adhesion bonds, Biophysical Journal **72** (1997).

[84] S. Adhikari and K. Beach, Reliable extraction of energy landscape properties from critical force distributions, Physical Review Research **2** (2020).

[85] N. Grønbech-Jensen and O. Farago, A simple and effective verlet-type algorithm for simulating langevin dynamics, Molecular Physics **111**, 207–202 (2013).

[86] L. Verlet, Computer "experiments" on classical fluids. i. thermodynamical properties of lennard-jones molecules, Physical Review Letters **159**, 207–202 (1967).

[87] N. Metropolis and A. Rosenbluth, Equation of state calculations by fast computing machines, The Journal of Chemical Physics **21** (1953).

[88] D. J. Earl and M. W. Deem, Parallel tempering: Theory, applications, and new perspectives, Phys. Chem. Chem. Phys. **7**, 3910–3916 (2005).

[89] M. T. Woodside and S. M. Block, Reconstructing folding energy landscapes by single-molecule force spectroscopy, Annual Review of Biophysics **43** (2014).

[90] V. Barsegov and D. Thirumalai, Probing protein-protein interactions by dynamic force correlation spectroscopy, Physical Review Letters **95** (2005).

[91] A. Maitra and G. Arya, Model accounting for the effects of pulling-device stiffness in the analyses of single-molecule force measurements, Physical Review Letters **104** (2010).

[92] D. E. Makarov, Communication: Does force spectroscopy of biomolecules probe their intrinsic dynamic properties?, Journal of Chemical Physics **141** (2014).

[93] G. M. Nam and D. E. Makarov, Extracting intrinsic dynamic parameters of biomolecular folding from single?molecule force spectroscopy experiments, Protein Science **25** (2016).

[94] A. Garg, Escape-field distribution for escape from a metastable potential well subject to a steadily increasing bias field, Physical Review B **51** (1995).

[95] H. E. Stanley, Scaling, universality, and renormalization: Three pillars of modern critical phenomena, Reviews of Modern Physics **71** (1999).

[96] N. Kawashima and N. Ito, Critical behavior of the three-dimensional ±j model in a magnetic field, Journal of the Physical Society of Japan **62** (1993).

[97] S. M. Bhattacharjee and F. Seno, A measure of data collapse for scaling, Journal of Physics A: Mathematical and General **34** (2001).

[98] J. Houdayer and A. K. Hartmann, Low-temperature behavior of two-dimensional gaussian ising spin glasses, Physical Review B **70** (2004).

[99] S. Singh, R. Krishnan, and G. W. Robinson, Critical phenomena and scaling behavior in theories of activated barrier crossing, Physical Review Letters **68** (1992).

[100] S. Singh, R. Krishan, and G. W. Robinson, Critical scaling behavior in the activated-barrier-crossing problem, Physical Review E **49** (1994).

[101] B. Efron and R. J. Tibshiran, An introduction to the bootstrap, Chapman and Hall/CRC, 1st edition (1993).

[102] T. Cellmer, E. R. Henry, J. Hofrichter, and W. A. Eaton, Measuring internal friction of an ultrafast-folding protein, Proceedings of the National Academy of Sciences **105**, 18320–18325 (2008).

[103] S. Kamitori, A real knot in protein, Journal of American Chemical Society **118**, 8945–8946 (1996).

[104] J. B. Udgaonkar, Multiple routes and structural heterogeneity in protein folding, Tata Institute of Fundamental Research **37**, 489–510 (2008).

[105] S. S. Plotkin and P. G. Wolynes, Non-markovian configurational diffusion and reaction coordinates for protein folding, Physical Review Letter **80** (1998).

[106] D. E. Makarov, Interplay of non-markov and internal friction effects in the barrier crossing kinetics of biopolymers: insights from an analytically solvable model, Journal of Chemical Physics **138** (2013).

[107] K. Neupane, A. P. Manuel, and M. T. Woodside, Protein folding trajectories can be described quantitatively by one-dimensional diffusion over measured energy landscapes, Nature Physics **12** (2016).

[108] Y. Suzuki and O. K. Dudko, Single-molecule rupture dynamics on multidimensional landscapes, Physical Review Letter **104** (2010).

[109] M. Mann and R. Backofen, Exact methods for lattice protein models, Bio-Algorithms and Med-Systems **10** (2014).

[110] A. C. K. Farris and D. P. Landau, The role of chain-stiffness in lattice protein models : A replica-exchange wang-landau study, The Journal of Chemical Physics **149** (2018).

[111] S. Adhikari and K. S. D. Beach, Universal aspects of barrier crossing under bias, arxiv (2022).

VITA

Sudeep Adhikari

Education

M. Sc. Physics 2012

Jawaharlal Nehru University, New Delhi, India

Experience

Teaching Assistant 2015 – 2020

The University of Mississippi, Oxford, MS

Physics Lecturer 2012 – 2015

National School of Sciences, Kathmandu, Nepal

Published articles and preprints

Adhikari, S. & Beach, K. S. D. (2020). **Reliable extraction of energy landscape properties from critical force distributions.** https://doi.org/10.1103/PhysRevResearch.2.023276

Adhikari, S. & Beach, K. S. D. (2022). **Universal Aspects of Barrier Crossing Under Bias.** http://arxiv.org/abs/2203.16277

James R. Michels, Mohammad S. Nazrul, S. Adhikari, D. Wilkins & A. B. Pavel (2022). **Th1, Th2 and Th17 inflammatory pathways predict cardiometabolic protein expression in serum of COVID-19 patients.** https://doi.org/10.1039/D2MO00055E

Selected Conference Presentations

APS March Meeting 2021 by American Physical Society March 15-19, 2021

held online.

Title: The universality in activated barrier crossing.

Url: https://meetings.aps.org/Meeting/MAR21/Session/C12.10

APS March Meeting 2020 by American Physical Society March 2-6, 2020

Denver, CO, USA.

Title: An escape rate analysis for pulling experiments based on energy landscapes in two reaction coordinates.

Url: https://meetings.aps.org/Meeting/MAR20/Session/R24.10

APS March Meeting 2019 by American Physical Society March 4-8, 2019

Boston, MA, USA.

Title: Reliable extraction of energy landscape properties from critical force distributions.

Url: https://meetings.aps.org/Meeting/MAR19/Session/X64.8

Awards and achievements

Dissertation Fellowship Jan 2021- May 2022

The University of Mississippi, Oxford, MS

Summer Research Assistantship June 2020 - Aug 2020

The University of Mississippi, Oxford, MS

Merit scholarship recipient Jan 2011- May 2012

Jawaharlal Nehru University, New Delhi, India

Membership

American Physical Society(APS)

Nepal Physical Society (NPS)

Association of Nepali physicists in America (ANPA)